THE SIMILARITY RENORMALIZATION GROUP AND FACTORIZATION TECHNIQUES

By

Boyao Zhu

A DISSERTATION

Submitted to
Michigan State University
in partial fulfillment of the requirements
for the degree of

Physics – Doctor of Philosophy
Computational Math, Science & Engineering – Dual Major

2023

ABSTRACT

THE SIMILARITY RENORMALIZATION GROUP AND FACTORIZATION TECHNIQUES

By

Boyao Zhu

In this work, we explore the use of factorization techniques as a means to identify low-rank structures in nuclear interactions and many-body methods, which we aim to leverage in order to reduce computational cost and memory requirements of modern nuclear many-body calculations.

Using the Singular Value Decomposition (SVD), we show that we can construct accurate low-rank models of modern nucleon-nucleon interactions, and we develop a new variant of the Similarity Renormalization Group (SRG), that allows us to evolve nuclear interactions directly in the SVD-factorized form.

Next, We extend these developments to three-nucleon interactions, using randomized SVD (R-SVD) algorithms to mitigate the impact of the much greater basis dimensions. While we find evidence of low-rank structures in the three-nucleon interaction, we also identify obstacles to a persistent rank reduction that we trace back to SRG-induced interactions.

Finally, we explore applications of the SVD for factorization and rank reduction within the context of the In-Medium SRG (IMSRG). We develop rank-reduced IMSRG flow equations, which, while promising, still pose computational challenges stemming from the treatment of the so-called particle-hole terms. As a first step towards tackling this problem, we perform a detailed breakdown of the scaling and importance of all contributions in the IMSRG flow in applications for a schematic model as well as infinite neutron matter based on realistic interactions from chiral Effective Field Theory.

Acknowledgements

I extend my deepest gratitude to all those who have provided unwavering support and encouragement throughout the completion of my dissertation in the field of computational physics. Their invaluable assistance has been instrumental in turning this academic endeavor into a tangible reality.

First and foremost, I express my profound appreciation to my esteemed supervisor, Prof. Heiko Hergert, whose expert guidance and profound insights have been invaluable throughout this research journey. His unwavering encouragement and belief in my abilities have been a constant source of motivation and inspiration.

I am also immensely thankful to the esteemed committee members, Prof. Scott K Bogner, Prof. Sean N. Liddick, Prof. Mark Iwen, Prof. Matthew Hirn, and Prof. Longxiu Huang from the Department of Physics and Center of Computational Mathematics, Science, and Engineering at Michigan State University. To Prof. Huang, I warmly welcome your involvement and eagerly anticipate benefiting from your expertise in the final stages of my work.

Gratitude is extended to my colleagues Jacob Davison, Roland Wirth, and Jiangming Yao for their engaging discussions and insightful ideas. Their diverse perspectives have enriched my understanding of the subject matter and made this academic journey all the more rewarding.

I would like to express my deep appreciation and send my best wishes to my cohort for

their constant spiritual support and companionship during this journey. To each member, including Hao Lin, Xingze Mao, Tong Li, Mengzhi Chen, Avik Sakar, Zhite Yu, Omokuyani Udiani, Xiaoyi Sun, Zhouyou Fan, Rui Zhang, Kang Yu, Shuyue Xue, Ruixin Zhang, Lijiang Xu, Siyuan Ma, Min Feng, and anyone I met, your unwavering presence and encouragement have meant the world to me, and I am truly grateful for your invaluable support.

I would be remiss not to express my heartfelt thanks to my family for their unwavering support and belief in my abilities. Their love and encouragement have been a constant source of strength throughout the ups and downs of this scholarly pursuit.

Finally, my appreciation goes to all the participants who contributed to this research, making it possible to achieve profound and meaningful outcomes.

With profound gratitude to all who have played an integral role in my academic journey, I am sincerely thankful for their invaluable contributions and encouragement.

Dedication

Will insert upon submission

Introduction or Preface

Insert your preface text here if applicable. This page is optional, you may delete it if not needed. If you delete this page make sure to move page counter comment in thesis.tex to correct location.

TABLE OF CONTENTS

Part I

Preliminaries

Chapter 1

Introduction to *ab initio* Nuclear Many-Body Theory

The aim of theoretical nuclear physics is to accurately describe the structure and dynamics of atomic nuclei. Over the past decade, new developments in many–body theory, in particular new insights into the nuclear interactions and rapid growth of many–body technology, has greatly expanded the capabilities of *ab initio*[1] [21, 40] nuclear structure and reaction theory in low–energy nuclear physics.

1.1 The nuclear many-body problem

Nuclear structure and dynamics are governed by the time-independent and time-dependent many-body Schrödinger equations,

$$H\,|\Psi_k^A\rangle = E_k\,|\Psi_k^A\rangle \tag{1.1}$$

and

$$i\hbar\frac{d}{dt}\,|\Psi(t)\rangle = H\,|\Psi(t)\rangle\ , \tag{1.2}$$

[1] This means "from first principles", i.e., starting from interactions between constituent nucleons and deriving all other observables from there

respectively. The main task of nuclear many-body theory is to provide precise and accurate solutions to these equations. Here, $|\Psi_k^A\rangle$ denotes the k-th eigenstate of the system with eigenvalue E_k, and $|\Psi(t)\rangle$ is a general time-dependent state describing the target and projectile(s) in a nuclear reaction.

The nuclear Hamiltonian H arises from the modeling of the strong interaction at low energy using nucleonic degrees of freedom

$$H = T + V^{[2]} + V^{[3]} + \cdots \tag{1.3}$$

T denotes the (intrinsic) kinetic energy, and $V^{[2]}$ and $V^{[3]}$ are two-nucleon (NN) and three-nucleon (3N) interactions, systematically constructed from chiral effective field theory (χEFT), see Section 1.2, where χEFT is a systematic framework for describing the strong interaction at low momentum, using pions and nucleons as degrees of freedom, and incorporating the chiral symmetry of Quantum Chromodynamics . Before then, many phenomenological potentials, such as Argonne and CD-Bonn [2], describe nucleus from the bottom up by solving the Schrödinger equation.

Nuclear many-body physics, when trying to solve Schrödinger equation, faces two major challenges. The first is that the nuclear forces between nuclei cannot be directly derived from QCD, the underlying theory of strong interaction. The second major challenge of nuclear theory lies in the difficulty of obtaining accurate results in an efficient way, due to the fact that the many-body Hilbert space grows in a combinatoric way as the number of particles increases. Thus, an exact diagonalization of the nuclear Hamiltonian, referred to as a no-

[2] they are rooted in pion or boson-exchange pictures to some degree, and give a very precise and accurate fit to NN scattering data, but lack the more systematic underpinning of chiral EFT, especially when it comes to consistent 3N (and higher) forces, as well as other operators like transitions and currents.

core Full Configuration Interaction (FCI) calculation, scales exponentially with the number of particles A, and quickly becomes unfeasible as A increases.

1.2 Interactions from Chiral Effective Field Theory

Efforts to construct a fundamental theory of the interaction between nucleons date back as far as eight decades. With the discovery of the neutron by Chadwick [17] in 1932, it became evident that the atomic nuclei are built up from protons and neutrons. The concept of strong nuclear interactions was first introduced by Heisenberg [36], in order to explain why electromagnetic forces cannot bind the nucleus together. In 1935, the meson exchange theory by Hideki Yukawa [111] suggested that the nucleons create the force by exchanging particles between each other, in analogy to the theory of the electromagnetic interaction where the exchange of the particle, known as photon, is the cause of the force. By the 1960s, the systematic measurements of nucleon-nucleon (NN) observables and phase shift [90] analysis had revealed the existence of a repulsive core, an attractive intermediate- ranged force, as well as strong tensor and spin-orbit forces [66], see Figure 1.1. Yukawa's meson exchange, which included these features was an excellent phenomenology [65] for describing nuclear interactions. However, with the rise of Quantum Chromodynamics (QCD), we desire to understand nuclear interactions on a more fundamental level.

Within the Standard Model of particle physics, QCD provides the theoretical for describing the strong interaction, while nuclear interactions are considered as residuals of strong forces. According to the theory, the fundamental degrees of freedom are quarks and gluons, which carry an abstract color charge. Quarks interact via gluon exchange, but unlike other exchange particles, gluons also can also interact with themselves, because QCD is a is a

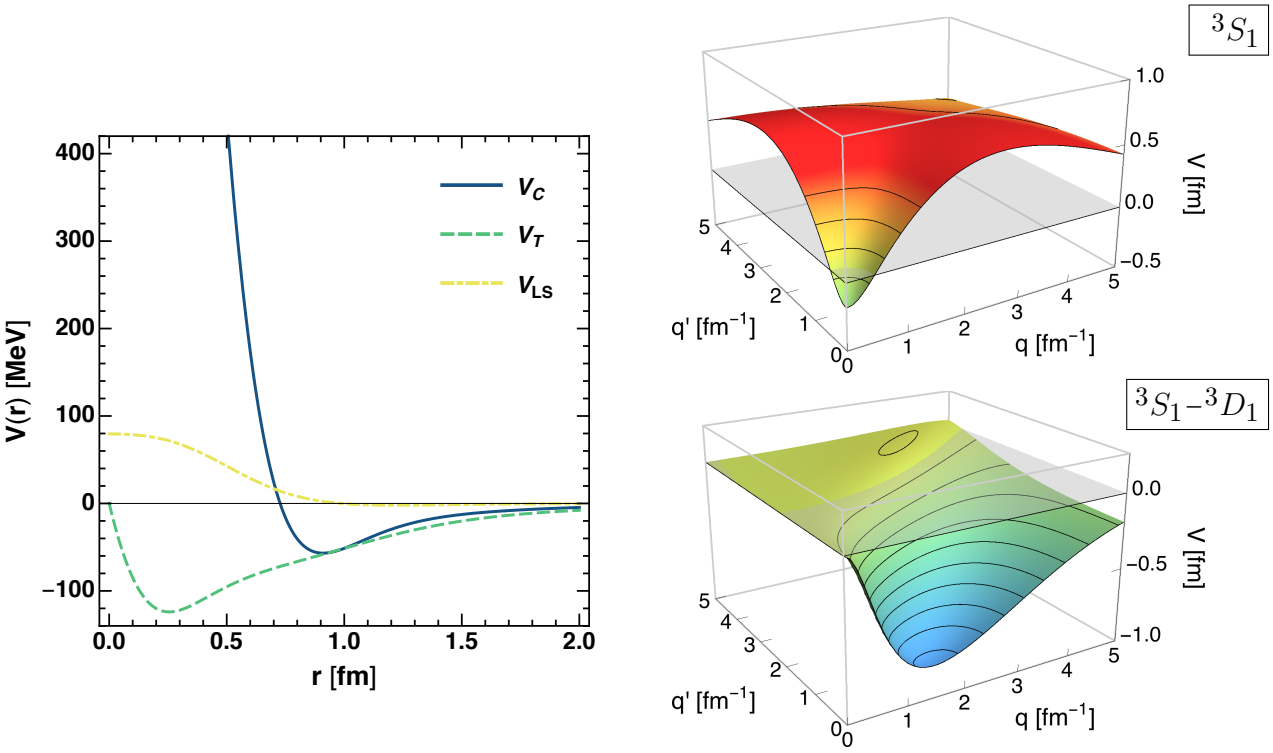

Figure 1.1: The Argonne V18 [109] nuclear potential in coordinate (left) and momentum (right) representations [41]. In the left panel, the radial dependencies of the central (V_C), tensor (V_T) and spin-orbit interactions (V_{LS}) in the $S = 1, T = 0$ spin- and isospin-channel are shown, while the right panel shows its momentum space matrix elements in the deuteron partial waves.

non-Abelian gauge field theory. A consequence of this is that the QCD coupling constant becomes weak at high energies, a property that is referred to asymptotic freedom. Thus, QCD processes at high energy and momentum transfer can be described with perturbative methods. At low energies, where nuclear physics resides, the QCD coupling is large and the theory is inherently non-perturbative. The main approach for performing non-perturbative calculations in this regime is Lattice QCD (LQCD), which simulates QCD processes on a discrete space-time lattice. However, the range of applications of LQCD is limited due to the enormous computational cost, as well as algorithmic challenges, in particular related to extracting meaningful results from a noisy signal.

Therefore, QCD calculations of finite nuclei are not feasible, and even a direct derivation

of nuclear forces from QCD is extremely challenging.

In the 1980s, Steven Weinberg applied the concepts of effective field theory (EFT) to develop a systematic and model-independent treatment of low-energy QCD that also accounts for the spontaneously broken chiral symmetry (see [101–103] for more detailed discussion), with pions and nucleons as effective degrees of freedom. This chiral EFT (χEFT) is established through a low-momentum expansion and is valid only at low energies, suppressing high-momentum contributions by introducing regularizations. According to Weinberg, one can construct effective Lagrangians that consist of all interactions that are consistent with the symmetries of low-energy QCD and organized by an expansion in powers of (Q/Λ). Here, Q is a typical momentum of the interacting system, and Λ is the so-called breakdown scale of the theory. Applying this Lagrangian to a certain process, an infinite number of Feynman diagrams appear, but they can be organized according to the power counting in $(Q\Lambda)$, as shown in Figure 1.2. These interactions consist of (multi-)pion exchanges between nucleons, denoted by dashed lines, as well as nuclear contact interactions. While the chiral interactions [15] constructed in this framework are nowadays the de facto standard input to *ab initio* many-body calculations, open challenges remain.

Because the typical cutoffs Λ for χEFT interactions are lower than those of phenomenological interactions like AV18 and CD-Bonn [64], they tend to be better behaved in *ab initio* calculations and results converge more rapidly. However, such calculations are still computationally heavy. Merely using an even lower cutoff to obtain even softer χEFT potentials is problematic, because it will eventually affect their accuracy [50]. To solve this problem, we perform renormalization group (RG) evolutions of the nuclear interaction, which "soften" them while preserving relevant physical information. RG methods are natural colleagues to any EFT, since they allow us to dial the EFTs resolution scales, and are (in principle) able

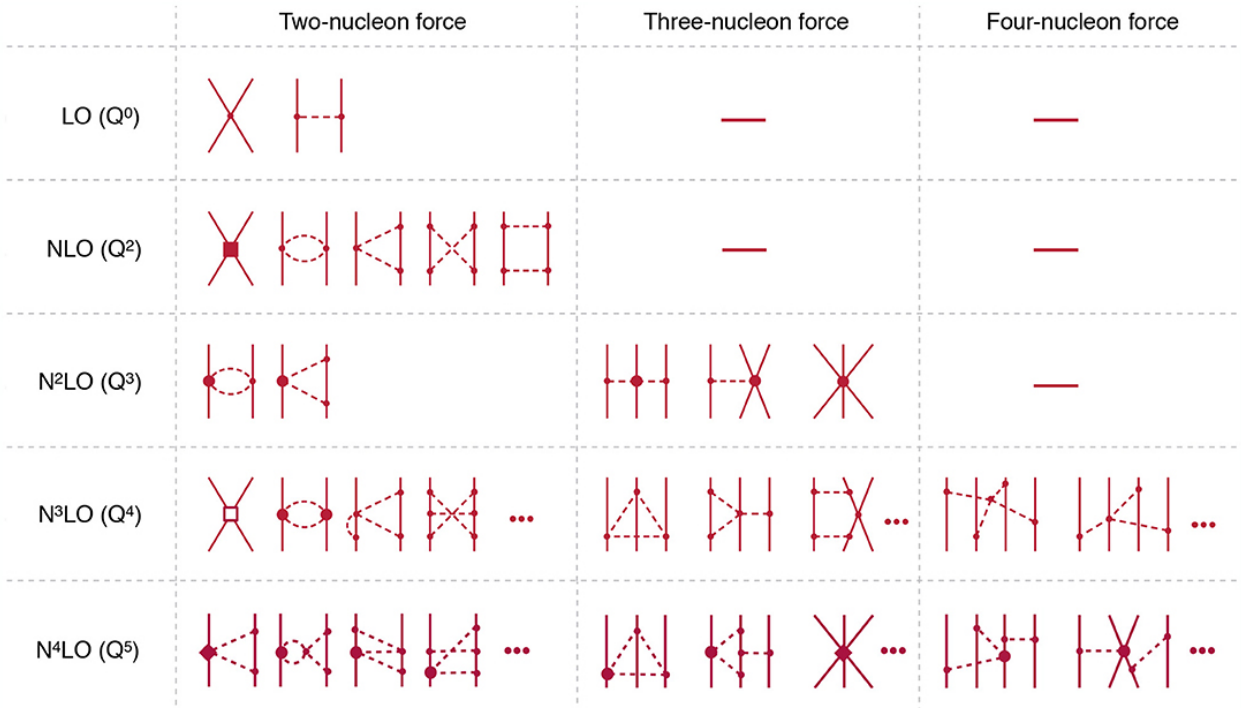

Figure 1.2: Hirarchy of nuclear forces at increasing orders up to N^{4}LO in chiral expansion arranged by the particle rank of the interaction in the Weinberg scheme [23]. Solid and dashed lines refer to nucleons and pions, respectively. Solid dots, filled circles, filled squares, filled diamonds, and open squares refer to vertices from the Lagrangian of dimension $\Delta =$ 0, 1, 2, 3 and 4, respectively.

to event connect theories with different degrees of freedom [59, 60].

1.3 Elements of Many-Body Theory

Let us now review some of the essential ideas of many-body theory that will become relevant in later chapters. We will keep the discussion light on mathematical details and refer to Refs. [25, 81, 88] for details.

1.3.1 Many-Particle Spaces and Basic Concepts

In nuclear physics, we are solely dealing with systems of fermions, protons and neutrons, which are usually regarded as identical particles with a different isospin quantum number when dealing with the strong interaction. In coordinate representation, an abstract one-particle state $|i\rangle$ has the following wave function,

$$\varphi_i(\vec{x}) \equiv \langle \vec{x} \,|\, i \rangle \tag{1.4}$$

where $\vec{x} \equiv (\vec{r}, s, t)$ denotes the spatial $(\vec{r})$ and internal coordinates (spin s, isospin t). The overlap of two single-particle states is easily obtained using the identity resolution

$$\mathbb{1} = \int d\vec{x} \;\; |\vec{x}\rangle \, \langle \vec{x}| \tag{1.5}$$

where $\vec{\mathbb{1}}$ designates the identity operator in the product of the coordinate and internal space(s) and the integral symbol indicates the integration over the 3 dimensional Euclidean

space and the summation over discrete internal variable(s). Thus

$$\langle i \,|\, j \rangle = \int d\vec{x} \;\langle i \,|\, \vec{x} \rangle \langle \vec{x} \,|\, j \rangle = \int d\vec{x} \varphi_i^*(\vec{x}) \varphi_j(\vec{x})$$

where $\langle i \,|\, \vec{x} \rangle$ and $\langle \vec{x} \,|\, i \rangle$ are complex conjugates. We typically work in single-particle bases that are orthonormalized, so that

$$\langle i \,|\, j \rangle = \delta_{ij} \,. \tag{1.6}$$

Any single particle state $\psi(\vec{x}) \equiv \langle \vec{x} \,|\, \psi \rangle$ can be expressed as a linear combination of the vectors in a complete basis $\{\varphi_i\}_{i \in \mathbb{N}}$

$$\psi(\vec{x}) = \sum_i c_i \varphi_i(\vec{x}) \tag{1.7a}$$

or

$$|\psi\rangle = \sum_i c_i \,|i\rangle \tag{1.7b}$$

where the summation generally extends over the full basis. The expansion coefficients c_i are given as

$$c_i = \langle i \,|\, \psi \rangle = \int d\vec{x} \; \varphi_i^*(\vec{x}) \psi(\vec{x}) \tag{1.8}$$

where the resolution of identity has been used again, Eq. (1.5). A complete orthonormal basis $\{|i\rangle\}$ or $\{\varphi_i(\vec{x})\}$ could thus be regarded as a basis for a one-particle Hilbert space $\mathcal{V}_1$.[3]

Consider next a system of N identical fermions, e.g., a system of N nucleon. Its state

[3] Technically, the states $|i\rangle$ and $\{\varphi_i(\vec{x})\}$ are different vector spaces, with the former being abstract while the latter being a product of square-integrable functions with a spin-isospin spinor space. However, these spaces are merely related by a natural isomorphism, as indicated in Eq. (1.4) and we thus use the identical symbol $\mathcal{V}_1$ for both. The same convention will be used for corresponding many-particle spaces.

space $\mathcal{F}_\mathcal{N}$ can be interpreted as an antisymmetric outer product of N single-particle Hilbert spaces

$$\mathcal{F}_\mathcal{N} = \mathcal{A}\mathcal{V}_\mathcal{N} \tag{1.9}$$

where $\mathcal{A}$ denotes the so-called antisymmetrizer, i.e., the projector onto the totally antisymmetric subspace of $\mathcal{V}_\mathcal{N}$, and

$$\mathcal{V}_\mathcal{N} = \underbrace{\mathcal{V}_1 \otimes \mathcal{V}_1 \otimes \cdots \otimes \mathcal{V}_1}_{\text{N-times}} = \mathcal{V}_1^{\otimes N}$$

The product space $\mathcal{V}_\mathcal{N}$ consists of many-body states where none of the particles are interacting with each other, i.e., simple product states of the form

$$\varphi_{i_1}(\vec{x}_1) \otimes \varphi_{i_2}(\vec{x}_2) \otimes \cdots \otimes \varphi_{i_N}(\vec{x}_N) \tag{1.10a}$$

or

$$|i_1\rangle \otimes |i_2\rangle \otimes \cdots \otimes |i_N\rangle \ . \tag{1.10b}$$

For compactness, this is usually written as

$$\varphi_{i_1}(\vec{x}_1)\varphi_{i_2}(\vec{x}_2)\cdots\varphi_{i_N}(\vec{x}_N) \tag{1.11a}$$

or

$$|i_1\rangle\,|i_2\rangle \cdots |i_N\rangle \equiv |i_1 i_2 \cdots i_N\rangle \tag{1.11b}$$

A general normalized basis vector in $\mathcal{F}_\mathcal{N}$ can be constructed from the single-particle basis as

$$|\Phi_K\rangle = \sqrt{N!}\mathcal{A}\,|i_1 i_2 \cdots i_N\rangle \tag{1.12}$$

where K designates the index set

$$K \equiv \{i_1, i_2, \cdots, i_N\}\,. \tag{1.13}$$

The antisymmetrizer $\mathcal{A}$ has the explicit form

$$\mathcal{A} = (N!)^{-1} \sum_{P \in S_N} (-1)^{\pi(P)} P \tag{1.14}$$

where the sum extends over $N!$ permutations P that constitute the symmetric group S_N, $\pi(P)$ is the signature of P — i.e., the number of pairwise permutations it consists of — and $(-1)^{\pi(P)}$ is referred to as the parity of P. Antisymmetrized product states of the form (1.12) are also referred to as *Slater determinants* as well as basis configurations in the following. The configurations $|\Phi_K\rangle$ form a basis of the N-particle space $\mathcal{F}_\mathcal{N}$ so that a general state of any many-fermion system can be expanded as follows:

$$|\Psi\rangle = \sum_K c_K\,|\Phi_K\rangle \tag{1.15}$$

where

$$c_K = \langle \Phi_K\,|\,\Psi\rangle\ . \tag{1.16}$$

The single-particle states appearing in K are said to be *occupied* in this configuration while those not present are said to be *unoccupied*.

1.3.2 Occupation Number Representation

To uniquely specify any given basis configuration, we need to specify a fixed ordering of the single-particle basis states, e.g., such that indices are in ascending order, and we need to know which single-particle states are occupied and which are not in $|\Phi_K\rangle$. We can then introduce the *occupation number representation*, where a given $|\Phi_K\rangle$, can be uniquely defined as

$$|\Phi_K\rangle = |\{i_1, i_2, \cdots, i_N\}\rangle \equiv |n_1 n_2 \cdots n_N \cdots\rangle \tag{1.17}$$

where for fermionic systems the occupation number n_k for any configuration can only take on two values, 0 and 1. Clearly, $n_k = 1$ if $|i_k\rangle$ is occupied in $|\Phi_K\rangle$ for $i_k \in K$.

For example, a five-particle state $|\{i_1, i_2, \cdots, i_5\}\rangle$ with $i_1 = 0$, $i_2 = 1$, $i_3 = 4$, $i_4 = 7$ and $i_5 = 9$, has the occupation number representation

$$|\Phi_{01479}\rangle = |\{0, 1, 4, 7, 9\}\rangle = |110010010100 \cdots 0 \cdots\rangle \ . \tag{1.18}$$

As we can see, the index-based notation for fermionic systems is usually more concise than the occupation number notation. The latter, however, reveals that basis configurations can be represented as bit strings. This is very convenient for numerical implementation, in particular for implementing the action of particle creation and annihilation operators, which will be discussed in the next subsection.

1.3.3 Creation and Annihilation Operators

We are now in the proper position to introduce the time-independent operators $\hat{a}_i$ and $\hat{a}_i^\dagger$, which annihilate and create a particle in the single-particle state $|i\rangle$, respectively. We

define the action of a fermionic annihilation operator as follows:

$$\begin{aligned} \hat{a}_i \left|\{i j_2 j_3 \cdots j_N\}\right\rangle &= \left|\{j_2, j_3 \cdots j_N\}\right\rangle \quad \text{if } i \notin \{j_2, j_3, \cdots, j_N\}\,, \\ \hat{a}_i \left|\{j_1 j_2 j_3 \cdots q_N\}\right\rangle &= 0 \qquad\qquad\qquad\quad \text{if } i \notin \{j_1, j_2, j_3, \cdots, j_N\}\,. \end{aligned} \tag{1.19}$$

The annihilation operator annihilates a particle in the state i assuming there is a particle present, i.e., the state i is occupied (and distinct from all other occupied states). If there is no particle in that state, the annihilation operator makes the whole N-particle state vanish.

In the first equation of Eq. (1.19) we have made an assumption that the state i occurs at the first position in the configuration for simplicity. If this is not the case, we can use the antisymmetrization of the fermionic state to obtain

$$\left|\{i_1 i_2 i_3 i_4 \cdots\, i_N\}\right\rangle = (-1)^{\pi(P)} \left|\{j_1 j_2 j_3 j_4 \cdots\, j_N\}\right\rangle \tag{1.20}$$

where $(-1)^{\pi(P)}$ is the parity of the permutation P that reorders the set $\{i_1, i_2, \ldots, i_N\}$ into the set $\{j_1, j_2, \ldots, j_N\}$. For example

$$\begin{aligned} \hat{a}_i \left|\{ijkl\cdots\}\right\rangle &= \left|\{jkl\cdots\}\right\rangle \\ \hat{a}_i \left|\{jikl\cdots\}\right\rangle &= \hat{a}_i(-1)\left|\{ijkl\cdots\}\right\rangle = -\left|\{jkl\cdots\}\right\rangle \\ \hat{a}_i \left|\{jkil\cdots\}\right\rangle &= \hat{a}_i(-1)^2\left|\{ijkl\cdots\}\right\rangle = \left|\{jkl\cdots\}\right\rangle\,. \end{aligned}$$

With a fermionic state in the occupation number representation one can write Eq. (1.20) in the following compact form

$$\hat{a}_i \left|n_1 n_2 \cdots n_i \cdots\right\rangle = (-1)^{s(i)} n_i \left|n_1 n_2 \cdots\, n_i - 1 \cdots\right\rangle \tag{1.21}$$

where $s(i)$ is the number of occupied states that are preceding the state i, which is also equivalent to the number of pairwise permutations that are needed to move the state i from its position to the first position:

$$s(i) = \sum_{k<i} n_k \tag{1.22}$$

Now before introducing the creation operator, we first have to define a vacuum state $|\varnothing\rangle$, which is also referred to as a true vacuum state since all single-particle states are unoccupied:

$$|\varnothing\rangle \equiv |0000\cdots0\cdots\rangle \tag{1.23}$$

This implies

$$\hat{a}_i |\varnothing\rangle = 0 \tag{1.24}$$

for any single-particle state, as well as

$$\begin{aligned} &\hat{a}_i |i\rangle = |\varnothing\rangle \ , \\ &\hat{a}_i |j\rangle = 0 \qquad \text{if } i \neq j \ . \end{aligned} \tag{1.25}$$

Now we can introduce the creation operator by simply defining it as the Hermitian adjoint of the annihilation operator. Let us see what will result when $\hat{a}_i^\dagger$ acts on the vacuum state $|\varnothing\rangle$ and we take the Hermitian conjugate:

$$\hat{a}_i |i\rangle = |\varnothing\rangle \quad \longrightarrow \quad \langle i| \hat{a}_i^\dagger = \langle\varnothing| \ . \tag{1.26}$$

It then follows when forming the scalar product with $|\varnothing\rangle$

$$\langle i|\,\hat{a}_i^\dagger\,|\varnothing\rangle = \langle\varnothing\,|\,\varnothing\rangle = 1\,. \tag{1.27}$$

Recalling the completeness and orthonormality of the single-particle states, Eq. (1.27) also indicates that

$$\hat{a}_i^\dagger\,|\varnothing\rangle = |i\rangle\ . \tag{1.28}$$

In general, when the creation operator acts on an N–particle state (including $|\varnothing\rangle$ in case $N = 0$) it yields an $(N+1)$–particle state, assuming the created state was not occupied initially. If the created state was occupied initially, we will obtain zero due to the antisymmetrization property.

$$\begin{aligned} \hat{a}_i^\dagger\,|\{j_1 j_2 \cdots j_N\}\rangle &= |\{i j_1 j_2 \cdots j_N\}\rangle \quad \text{if } i \notin \{j_1, j_2, \cdots, j_N\}\,, \\ \hat{a}_i^\dagger\,|\{j_1 j_2 \cdots j_N\}\rangle &= 0 \qquad\qquad\qquad\quad \text{if } i \in \{j_1, j_2, \cdots, j_N\}\,. \end{aligned} \tag{1.29}$$

Thus, the second quantization formalism naturally accounts for the Pauli exclusion principle, which prohibits two fermions from occupying the same single-particle state.

In general, we can express the action of the creation operator on a state in occupation number representation analogous to Eq. (1.21) as

$$\hat{a}_i^\dagger\,|n_1 n_2 \cdots n_i \cdots\rangle = (-1)^{s(i)}(1 - n_i)\,|n_1 n_2 \cdots\, n_i + 1\, \cdots\rangle \tag{1.30}$$

where $s(i)$ is again give by Eq. (1.22)

1.3.4 Number Operator

Using the definitions of the creation and annihilation operators, we can define the number operator as

$$\hat{N}_i \equiv \hat{a}_i^\dagger \hat{a}_i \,. \tag{1.31}$$

This operator conserves particle number and it is Hermitian:

$$\hat{N}_i^\dagger = (\hat{a}_i^\dagger \hat{a}_i)^\dagger = \hat{a}_i^\dagger \hat{a}_i = \hat{N}_i \,. \tag{1.32}$$

The effects of the operator $\hat{a}_i^\dagger \hat{a}_i$ on an arbitrary N–particle state have to be differentiated into two cases, namely the case (1) of $|i\rangle$ being occupied and the case (2) of $|i\rangle$ not being occupied in the N–particle state. When $\hat{N}_i$ acts on an N–particle state $|\Phi_K\rangle$ where $i \in K$, we obtain

$$\begin{aligned}
\hat{a}_i^\dagger \hat{a}_i |\Phi_K\rangle &= \hat{a}_i^\dagger \hat{a}_i |\{j_1 j_2 \cdots j_{n-1}\ \underline{i}\ j_{n+1} \cdots j_N\}\rangle \\
&= \hat{a}_i^\dagger \hat{a}_i (-1)^{n-1} |\{\underline{i}\ j_1 j_2 \cdots j_{n-1} j_{n+1} \cdots j_N\}\rangle \\
&= (-1)^{n-1} \hat{a}_i^\dagger |\{j_1 j_2 \cdots j_{n-1} j_{n+1} \cdots j_N\}\rangle \\
&= (-1)^{n-1} |\{\underline{i}\ j_1 j_2 \cdots j_{n-1} j_{n+1} \cdots j_N\}\rangle \\
&= (-1)^{2n-2} |\{j_1 j_2 \cdots j_{n-1}\ \underline{i}\ j_{n+1} \cdots j_N\}\rangle \\
&= |\Phi_K\rangle \,.
\end{aligned} \tag{1.33}$$

When $\hat{N}_i$ acts on an N–particle state $|\Phi_K\rangle$ where $i \notin K$, we get

$$\hat{a}_i^\dagger \hat{a}_i |\Phi_K\rangle = 0 \,. \tag{1.34}$$

We can combine the results (1.33) and (1.34) by writing

$$\hat{a}_i^\dagger \hat{a}_i \, |\Phi_K\rangle = n_i \, |\Phi_K\rangle \tag{1.35a}$$

or

$$\hat{a}_i^\dagger \hat{a}_i \, |n_1 n_2 \cdots n_i \cdots\rangle = n_i \, |n_1 n_2 \cdots n_i \cdots\rangle \; . \tag{1.35b}$$

Thus, the state in number occupation representation is an eigenstate of $\hat{N}_i$ with eigenvalue n_i. Now we define the total number operator as the sum of all possible number operators

$$\hat{N} \equiv \sum_i \hat{N}_i = \sum_i \hat{a}_i^\dagger \hat{a}_i \, . \tag{1.36}$$

Its eigenvalue for an arbitrary occupation-number state is equal to the total number of particles in that state:

$$\hat{N} \, |\Phi_K\rangle = N \, |\Phi_K\rangle \; , \qquad N = \sum_i n_i \, . \tag{1.37}$$

1.3.5 Anti-Commutation Relations

The fermionic creation and annihilation operators introduced above obey the so-called *canonical anti-commutation relations*: For arbitrary single-particle states i and j, we have

$$\{\hat{a}_i^\dagger, \hat{a}_j\} = \hat{a}_i^\dagger \hat{a}_j + \hat{a}_j \hat{a}_i^\dagger = \delta_{ij} \, , \tag{1.38}$$

$$\{\hat{a}_i, \hat{a}_j\} = 0 \, , \tag{1.39}$$

and

$$\{\hat{a}_i^\dagger, \hat{a}_j^\dagger\} = 0\,. \tag{1.40}$$

Note that the relations (1.39) and (1.40) imply that

$$\hat{a}_i^2 = (\hat{a}_i^\dagger)^2 = 0\,, \tag{1.41}$$

which again reflects that there can be at most one fermion in a given single-particle state, as demanded by the Pauli exclusion principle.

These anti-commutation relations impose a particular structure on the overlap of fermionic many-particle states. For example, let us calculate the overlap of a pair of two-fermion states $\langle \Phi_{ij} \,|\, \Phi_{kl} \rangle$, where $i, j \neq k, l$:

$$\langle \Phi_{ij} \,|\, \Phi_{kl} \rangle = \langle \{ij\} \,|\, \{kl\} \rangle = \langle \varnothing |\, \hat{a}_i \hat{a}_j \hat{a}_k^\dagger \hat{a}_l^\dagger \,| \varnothing \rangle \tag{1.42}$$

$$= \langle \varnothing |\, \hat{a}_i (\delta_{jk} - \hat{a}_k^\dagger \hat{a}_j) \hat{a}_l^\dagger \,| \varnothing \rangle \tag{1.43}$$

$$= \delta_{jk} \langle \varnothing |\, \hat{a}_i \hat{a}_l^\dagger \,| \varnothing \rangle - \langle \varnothing |\, \hat{a}_i \hat{a}_k^\dagger \hat{a}_j \hat{a}_l^\dagger \,| \varnothing \rangle \tag{1.44}$$

$$= \delta_{jk} \langle i \,|\, l \rangle - \langle \varnothing |\, \hat{a}_i \hat{a}_k^\dagger (\delta_{jl} - \hat{a}_l^\dagger \hat{a}_j) \,| \varnothing \rangle \tag{1.45}$$

$$= \delta_{jk} \delta_{il} - \delta_{jl} \langle \varnothing |\, \hat{a}_i \hat{a}_k^\dagger \,| \varnothing \rangle + \langle \varnothing |\, \hat{a}_i \hat{a}_k^\dagger \hat{a}_l^\dagger \hat{a}_j \,| \varnothing \rangle \tag{1.46}$$

$$= \delta_{jk} \delta_{il} - \delta_{jl} \langle i \,|\, k \rangle + \cancel{\langle \varnothing |\, \hat{a}_i \hat{a}_k^\dagger \hat{a}_l^\dagger \hat{a}_j \,| \varnothing \rangle} \tag{1.47}$$

$$= \delta_{jk} \delta_{il} - \delta_{jl} \delta_{ik}\,, \tag{1.48}$$

where we have used the orthonormality of the single-particle states, $\langle i \,|\, j \rangle = \delta_{ij}$. We note that the final expression is antisymmetrized under permutations in the bra ($i \leftrightarrow j$) and ($k \leftrightarrow l$). For states with N particles, we analogously obtain antisymmetrized products of N Kronecker

deltas.

The calculation of the overlap illustrates the overall strategy for evaluating expectation values of strings of creation and annihilation operators: The goal is to shift the annihilator operator to the far right until it acts on the vacuum state, and apply the "killing condition" (1.24) to make terms vanish for good. Along the way, we can also exploit that $\langle\varnothing|\,\hat{a}_i^\dagger = 0$, which follows from Eq. (1.24) by taking the Hermitian adjoint.

1.3.6 The Fermi Vacuum

In many-body calculations, it is often convenient to organize the many-body basis in terms of excitations of a non-interacting fermionic ground state $|\Phi_0\rangle$. One then refers to this Slater determinant state as the Fermi vacuum in order to distinguish it from the true vacuum $|\varnothing\rangle$. In the ground state of a non-interacting fermionic many-particle system, the occupied states are usually the energetically lowest available single-particle states. We can then introduce the so-called *Fermi level* as the occupied single-particle state with the highest energy, and refer to its energy as the *Fermi energy* ε_F. The single-particle basis can now be divided into unoccupied or *particle* states with $\varepsilon > \varepsilon_F$, and occupied or *hole* states with $\varepsilon \leq \varepsilon_F$. With these conventions, we can write the Fermi vacuum as

$$|\Phi_0\rangle = \left(\prod_{\varepsilon_i \leq \varepsilon_F} \hat{a}_i^\dagger\right)|\varnothing\rangle \tag{1.49}$$

where the index i designates different single-particle states up to the Fermi level.

Let us now modify our notation a bit and reserve ranges of indices for particular kinds of single-particle states[4]. We use letters $ijkl\cdots$ for states below the Fermi level (holes) and

[4]The convention used in the following originates in quantum chemistry, see [88], for example.

$i, j, k, \ldots$	hole state
$a, b, c, \ldots$	particle state
$p, q, r, \ldots$	generic state

Table 1.1: Single-Particle Labeling Convention

$abcd\cdots$ for states above the Fermi level (particles), while general single-particle state are indicated by letters $pqrs\cdots$ (cf. Table 1.1).

As suggested above, we can now write a given one–particle–one–hole $(1p1h)$ state as

$$|\Phi_i^a\rangle = \hat{a}_a^\dagger \hat{a}_i \, |\Phi_0\rangle \ ,$$

a $(2p2h)$ state as

$$|\Phi_{ij}^{ab}\rangle = \hat{a}_a^\dagger \hat{a}_b^\dagger \hat{a}_j \hat{a}_i \, |\Phi_0\rangle$$

and a general $(ApAh)$ excited state as

$$|\Phi_{ijk\ldots}^{abc\cdots}\rangle = \hat{a}_a^\dagger \hat{a}_b^\dagger \hat{a}_c^\dagger \cdots \hat{a}_k \hat{a}_j \hat{a}_i \, |\Phi_0\rangle \ . \tag{1.50}$$

We also see that

$$\hat{a}_i^\dagger \, |\Phi_0\rangle = 0 \, , \tag{1.51}$$

$$\hat{a}_a \, |\Phi_0\rangle = 0 \, , \tag{1.52}$$

because a creation operator can not create a particle under the Fermi level since the state was occupied in $|\Phi_0\rangle$, and an annihilator cannot destroy a particle above the Fermi level since there are no particles present.

1.3.7 Normal Ordering and Wick's Theorem

Next, we introduce the idea of normal ordering the Hamiltonian with respect to the vacuum state $|\varnothing\rangle$. For two arbitrary creation or annihilation operators, we define

$$XY \equiv \{XY\} + \overbrace{XY}\,, \tag{1.53}$$

where the first term on the right $\{\cdots\}$[5] designates the *normal-ordered* product operator, and the brace indicates the *contraction* of X and Y.

The normal-ordered operators are defined as the product of the same operators whose ordering is rearranged in such a way that all the creators are to the left of all the annihilators, keeping only the signs from anticommuting the operators, but not the Kronecker delta from Eq. (1.38), which is taken care of by the contraction. For example. we have

$$\{a_p^\dagger a_q a_r^\dagger\} = \{-a_p^\dagger a_r^\dagger a_q\} = a_r^\dagger a_p^\dagger a_q\,.$$

It is obvious that the expectation values of arbitrary normal-ordered operators with respect to the true vacuum $|\varnothing\rangle$ must vanish

$$\langle\varnothing|\,\{a_p^\dagger\cdots a_q\}\,|\varnothing\rangle = 0\,, \tag{1.54}$$

because the rightmost operator will always be an annihilator that kills the vacuum.

For the contractions, we have four elementary combinations:

[5] This is to be distinguished from the anti-commutator $\{X, Y\}$.

1. $X = a_p, \quad Y = a_q$:

$$\overbrace{a_p a_q} = a_p a_q - \{a_p a_q\} = a_p a_q - a_p a_q = 0\,, \tag{1.55}$$

2. $X = a_p^\dagger, \quad Y = a_q^\dagger$:

$$\overbrace{a_p^\dagger a_q^\dagger} = a_p^\dagger a_q^\dagger - \{a_p^\dagger a_q^\dagger\} = a_p^\dagger a_q^\dagger - a_p^\dagger a_q^\dagger = 0\,, \tag{1.56}$$

3. $X = a_p^\dagger, \quad Y = a_q$:

$$\overbrace{a_p^\dagger a_q} = a_p^\dagger a_q - \{a_p^\dagger a_q\} = a_p^\dagger a_q - a_p^\dagger a_q = 0\,, \tag{1.57}$$

4. $X = a_p, \quad Y = a_q^\dagger$:

$$\overbrace{a_p a_q^\dagger} = a_p a_q^\dagger - \{a_p a_q^\dagger\} = a_p a_q^\dagger + a_q^\dagger a_p = \{a_p, a_q^\dagger\} = \delta_{pq}\,. \tag{1.58}$$

In the first three cases, the operator string is already in normal order, so it makes sense that the contractions vanish. In the fourth case, $\langle\varnothing|\,\{a_p a_q^\dagger\}\,|\varnothing\rangle = 0$ implies that the contraction is equal to the vacuum expectation value of the operator,

$$\langle\varnothing|\,a_p a_q^\dagger\,|\varnothing\rangle = \overbrace{a_p a_q^\dagger}\,\langle\varnothing\,|\,\varnothing\rangle\ , \tag{1.59}$$

which vanishes unless (reading from right to left) we create and then annihilate a fermion in the same state p.

The generalization of these considerations to longer strings of creators and annihilators is provided by Wick's theorem [88, 107], which provides a convenient algorithm for expanding an operator string in products of normal-ordered operators and contractions as follows:

$$X_1 \cdots X_N \equiv \{X_1 \cdots X_N\}$$

$$
\begin{aligned}
&+ \overbrace{X_1 X_2}\,\{X_3 \cdots X_N\} - \overbrace{X_1 X_3}\,\{X_2 X_4 \cdots X_N\} \\
&\quad + \text{all other single contractions} \\
&+ \left(\overbrace{X_1 X_2}\,\overbrace{X_3 X_4} - \overbrace{X_1 X_3}\,\overbrace{X_2 Y_4} \right) \{X_5 \cdots X_N\} \\
&\quad + \text{all other double contractions} \\
&+ \text{all triple contractions} \\
&\cdots \\
&+ \text{all full contractions}\,. \qquad (1.60)
\end{aligned}
$$

Here we have assumed that the string consists of an even number of operators, so that it can be fully contracted.

For example,

$$
a_p^\dagger a_q^\dagger a_s a_r = \left\{ a_p^\dagger a_q^\dagger a_s a_r \right\} \qquad (1.61)
$$

because the operator is already in normal ordered form and all contractions vanish in this case. Another example is

$$
\begin{aligned}
a_p a_q a_s^\dagger a_r^\dagger &= \left\{ a_p a_q a_s^\dagger a_r^\dagger \right\} \\
&\quad - \overbrace{a_p a_r^\dagger} \left\{ a_s^\dagger a_q \right\} + \overbrace{a_p a_s^\dagger} \left\{ a_r^\dagger a_q \right\} + \overbrace{a_q a_r^\dagger} \left\{ a_s^\dagger a_p \right\} - \overbrace{a_q a_s^\dagger} \left\{ a_r^\dagger a_p \right\} \\
&\quad + \overbrace{a_p a_r^\dagger}\,\overbrace{a_q a_s^\dagger} - \overbrace{a_p a_s^\dagger}\,\overbrace{a_q a_r^\dagger} \\
&= - \delta_{pr} \left\{ a_s^\dagger a_q \right\} + \delta_{ps} \left\{ a_r^\dagger a_q \right\} + \delta_{qr} \left\{ a_s^\dagger a_p \right\} - \delta_{qs} \left\{ a_r^\dagger a_p \right\} \\
&\quad + \delta_{pr}\delta_{qs} - \delta_{ps}\delta_{qr}\,. \qquad (1.62)
\end{aligned}
$$

A very useful corollary of Wick's theorem exists for products of normal-ordered operators

(see [41, 107]):

$$\begin{aligned}\{X_1\cdots X_N\}\{Y_1\cdots Y_M\} \equiv &\{X_1\cdots X_N Y_1\cdots Y_M\} \\ &+ \overbrace{X_N Y_1}\{X_1\cdots X_{N-1}Y_2\cdots Y_M\} - \overbrace{X_N Y_2}\{X_1\cdots X_{N-1}Y_1Y_3\cdots Y_M\} \\ &\quad + \text{all other single contractions} \\ &+ \left(\overbrace{X_N Y_1}\overbrace{X_{N-1}Y_2} - \overbrace{X_N Y_2}\overbrace{X_{N-1}Y_1}\right)\{X_1\cdots X_{N-2}Y_3\cdots Y_M\} \\ &\quad + \text{all other double contractions} \\ &+ \text{all triple contractions} \\ &\cdots . \end{aligned} \tag{1.63}$$

We can expand the product by pairwise contracting one operator from each of the strings. It is easy to see that if there are N operators in the first and M operators in the second string, the expansion will contain products of length $|N-M|$ through $N+M$. Products of three or more normal-ordered operators can be evaluated by using Eq. (1.63) recursively.

As examples, we evaluate

$$\begin{aligned}\{a_p^\dagger a_q\}\{a_r^\dagger a_s\} =&\{a_p^\dagger a_r^\dagger a_s a_q\} + \overbrace{a_q a_r^\dagger}\{a_p^\dagger a_s\} \\ =&\{a_p^\dagger a_r^\dagger a_s a_q\} + \delta_{qr}\{a_p^\dagger a_s\}\end{aligned} \tag{1.64}$$

and

$$\begin{aligned}\{a_p a_q\}\{a_r^\dagger a_s^\dagger\} = &-\{a_r^\dagger a_s^\dagger a_q a_p\} \\ &- \overbrace{a_q a_r^\dagger}\{a_s^\dagger a_p\} + \overbrace{a_q a_s^\dagger}\{a_r^\dagger a_p\} + \overbrace{a_p a_r^\dagger}\{a_s^\dagger a_p\} - \overbrace{a_p a_s^\dagger}\{a_r^\dagger a_p\}\end{aligned}$$

$$
\begin{aligned}
&+ \overbracket{a_q a_r^\dagger} \overbracket{a_p a_s^\dagger} - \overbracket{a_p a_r^\dagger} \overbracket{a_q a_s^\dagger} \\
&= - \{a_r^\dagger a_s^\dagger a_q a_p\} \\
&\quad - \delta_{qr}\{a_s^\dagger a_p\} + \delta_{qs}\{a_r^\dagger a_p\} + \delta_{pr}\{a_s^\dagger a_p\} - \delta_{ps}\{a_r^\dagger a_p\} \\
&\quad + \delta_{qr}\delta_{ps} - \delta_{pr}\delta_{qs} \, .
\end{aligned} \tag{1.65}
$$

We now turn to define the normal product of operators with respect to the Fermi vacuum $|\Phi_0\rangle$ in an analogous way as for the vacuum $|\varnothing\rangle$. As discussed in Section 1.3.6, the killing condition for $|\Phi_0\rangle$ turns into two separate conditions for hole and particle states, Eqs. (1.52) and (1.51). To make the analogy with the true vacuum, we can introduce new creation and annihilation operators for the Fermi vacuum by defining

$$b_i^\dagger \equiv a_i \tag{1.66a}$$

$$b_i \equiv a_i^\dagger \tag{1.66b}$$

$$b_a^\dagger \equiv a_a^\dagger \tag{1.66c}$$

$$b_a \equiv a_a \tag{1.66d}$$

where i and a denote hole and particle indices, respectively, as introduced in Sec. 1.3.6. Equation (1.66a) states that annihilation of a fermion in the state i below the Fermi level is equivalent to creating a hole in the Fermi vacuum. Similarly, creating a particle in the state i below the Fermi level is analogous to destroying a hole in Eq. (1.66b). For the unoccupied states above the Fermi level the creation and annihilation operators remain unchanged.

Since the killing condition in the new creators and annihilators is once again simply given

by

$$b_p \left|\Phi_0\right\rangle = 0 \tag{1.67}$$

for all single-particle basis states, the discussion of the elementary contractions is exactly the same as above, and the only non-vanishing contraction is

$$\overbrace{b_p b_q^\dagger} = \delta_{pq} \,. \tag{1.68}$$

Reverting to the original operators, this means for particle indices that

$$\overbrace{b_a b_b^\dagger} = \overbrace{a_a a_b^\dagger} = \delta_{ab} \,, \tag{1.69}$$

and for hole indices

$$\overbrace{b_i b_j^\dagger} = \overbrace{a_i^\dagger a_j} = \delta_{ij} \,. \tag{1.70}$$

We can generalize these contractions to arbitrary single particle states with the help of occupation numbers: Then

$$\overbrace{a_p a_q^\dagger} = (1 - n_p)\delta_{pq} \,, \tag{1.71}$$

$$\overbrace{a_p^\dagger a_q} = n_p \delta_{pq} \,. \tag{1.72}$$

1.3.8 Hamiltonians and General Observables in Second-Quantized Form

Let H be a general Hamiltonian for an A-body system, consisting of up to three-body interaction terms:

$$H = H^{[1]} + H^{[2]} + H^{[3]} \,. \tag{1.73}$$

In this work, we will consider both schematic Hamiltonians (usually without three-body parts) and realistic nuclear Hamiltonians consisting of kinetic terms as well as two- and three-body interactions, for which

$$H^{[1]} = T^{[1]} \,, \tag{1.74}$$

$$H^{[2]} = T^{[2]} + V^{[2]} \,, \tag{1.75}$$

$$H^{[3]} = V^{[3]} \,. \tag{1.76}$$

There are one- and two-body kinetic energy terms because we will be using the intrinsic kinetic energy

$$T_{\text{int}} = T - T_{\text{cm}} = \left(1 - \frac{1}{A}\right) \sum_i \frac{\vec{p}_i^{\,2}}{2m} - \frac{1}{A} \sum_{i \neq j}^{A} \frac{\vec{p}_i \cdot \vec{p}_j}{m} \,. \tag{1.77}$$

Note that A is generally to be understood as a particle-number operator [38], although this subtlety doesn't matter when we work with Hilbert spaces with fixed particle numbers as in this work.

In second-quantized form, we can write the individual contributions in normal ordering

with respect to the true vacuum as

$$H^{[1]} = \sum_{pq} \langle p| h^{[1]} |q\rangle \, a_p^\dagger a_q \,, \tag{1.78}$$

$$H^{[2]} = \frac{1}{4} \sum_{pqrs} \langle pq| h^{[2]} |rs\rangle \, a_p^\dagger a_q^\dagger a_s a_r \,, \tag{1.79}$$

$$H^{[3]} = \frac{1}{36} \sum_{pqrstu} \langle pqr| h^{[3]} |stu\rangle \, a_p^\dagger a_q^\dagger a_r^\dagger a_u a_t a_s \tag{1.80}$$

(note the usual convention for the index ordering in the matrix elements and the annihilation operators). Here, we have assumed that the matrix elements defining the two- and three-body terms are antisymmetrized and obey

$$\langle pq| h^{[2]} |rs\rangle = -\langle qp| h^{[2]} |rs\rangle = -\langle pq| h^{[2]} |sr\rangle = \langle qp| h^{[2]} |sr\rangle \,, \tag{1.81}$$

$$\begin{aligned} \langle pqr| h^{[3]} |stu\rangle &= \langle qrp| h^{[3]} |stu\rangle = \langle rpq| h^{[3]} |stu\rangle \\ &= -\langle qpr| h^{[3]} |stu\rangle = -\langle prq| h^{[3]} |stu\rangle = -\langle rqp| h^{[3]} |stu\rangle \\ &= \ldots \text{ (additional permutations)} \end{aligned} \tag{1.82}$$

Using a single Slater determinant $|\Phi\rangle$ as the reference state, we can use Wick's theorem (cf. Section 1.3.7) to express the Hamiltonian in terms of normal–ordered operators:

$$H = E + \sum_{pq} f_{pq} \{a_p^\dagger a_q\} + \frac{1}{4} \sum_{pqrs} \Gamma_{pqrs} \{a_p^\dagger a_q^\dagger a_s a_r\} + \frac{1}{36} \sum_{pqrstu} W_{pqrstu} \{a_p^\dagger a_q^\dagger a_r^\dagger a_u a_t a_s\} \,. \tag{1.83}$$

To obtain the individual normal–ordered contributions in Eq. (1.83), let us first look at the

one–body term (1.78):

$$
\begin{aligned}
H^{[1]} &= \sum_{pq} \langle p| h^{[1]} |q\rangle \, a_p^\dagger a_q = \sum_{pq} \langle p| h^{[1]} |q\rangle \left(\{a_p^\dagger a_q\} + n_p \delta_{pq} \right) \\
&= \sum_{pq} \langle p| h^{[1]} |q\rangle \, \{a_p^\dagger a_q\} + \sum_{p} \langle p| h^{[1]} |p\rangle \, n_p \\
&= \sum_{pq} \langle p| h^{[1]} |q\rangle \, \{a_p^\dagger a_q\} + \sum_{i} \langle i| h^{[1]} |i\rangle \ . \qquad (1.84)
\end{aligned}
$$

Thus, we obtain contributions to the normal-ordered zero- and one-body parts.

For the two-body operator (1.79), Wick's theorem (1.60) yields

$$
\begin{aligned}
a_p^\dagger a_q^\dagger a_s a_r &= \{a_p^\dagger a_q^\dagger a_s a_r\} \\
&\quad + \{a_p^\dagger \overbracket{a_q^\dagger a_s} a_r\} + \{a_p^\dagger \overbracket{a_q^\dagger a_s a_r}\} + \{\overbracket{a_p^\dagger a_q^\dagger} a_s a_r\} + \{\overbracket{a_p^\dagger a_q^\dagger a_s} a_r\} \\
&\quad + \{\overbracket{a_p^\dagger \overbracket{a_q^\dagger a_s} a_r}\} + \{\overbracket{a_p^\dagger \overbracket{a_q^\dagger a_s a_r}}\} \\
&= \{a_p^\dagger a_q^\dagger a_s a_r\} \\
&\quad + n_q \delta_{qs} \{a_p^\dagger a_r\} - n_q \delta_{qr} \{a_p^\dagger a_s\} - n_p \delta_{ps} \{a_q^\dagger a_r\} + n_p \delta_{pr} \{a_q^\dagger a_s\} \qquad (1.85) \\
&\quad + n_p n_q \left(\delta_{pr} \delta_{qs} - \delta_{ps} \delta_{qr} \right) , \qquad (1.86)
\end{aligned}
$$

so the two–body operator can be decomposed into a sum of a normal-ordered two–body operator, a collection of one–body operators and two zero–body terms (scalars). Inserting this expansion into Eq. (1.79)

$$
\begin{aligned}
H^{[2]} &= \frac{1}{4} \sum_{pqrs} \langle pq| h^{[2]} |rs\rangle \, a_p^\dagger a_q^\dagger a_s a_r \\
&= \frac{1}{4} \sum_{pqrs} \langle pq| h^{[2]} |rs\rangle \, \{a_p^\dagger a_q^\dagger a_s a_r\}
\end{aligned}
$$

$$
\begin{aligned}
&+ \frac{1}{4}\Bigg(\sum_{pqrs} n_q \delta_{qs} \langle pq| h^{[2]} |rs\rangle \{a_p^\dagger a_r\} - n_q \delta_{qr} \langle pq| h^{[2]} |rs\rangle \{a_p^\dagger a_s\} \\
&- n_p \delta_{ps} \langle pq| h^{[2]} |rs\rangle \{a_q^\dagger a_r\} + n_p \delta_{pr} \langle pq| h^{[2]} |rs\rangle \{a_q^\dagger a_s\} \\
&+ n_p n_q \delta_{pr} \delta_{qs} \langle pq| h^{[2]} |rs\rangle - n_p n_q \delta_{ps} \delta_{qr} \langle pq| h^{[2]} |rs\rangle\Bigg) \\
= &\frac{1}{4} \sum_{pqrs} \langle pq| h^{[2]} |rs\rangle \{a_p^\dagger a_q^\dagger a_s a_r\} \\
&+ \frac{1}{4} \sum_{pqi} \Big(\langle pi| h^{[2]} |qi\rangle - \langle pi| h^{[2]} |iq\rangle - \langle ip| h^{[2]} |qi\rangle + \langle ip| h^{[2]} |iq\rangle\Big) \{a_p^\dagger a_q\} \\
&+ \frac{1}{4} \sum_{ij} \Big(\langle ij| h^{[2]} |ij\rangle - \langle ij| h^{[2]} |ji\rangle\Big) \\
= &\frac{1}{4} \sum_{pqrs} \langle pq| h^{[2]} |rs\rangle \{a_p^\dagger a_q^\dagger a_s a_r\} + \sum_{pqi} \langle pi| h^{[2]} |qi\rangle \{a_p^\dagger a_q\} + \frac{1}{2} \sum_{ij} \langle ij| h^{[2]} |ij\rangle
\end{aligned} \tag{1.87}
$$

where i and j refer to holes states (see Table 1.1). The calculation for the three-body part is analogous but much more tedious due to the much greater number of possible contractions that need to be evaluated — without going into details, we see that it contributes to the zero-, one- and two-body parts of the normal-ordered H.

Ultimately, we obtain

$$E = \sum_i \langle i| t |i\rangle + \frac{1}{2} \sum_{ij} \langle ij| v |ij\rangle + \frac{1}{6} \sum_{ijk} \langle ijk| w |ijk\rangle \tag{1.88a}$$

$$f_{pq} = \langle p| t |q\rangle + \sum_i \langle pi| v |qi\rangle + \frac{1}{2} \sum_{ij} \langle pij| w |qij\rangle \tag{1.88b}$$

$$\Gamma_{pqrs} = \langle pq| v |rs\rangle + \sum_i \langle pqi| w |rsi\rangle \tag{1.88c}$$

$$W_{pqrstu} = \langle pqr| w |uts\rangle \ . \tag{1.88d}$$

All summations are limited to states that are occupied in the reference state $|\Phi\rangle$. We see that, as the name suggest, E is just the expectation value of H in the reference state, and

f is the usual mean-field Hamiltonian, as used in the Hartree-Fock method, for instance. The zero-, one-, and two-body components of the Hamiltonian all encompass in-medium contributions from the $3N$ interaction.

Other observables can be handled exactly like the Hamiltonian. The second-quantized form of a general k-body operator, can be written as

$$O^{[k]} = \left(\frac{1}{k!}\right)^2 \sum_{\substack{p_1 \cdots p_k \\ q_1 \cdots q_k}} \langle p_1 \cdots p_k | \, o^{[k]} \, | q_1 \cdots q_k \rangle \, a^\dagger_{p_1} \cdots a^\dagger_{p_k} a_{q_k} \cdots a_{q_1} \tag{1.89}$$

where we once again assume that the matrix elements have been antisymmetrized. Using Wick's theorem (1.60), we can normal order such operators with respect to arbitrary Slater determinant reference states.

1.3.9 Full Configuration Interaction Theory

In principle, we now have all ingredients for setting up the Hamiltonian matrix and trying to solve the (stationary) many-body Schrödinger equation through an exact diagonalization — this is the so-called Full Configuration Interaction (FCI) method [88], which is also known as No-Core Full Configuration (NCFC) or the No-Core Shell Model (NCSM) in nuclear physics [5, 73].

To perform an FCI calculation, one first needs to select an appropriate single-particle basis for describing bound systems, usually the spherical harmonic oscillator, and construct a complete orthonormal basis of Slater determinants by distributing the nucleons of a specific nucleus over the available single-particle levels in all possible configurations. As explained in Section 1.3.6, it is useful to organize the basis in terms of particle-hole excitations of a reference Slater determinant $|\Phi_0\rangle$ to aid the convergence of the expansion for the exact

eigenstates of H. Schematically, we have

$$|\Psi\rangle = C_0 |\Phi_0\rangle + \sum_{ai} C_i^a |\Phi_i^a\rangle + \sum_{abij} C_{ij}^{ab} |\Phi_{ij}^{ab}\rangle + \cdots \equiv (C_0 + \hat{C}) |\Phi_0\rangle \tag{1.90}$$

where the ellipsis three-particle-three-hole (3p3h) and higher excitations, and where we have introduced the so-called correlation operator

$$\hat{C} = \sum_{ai} C_i^a a_a^\dagger a_i + \frac{1}{4} \sum_{abij} C_{ij}^{ab} a_a^\dagger a_b^\dagger a_j a_i + \cdots . \tag{1.91}$$

Our requirement of orthonormality gives

$$\langle \Psi_0 | \Psi_0 \rangle = \sum_{ai} |C_i^a|^2 + \sum_{abij} |C_{ij}^{ab}|^2 + \cdots \equiv \sum_I |C_I|^2 = 1 , \tag{1.92}$$

where the collective index I runs over all sectors of the many-body basis. Expanding the eigenstates in the many-body Schrödinger Equation (1.1) in terms of the Slater determinant basis configurations, we obtain

$$H \sum_I C_I |\Phi_I\rangle = E \sum_I C_I |\Phi_I\rangle \tag{1.93}$$

Projecting Eq. (1.93) onto $\langle \Phi_{I'} |$, we see that

$$\langle \Phi_{I'} | H \sum_I C_I |\Phi_I\rangle = E \langle \Phi_{I'} | \sum_I C_I |\Phi_I\rangle \tag{1.94}$$

By rearranging the formula, we obtain

$$\sum_I C_I \langle \Phi_{I'} | H | \Phi_I \rangle = E \sum_I C_I \langle \Phi_{I'} | | \Phi_I \rangle \tag{1.95}$$

$$= E \sum_I C_I \delta_{II'} \tag{1.96}$$

$$= E C_{I'} \tag{1.97}$$

which precisely corresponds to the eigenvalue problem in linear algebra, commonly expressed as $H\vec{C} = E\vec{C}$. The elements of the Hamiltonian are given by

$$H_{II'} = \langle \Phi_I | H | \Phi_{I'} \rangle \ ,$$

and they can be evaluate with the help of Wick's theorem: Note that

$$a_a^\dagger a_b^\dagger \cdots a_j a_i = \{ a_a^\dagger a_b^\dagger \cdots a_j a_i \} \tag{1.98}$$

because we cannot contract particle $(a, b, \ldots)$ and hole $(i, j, \ldots)$ indices, so we can write the matrix elements as

$$H_{II'} = \langle \Phi_0 | \{ a_{i_1}^\dagger \cdots a_{i_k}^\dagger a_{a_k} \cdots a_{a_1} \} H \{ a_{b_1}^\dagger \cdots a_{b_{k'}}^\dagger a_{j_{k'}} \cdots a_{j_1} \} | \Phi_0 \rangle \ , \tag{1.99}$$

where I and I' are understood as $k\mathrm{p}k\mathrm{h}$ and $k'\mathrm{p}k'\mathrm{h}$ basis configurations, respectively.

In a practical many-body calculation, we first need to truncate the single-particle basis, which leads to a finite number of Slater determinants and thus a Hamiltonian matrix with finite size. In principle, eigenstates can then be obtained by directly diagonalizing the trun-

cated matrix, usually with Lanczos [58] or Arnoldi methods [3], since we are mostly interested in a few low-lying states. However, the basis dimension for the matrices and eigenvectors scales as $\binom{N}{A} = \frac{N!}{A!(N-A)!}$ with the single-particle basis size N and the nucleon number A, hence the diagonalization quickly becomes impractical even for modern supercomputers as A grows. Therefore, we need to truncate the basis of Slater determinants.

The No-Core Shell Model (NCSM) in nuclear physics uses an (oscillator) energy based truncation instead that can guarantee an exact factorization of the center of mass and intrinsic wave functions, but does not change the exponential scaling of the method [5].

Another option is to restrict the type of excitations that are included in the basis. If only singles and doubles excitations are considered, for example, then we get the configuration singles doubles (CISD) approximation

$$|\Psi_0^{CISD}\rangle = C_0 |\Phi_0\rangle + \sum_{ia} C_i^a |\Phi_i^a\rangle + \sum_{ijab} C_{ij}^{ab} |\Phi_{ij}^{ab}\rangle \ , \tag{1.100}$$

for which the basis dimension scales as $O(N_p^2 N_h^2)$ with the number of hole ($N_h = A$) and the number of particle states ($N_p = N - N_h = N - A$). Lanczos or Arnoldi iterations can then be performed at a cost of $O(N_p^4 N_h^4)$, but there are alternative methods with similar scaling that are more efficient for incorporating correlations into the target many-body state, like Coupled Cluster [88] or the In-Medium Similarity Renormalization Group [39, 41], which will be discussed in later chapters of this work.

Finding optimal ways to capture many-body correlations is a widely studied topic (see, e.g., [40] and references therein), and there is presently no one-size-fits-all solution. For specific applications, the choice of approximation depends on the strengths and weaknesses of each method.

Chapter 2

The Similarity Renormalization Group

Nuclear many-body calculations are challenging because of the influence of correlation effects that arise from the strong repulsion of the nuclear force at small distances as well as the tensor force, as mentioned in chapter 1. This leads to a coupling of many-body states with high and low momentum. To address this issue, we can use renormalization group (RG) techniques to "tame" these correlation effects. RG methods are naturally complementary to EFT approaches, and in our case, to the sequence of EFTs for the strong interaction. This is because they enable the systematic adjustment of resolution scales and cutoffs in these theories, allowing for the connection of various levels within the EFT hierarchy. Additionally, RG methods also offer a range of diagnostic tools for checking the fundamental consistency of power counting schemes in EFTs.

In the field of nuclear many-body theory, the most commonly used method is the Similarity Renormalization Group (SRG), which will be discussed in more detail in this chapter. This technique differs from the Wilsonian [108] RG approach, which eliminates high-momentum degrees of freedom through decimation. The SRG method separates the physics of low and high momenta through continuous unitary transformations. It is important to note that this concept is not limited to RG applications, as it can be used to modify a many-

body Hamiltonian or other relevant observables according to specific requirements, such as extracting eigenvalues [37, 39] or imposing certain operator structures [10, 13, 48, 92, 93], which will be discussed in the next chapter.

2.1 Flow Equation

We utilize the method of SRG transformations to "soften" the interactions between nucleons. The transformation process involves a series of unitary transformations, which allows for the evaluation of the Hamiltonian's evolution or flow as a function of the parameter s,

$$H_s = U_s H_0 U_s^\dagger \equiv T_{\text{rel}} + V_s \tag{2.1}$$

where T_{rel} is the relative kinetic energy[1], , H_0 is the initial Hamiltonian, and U_s is the unitary transformation. Note that we make the choise to absorb induced operators from the evolution of T_{rel} into V_s.

Instead of making an ansatz for U_s, we implement SRG transformations through the use of the flow equation formalism, as introduced by Wegner [99, 100]. We find the flow equation by taking the derivative of Eq. (2.1) with respect to s,

$$\begin{aligned}
\frac{dH_s}{ds} &= \frac{dU_s}{ds} H_0 U_s^\dagger + U_s H_0 \frac{dU_s^\dagger}{ds} \\
&= \frac{dU_s}{ds} U_s^\dagger U_s H_0 U_s^\dagger + U_s H_0 U_s^\dagger U_s \frac{dU_s^\dagger}{ds} \\
&= \frac{dU_s}{ds} U_s^\dagger H_s + H_s U_s \frac{dU_s^\dagger}{ds}
\end{aligned} \tag{2.2}$$

[1] Since all fundamental interactions are translationally invariant, the center-of-mass kinetic energy (T_{cm}) commutes with the other operators in Eq.(2.1).

where we have plugged in $\mathbb{1} = U_s U_s^\dagger = U_s^\dagger U_s$ in the second line, and we also have used

$$\frac{d}{ds}(\mathbb{1}) = \frac{d}{ds}\left(U_s U_s^\dagger\right) = 0 \tag{2.3}$$

which implies

$$\frac{dU_s}{ds}U_s^\dagger = -U_s\frac{dU_s^\dagger}{ds} \tag{2.4}$$

Defining the anti-Hermitian operator

$$\eta_s \equiv \frac{dU_s}{ds}U_s^\dagger = -\eta_s\,, \tag{2.5}$$

Eq. (2.2) can be rewritten as

$$\begin{aligned}\frac{dH_s}{ds} &= \eta_s H_s + H_s\eta_s^\dagger = \eta_s H_s - H_s\eta_s \\ &= [\eta_s, H_s]\end{aligned} \tag{2.6}$$

The SRG flow equation for the Hamiltonian describes the way a system changes over time when it is subject to the *dynamical generator* η_s. Note that because of the unitary nature of the transformation, the Hamiltonian's spectrum is conserved unless we need to introduce approximations.

By integrating the flow equation (2.6) for $s \to \infty$, we can achieve the desired transformation of the Hamiltonian by selecting an appropriate generator η_s. Wegner originally proposed a type of generators known (henceforth referred to as Wegner generators), given by

$$\eta_s = \left[H_s^d, H_s^{od}\right] \tag{2.7}$$

which is constructed by dividing the Hamiltonian into a diagonal part (H_s^d) we want to keep as $s \to \infty$, and an off-diagonal part (H_s^{od}) we want to suppress. Several options for splitting the Hamiltonian are available for consideration [1, 9, 50, 52], and one can even generalize this idea and consider the commutator of an arbitrary Hermitian operator G_s with H_s, e.g., for unmixing symmetries [48]. In the following, we use $H_s^d = T_{\text{rel}}$, a constant, for which the flow equation becomes

$$\frac{dH_s}{ds} = [[T_{\text{rel}}, H_s], H_s] \tag{2.8}$$

The Eq. (2.8) represent operator equations that are independent of any specific basis. The equation can be evaluated numerically by projecting onto a suitable basis and converting it into a matrix differential equation. In the case of two-nucleon system, a partial-wave momentum basis is a convenient, accurate, and straightforward choice, since our generator is based on T_{rel}.

2.2 SRG Decoupling

One of the major consequence of the SRG is that the Hamiltonian will be driven to a diagonal or band-diagonal form in a chosen basis. To see this, we consider the Wegner generator and split the Hamiltonian matrix into diagonal and off-diagonal pieces

$$\begin{aligned} H_s^d &= \text{diag}(H_s) \\ H_s^{od} &= H_s - H_s^d \end{aligned} \tag{2.9}$$

Suppressing the s dependence of the quantities, Eq. (2.6) can then be written as

$$\begin{aligned}
\frac{d}{ds}\langle i|H|j\rangle &= \langle i|[\eta, H]|j\rangle \\
&= \sum_k \Big(\langle i|\eta|k\rangle\langle k|H|j\rangle - \langle i|H|k\rangle\langle k|\eta|j\rangle\Big) \\
&= \sum_k \Big(\langle i|\eta|k\rangle\langle k|H^d + H^{od}|j\rangle - \langle i|H^d + H^{od}|k\rangle\langle k|\eta|j\rangle\Big) \\
&= -(E_i - E_j)\langle i|\eta|j\rangle + \sum_k \Big(\langle i|\eta|k\rangle\langle k|H^{od}|j\rangle - \langle i|H^{od}|k\rangle\langle k|\eta|j\rangle\Big)
\end{aligned} \tag{2.10}$$

where we have used the completeness of the basis, $\mathbb{1} = \sum_k |k\rangle\langle k|$, in the second equality above and, in the third equality, we have used that $H^d|k\rangle = E_k|k\rangle$ by construction. Then we also have

$$\langle i|\eta|j\rangle = \langle i|\Big[H^d, H^{od}\Big]|j\rangle = (E_i - E_j)\langle i|H^{od}|j\rangle\ . \tag{2.11}$$

Inserting this into the Eq. (2.10), we obtain

$$\frac{d}{ds}\langle i|H|j\rangle = -(E_i - E_j)^2\langle i|H^{od}|j\rangle + \sum_k (E_i + E_j - 2E_k)\langle i|H^{od}|k\rangle\langle k|H^{od}|j\rangle \tag{2.12}$$

For the diagonal elements ($i = j$), Eq. (2.12) becomes

$$\frac{d}{ds}\langle i|H|i\rangle = 2\sum_k (E_i - E_k)|\langle i|H^{od}|k\rangle|^2 \tag{2.13}$$

where $\langle i|\, H^{od}\, |i\rangle = 0$, and

$$\begin{aligned}
\frac{d}{ds}\sum_i |\langle i|\, H\, |i\rangle|^2 &= 2\sum_i \langle i|\, H\, |i\rangle\, \frac{d}{ds}\langle i|\, H\, |i\rangle \\
&= 2\sum_{i,k} E_i(E_i - E_k)|\langle i|\, H^{od}\, |k\rangle|^2 \\
&= 4\sum_{i\neq k} E_i(E_i - E_k)^2|\langle i|\, H^{od}\, |k\rangle|^2 \\
&= 2\sum_{i\neq k} (E_i - E_k)^2|\langle i|\, H^{od}\, |k\rangle|^2 \\
&\geq 0\,.
\end{aligned} \tag{2.14}$$

Due to unitary, the trace of a matrix is fixed under the evolution

$$\begin{aligned}
\mathrm{Tr}\, H^2 = \text{const.} &= \sum_{i,j} |\langle i|\, H\, |j\rangle|^2 \\
&= \sum_i |\langle i|\, H\, |i\rangle|^2 + \sum_{i\neq j} |\langle i|\, H\, |j\rangle|^2
\end{aligned} \tag{2.15}$$

Therefore, we obtain

$$\begin{aligned}
\frac{d}{ds}\sum_{i\neq j} |\langle i|\, H\, |j\rangle|^2 &= -\frac{d}{ds}\sum_i |\langle i|\, H\, |i\rangle|^2 \\
&\leq 0\,.
\end{aligned} \tag{2.16}$$

This means the off-diagonal matrix elements will decrease and, the transformation caused by η effectively suppresses H^{od}. Thinking further, this means that the norm of the absolute value of H^{od} will become small for some s_0. For even larger values $s > s_0$, we can then disregard the second term of the flow equation (2.12) compared to the first term, and this

implies

$$\frac{dE_i}{ds} = \frac{d}{ds}\langle i|\, H^d\, |i\rangle = 2\sum_k (E_i - E_k)|\langle i|\, H^{od}\, |k\rangle|^2 \approx 0 \tag{2.17}$$

and

$$\frac{d}{ds}\langle i|\, H^{od}\, |j\rangle \approx (E_i - E_j)^2\, \langle i|\, H^{od}\, |j\rangle \tag{2.18}$$

respectively. This means that the diagonal elements of the matrix will remain nearly constant in the asymptotic region,

$$E_s \approx E_{s_0}, \qquad s > s_0\,, \tag{2.19}$$

which allows us to integrate Eq. (2.18):

$$\langle i|\, H_s^{od}\, |j\rangle \approx \langle i|\, H_{s_0}^{od}\, |j\rangle\, e^{-(E_i - E_j)^2 (s - s_0)}, \qquad s > s_0\,. \tag{2.20}$$

It is revealed that the characteristic decay scale of each element is dependent on the square of the energy difference between the states it connects, e.g. $(E_i - E_j)^2$: States with higher energy differences will be decoupled before those with lower energy difference, thereby ensuring that the Wegner generator produces a proper RG transformation.

2.3 Evolution of Nuclear Interactions

For the sake of simplicity, let us consider a nuclear Hamiltonian that consists of the intrinsic kinetic energy and a two-nucleon interaction (cf. Section 1.3.8):

$$H_{\text{int}} = T_{\text{int}} + V^{[2]}\,. \tag{2.21}$$

T_{int} (Eq. (1.77)) can be written as a pure two-body operator

$$T_{\text{int}} = \frac{2}{A}\sum_{i<j}\frac{q_{ij}^2}{2\mu}, \qquad q_{ij} = p_i - p_j \tag{2.22}$$

where A is a particle-number operator [38], q_{ij} is the relative momentum of two nucleons, and $\mu = m/2$, the reduced two-nucleon mass (averaging the proton and neutron masses for simplicity). Thus, the Eq. (2.21) can be reexpressed as

$$H_{\text{int}} = \frac{2}{A}\sum_{i<j}\frac{q_{ij}^2}{2\mu} + \sum_{i<j} v_{ij}^{[2]} \tag{2.23}$$

When we analyze the SRG evolution of the nuclear Hamiltonian by means of the flow equation in Eq. (2.8), it is convenient to fully incorporate the flow-parameter dependency into the interaction part of the Hamiltonian, while keeping the kinetic energy piece unaltered, as in Eq. (2.1). This merely involves transferring all s-dependent component of H^d to H^{od}. As a result, we obtain a flow equation for the two-nucleon interaction that reads

$$\frac{d}{ds}v^{[2]} = \left[\eta, t^{[2]} + v^{[2]}\right]. \tag{2.24}$$

Let's now examine the flow equation (2.24) in detail. Due to the translational and rotational symmetry of the nuclear Hamiltonian, it is most convenient to work in a momentum-space partial wave basis consisting of momentum and angular momentum eigenstates, denoted as

$$|q(LS)JMTM_T\rangle\,. \tag{2.25}$$

Conservation of total angular momentum J of the nucleon pair is guaranteed by the NN

interaction's rotational symmetry, while the orbital angular momentum L is not conserved because of the nuclear tensor interaction. In general, this would also imply that the spin S of the nuclear pair need not be conserved, but it is in our case because the allowed spin couplings for two nucleons are very limited. Assuming charge symmetry breaking due to the Coulomb interaction and isospin-symmetry violations in the nuclear interaction, the matrix elements in the $T = 1$ channel are also dependent on the projection $M_T = -1, 0, 1$, which denotes the neutron-neutron, neutron-proton, and proton-proton components of nuclear Hamiltonian. For $T = 0$, only $M_T = 0$ is allowed.

As we saw in Figure 1.1, the momentum-space matrices of an interaction like Argonne V18 in the deuteron partial waves ($^3S_1$, $^3S_1$–$^3D_1$ and $^3D_1$) have strong off-diagonal elements that are caused by the repulsive core in the short-range central region of the interaction. The mixed partial wave, generated exclusively by the tensor force, also has significant matrix elements. This causes a need for large Hilbert spaces in few- and many-body calculations, even when only the lowest eigenstates are of interest: Techniques like the Lanczos algorithm (see [58] and Section 1.3.9) repeatedly act with the Hamiltonian on an arbitrary starting vector to extract eigenvalues and eigenvectors. Because of the strong off-diagonal matrix elements, any starting vector will quickly be spread out over large parts of the Hilbert space, resulting in a slow convergence of the eigenstates with respect to the Hilbert space dimension. This is the behavior we seek to address with RG methods.

In Figure 2.1, we present examples of two types of RG evolution methods that separate the low- and high-momentum components of the NN (nucleon-nucleon) interactions. The first example, as shown in Figure 2.1a, is the RG decimation method, which involves evolving the interaction to lower cutoff scales $\Lambda_0 > \Lambda_1 > \Lambda_2$ and integrating out high-momentum modes, effectively renormalizing it into smaller and smaller blocks in momentum space. This method

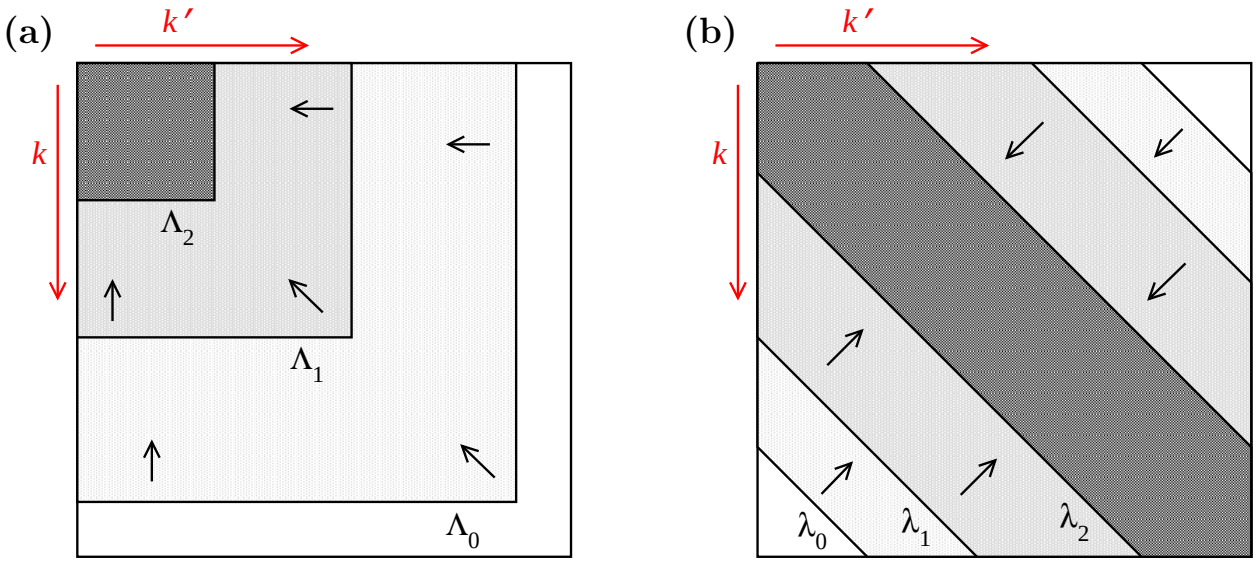

Figure 2.1: The diagram depicts two different RG evolutions of NN potentials in momentum space. In the $V_{\text{low-k}}$ approach (a), the interaction is renormalized into blocks of decreasing cutoff Λ. In contrast, the SRG evolution (b) transforms the interaction to a band-diagonal form with decreasing width λ. In the diagram, k and k' designate the relative momenta of the initial and final states, respectively. At each Λ_i and λ_i, the matrix elements outside of the corresponding blocks or bands are negligible. Therefore, it can be inferred that high and low momentum states are effectively decoupled [10].

is also known as the $V_{\text{low-k}}$ approach and was first introduced in nuclear physics during the early 2000s [10, 11]. On the other hand, Figure 2.1b displays the SRG evolution of the NN interaction to a band-diagonal form using the flow equation (2.8), where the generator is constructed from the relative kinetic energy T_{rel} in the two-nucleon system [9, 10]. Here, the SRG evolution of a system has been parameterized by a momentum with dimensions of $\lambda = s^{-1/4}$, rather than the usual parameter s, which is an indicator of the width of the band in momentum space:

$$|q' - q| \lesssim \lambda \,. \tag{2.26}$$

This suggests low- and high-momenta are decoupled as λ is decreased through the SRG. Physically, this implies that long-ranged components of the NN interactions are explicitly resolved, while the short-range components can be replaced by contact interactions [11, 33,

47, 60]. Thus, we can think of λ as a momentum resolution scale. When an NN interaction is evoved through an RG process, it leads to a universal long-range interaction, namely one-pion exchange (OPE), which is valid in the range of 1.5 fm^{-1} to 2.5 fm^{-1}. Further evolution to lower values of λ removes pieces of OPE and eventually results in a pion-less theory that is purely parameterized in terms of contact interactions.

Using the orthogonality and completeness relations for the states (2.25)

$$\langle qLSJMTM_T|\,|q'L'S'J'M'T'M'_T\rangle = \frac{\delta(q-q')}{qq'}\delta_{LL'}\delta_{SS'}\delta_{JJ'}\delta_{MM'}\delta_{TT'}\delta_{M_TM'_T}\,, \tag{2.27a}$$

$$\mathbb{1} = \sum_{LSJMTM_T}\int_0^\infty dqq^2\,|qLSJMTM_T\rangle\,\langle qLSJMTM_T|\,, \tag{2.27b}$$

we can represent the flow equation (2.24) in partial-wave form as

$$\begin{aligned}\left(-\frac{\lambda^5}{4}\right)\frac{d\,\langle qL|\,v\,|q'L'\rangle}{d\lambda} =& -(q^2-q'^2)^2\,\langle qL|\,v\,|q'L'\rangle \\ &+\sum_{\bar{L}}\int_0^\infty dpp^2(q^2+q'^2-2p^2)\,\langle qL|\,v\,|p\bar{L}\rangle\,\langle p\bar{L}|\,v\,|q'L'\rangle\end{aligned} \tag{2.28}$$

where we used $\hbar = m = 1$ and a prefactor $-\lambda^5/4$ appears due to the variables change from the flow parameter s to the resolutions scale λ. By discretizing the relative momentum variable using uniform or Gaussian quadrature meshes [80] , we can convert this integro-differential equation into a matrix flow equation. For example, the matrix elements of the relative kinetic energy operator can be represented as

$$\langle q_iL|\,t\,|q_jL'\rangle = q_i^2\delta_{q_iq_j}\delta_{LL'}$$

and the discretization transforms the continuous integration into the summation

$$\int_0^\infty dq q^2 \Rightarrow \sum_i w_i q_i^2$$

where the weights w_i depend on the choice of mesh. To simplify the calculation, we incorporate the weights and q^2 from the integral measure into the interaction matrix element, defining

$$\langle q_i L | \, \bar{v} \, | q_j L' \rangle \equiv \sqrt{w_i w_j} q_i q_j \, \langle q_i L | \, v \, | q_j L' \rangle \ . \tag{2.29}$$

As a result, the discretized flow equation can be expressed as

$$\frac{d}{d\lambda} \langle q_i L | \, \bar{v} \, | q_j L' \rangle = -\frac{4}{\lambda^5} \, \langle q_i L | \, [[t, \bar{v}], t + \bar{v}] \, | q_j L' \rangle \ . \tag{2.30}$$

As an illustration of a practical application, snapshots of the SRG transformation of the chiral N^{3}LO NN interactions by Entem and Machleidt with a cutoff Λ = 500 MeV [22, 67] are shown in Figure 2.2. The left column displays the matrix elements of the initial interaction s = 0, or $\lambda = \infty$, in the $^3S_1$ partial wave, and the corresponding deuteron wave function. The middle column and the right column are the interaction evolved to 3 fm^{-1} and then to 2 fm^{-1}, where the off-diagonal matrix elements are suppressed and the interaction is primarily confined to a block of states with $|q| \sim 2$ fm^{-1}. Furthermore, it is noted that the chiral interaction initially has much weaker off-diagonal matrix elements, while the AV18 matrix elements extend up to $|q| \sim 20$ fm^{-1}. In nuclear physics terminology, AV18 is considered as a harder interaction than the chiral interaction due to its repulsive core.

The positive impact of low-momentum potentials in nuclear many-body calculations is

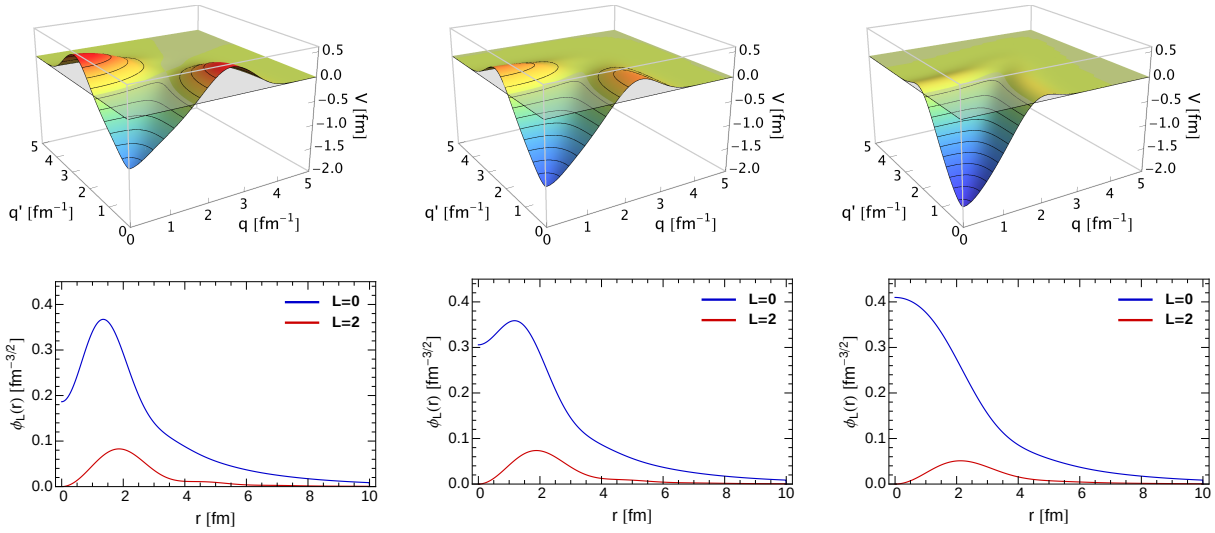

(a) $\lambda = \infty$ (b) $\lambda = 3$ fm^{-1} (b) (c) $\lambda = 2$ fm^{-1}

Figure 2.2: The SRG evolution of the chiral N^{3}LO nucleon-nucleon interaction by Entem and Machleidt [22, 67], with initial cutoff $\Lambda = 500$ MeV. In the top row, we display the momentum-space matrix elements of the interaction in the $^3S_1$ partial wave at different values of the SRG resolution scale. The initial interaction is shown in the left column at $s = 0$, or $\lambda = \infty$. In the bottom panel, we display $S-$ and $D-$wave components of the deuteron wave function that results from solving the Schrödinger equation with the corresponding SRG-evolved interaction [41].

illustrated in Figures 2.3a and 2.3b. The figures show ground-state energies of ^{4}He and ^{6}Li from exact diagonalization of the Hamiltonian matrix in the No-Core Shell Model (NCSM), one of the nuclear FCI approaches discussed in Section 1.3.9. The original potential is once again the chiral NN interaction by Entem and Machleidt that we discussed above, and it is now supplemented with a chiral $3N$ interaction — for details, we refer to [27, 49]. Although this interaction is rather soft in nuclear physics terminology, the NCSM convergence with respect to the harmonic oscillator (HO) many-body basis is slow, all while matrix dimensions are growing rapidly with both *Nmax* and the number of nucleons, as shown in Fig. 2.3c. However, SRG evolution significantly improves convergence and allows reliable extrapolation of partly converged result to the $N_{\max} \to \infty$ limit, reducing the computational cost by several orders of magnitude. Because of the SRG softening of the interaction and the use

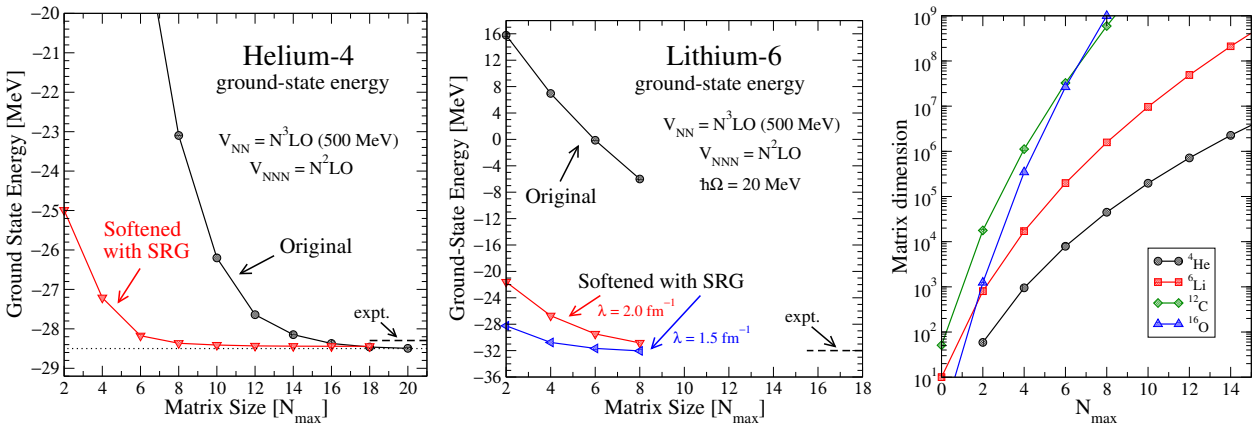

(a) (b) (c)

Figure 2.3: The convergence of the No-Core Shell Model (NCSM) calculations of the ground-state energies of ^{4}He (a) and ^{6}Li (b) is analyzed as a function of the basis size parameter $N_{\max}$ at different SRG resolution scales λ. Panel (c) illustrates the growth of the NCSM basis dimension with $N_{\max}$ for various nuclei. See Refs. [27, 49] for details.

of techniques like importance sampling [83, 86], exact diagonalization approaches can today reach nuclei with mass $A \sim 20$ [40], but the fast growth of the basis with the number of nucleons remains an obstacle in calculating even larger nuclei.

2.4 Induced Interactions

While SRG decoupling of low- and high-momentum components of nuclear interactions improves the convergence of many-body calculations, there is a price to pay for in practical applications: The evolution induces three-body and higher many-body forces. To see this, we again consider the Hamiltonian in second-quantized form (see Section 1.3.8):

$$H = \sum_{pq} T^{[1]}_{pq} a^\dagger_p a_q + \frac{1}{4} \sum_{pqrs} \left(T^{[2]} + V^{[2]} \right)_{pqrs} a^\dagger_p a^\dagger_q a_s a_r + \frac{1}{36} \sum_{pqrstu} V^{[3]}_{pqrstu} a^\dagger_p a^\dagger_q a^\dagger_r a_u a_t a_s \,. \quad (2.31)$$

To understand how the SRG generates many-body forces in an A-body space, we do not need to solve the flow equation (2.24) using the Hamiltonian given by Eq. (2.31) — we can

demonstrate the problem by considering only the two-body term:

$$\frac{dV_s}{ds} = \left[\left[\sum_{pq} T^{[1]}_{pq} a^\dagger_p a_q \sum_{pqrs} T^{[2]}_{pqrs} a^\dagger_p a^\dagger_q a_s a_r, \sum_{tuvw} V^{[2]}_{tuvw} a^\dagger_t a^\dagger_u a_w a_v\right], \sum_{ijkl} V^{[2]}_{ijkl} a^\dagger_i a^\dagger_j a_l a_k\right] + \dots . \tag{2.32}$$

Without explicitly calculating the above, let's consider the intermediate steps, the calculation of commutators: For the commutator of a one- and a two-body operator, application of Wick's theorem (1.63) yields

$$\begin{aligned}
\left[a^\dagger_p a_q, a^\dagger_r a^\dagger_s a_u a_t\right] =& a^\dagger_p a_q a^\dagger_r a^\dagger_s a_u a_t - a^\dagger_r a^\dagger_s a_u a_t a^\dagger_p a_q \\
=& a^\dagger_p a^\dagger_r a^\dagger_s a_u a_t a_q + \delta_{qr} a^\dagger_p a^\dagger_s a_u a_t - \delta_{qs} a^\dagger_p a^\dagger_r a_u a_t \\
& - a^\dagger_p a^\dagger_r a^\dagger_s a_u a_t a_q - \delta_{pt} a^\dagger_r a^\dagger_s a_u a_q + \delta_{pu} a^\dagger_r a^\dagger_s a_t a_q \\
=& \delta_{qr} a^\dagger_p a^\dagger_s a_u a_t - \delta_{qs} a^\dagger_p a^\dagger_r a_u a_t - \delta_{pt} a^\dagger_r a^\dagger_s a_u a_q + \delta_{pu} a^\dagger_r a^\dagger_s a_t a_q \,,
\end{aligned} \tag{2.33}$$

so we see that while each individual product in the commutator creates a three-body term (cf. Section 1.3.8), those terms cancel and we once again obtain a two-body operator, albeit one that appears more complicated. For the commutator of two two-body operators, however,

$$\begin{aligned}
\left[a^\dagger_p a^\dagger_q a_s a_r, a^\dagger_t a^\dagger_u a_w a_v\right] =& a^\dagger_p a^\dagger_q a_s a_r a^\dagger_t a^\dagger_u a_w a_v - a^\dagger_t a^\dagger_u a_w a_v a^\dagger_p a^\dagger_q a_s a_r \\
=& a^\dagger_p a^\dagger_q a^\dagger_t a^\dagger_u a_w a_v a_s a_r - \delta_{rt} a^\dagger_p a^\dagger_q a^\dagger_u a_w a_v a_s + \text{other single contractions} \\
& + \left(\delta_{rt}\delta_{su} - \delta_{ru}\delta_{st}\right) a^\dagger_p a^\dagger_q a_w a_v a_s \\
& - a^\dagger_p a^\dagger_q a^\dagger_t a^\dagger_u a_w a_v a_s a_r + \delta_{pv} a^\dagger_t a^\dagger_u a^\dagger_q a_w a_s a_r + \text{other single contractions} \\
& - \left(\delta_{pv}\delta_{qw} - \delta_{pw}\delta_{qv}\right) a^\dagger_t a^\dagger_u a_s a_r \,,
\end{aligned} \tag{2.34}$$

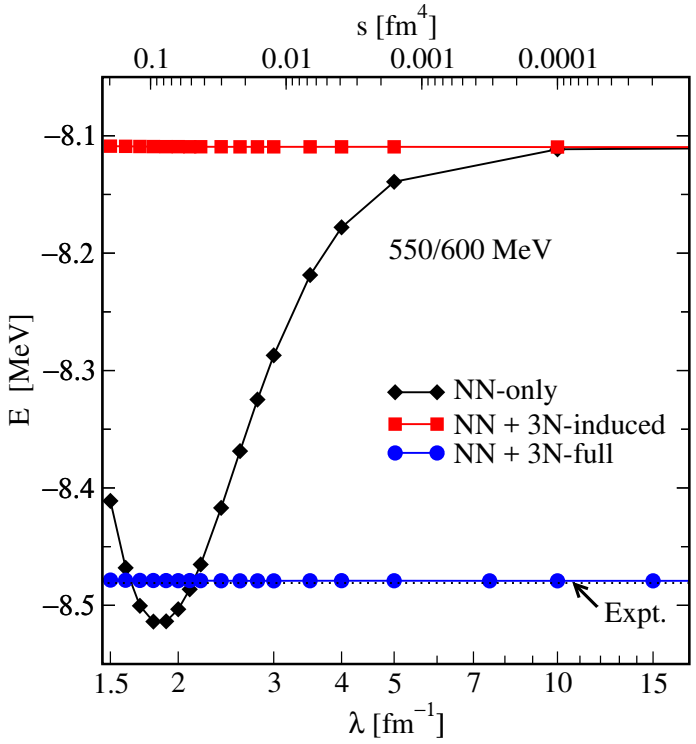

Figure 2.4: The ground state energy of ^3H as a function of the SRG resolution scale λ for chiral NN and $NN+3N$ interaction [34]. Three different typles of interactions are considered: $NN-$only, $NN+3N-$induced, and $NN+3N-$full. The experimental binding energy [98] is represented by a black dotted line. Figure adapted from Ref. [41], with original data courtesy of K. Hebeler.

i.e., the four-body operators cancel, but a new three-body operator remains. This would be true even if we started with a pure NN interaction, and as soon as after a single integration step. The induced $3N$ interaction will then induce up to $5N$ interactions in the next integration step, and so on — in general, the SRG flow induces up to A-nucleon interactions. However, these interactions are only potentially significant when analyzing A-nucleon systems [34, 35, 49, 50], and the expectation is that their importance diminishes with increasing A, so that the expected hierarchy of interactions is preserved, namely that $V^{[2]} > V^{[3]} > V^{[4]}$.

For a practical calculation of ^3H, for example, truncating the SRG flow equations the three-body level, should preserve all observables. The ^3H ground-state energies for different chiral NN and $NN+3N$ interactions, are presented in Figure 2.4. We see that the energy

changes significantly when we truncate the generator and evolving Hamiltonian at the two-body level ($NN-\text{only}$), while it remains constant when the evolution is performed at the three-body level and induced $3N$ interactions are included ($NN+3N-\text{induced}$). The same remains true when we include an initial $3N$ force whose parameters have been fit to reproduce the experimental ${}^3H$ ground-state energy ($NN+3N-\text{full}$).

Chapter 3

The In-Medium SRG

In our discussion of the SRG in chapter 2, we mentioned that we can contemplate utilizing the SRG methodology not solely for preprocessing nuclear interactions but also for imposing other desired structures on the Hamiltonian and other observables — we could even use it to calculate eigenvalues and eigenstates if we were to implement the SRG for the Hamiltonian matrix and chose H^d to be the diagonal of that matrix (see Section 2.2). This is not practical, of course, because of the exponential growth of the many-body basis (cf. Section 1.3.9) with the single-particle basis size and particle number. However, we can actually implement the SRG evolution directly at the level of the operator, and this leads us to the so-called In-Medium SRG (IMSRG), which is the subject of this chapter.

3.1 The Role of Normal Ordering

In order to implement SRG flow equations on the operator level, we first need to choose a set of "basis" operators. Ideally, we would want this set to be complete under the application of commutators, i.e., the operators would form an algebra, but unfortunately this is not possible in practice.

Because our goal is to compute energies and other observables of many-body systems, a

basis of second-quantized operator strings is a natural choice, and we could write

$$H = \sum_{pq} H_{pq} a_p^\dagger a_q + \frac{1}{4} \sum_{pqrs} H_{pqrs} a_p^\dagger a_q^\dagger a_s a_r + \cdots \tag{3.1}$$

$$\eta = \sum_{pq} \eta_{pq} a_p^\dagger a_q + \frac{1}{4} \sum_{pqrs} \eta_{pqrs} a_p^\dagger a_q^\dagger a_s a_r + \cdots, \tag{3.2}$$

dropping the particle-rank superscripts because it is clear how many particles the operators act on from the number of indices.

In Section 2.4, we saw that each evaluation of the commutator on the RHS of the operator flow equation (2.6) leads to an increase in the particle rank of $H(s)$,

$$\sum_{pqrstuvw} \eta_{pqrs} H_{tuvw} [a_p^\dagger a_q^\dagger a_s a_r, a_t^\dagger a_u^\dagger a_w a_v] \tag{3.3}$$

$$= \sum_{pqrstuv} \eta_{pqrv} H_{vstu} a_p^\dagger a_q^\dagger a_r^\dagger a_u a_t a_s + 3N \text{ terms} + NN \text{ terms}\,. \tag{3.4}$$

It should be noted that there are no induced $4N$ interaction, and that commutators involving at least one one–body operator do not result in any change in the particle rank. We cautioned that the impact of truncating these terms to "close" the flow equations can lead to significant truncation errors, and that these errors are expected to become more substantial in in systems comprising $A \geq 3$ particles.

Luckily, we also have a potential solution to this issue at our disposal: normal ordering. In Section 1.3.7, we saw that the process of normal ordering an operator with respect to a reference state, e.g., a Slater determinant, shifts parts of any second-quantized operators into terms of lower particle rank. Likewise, Wick's theorem 1.63 tells us that a large number of terms with contractions appear in the expansion of products — and therefore commutators — of normal ordered operators. For this reason, we choose to work with a basis of normal-

ordered operators,

$$\mathcal{B} \equiv \left\{ \{a_p^\dagger a_q\}, \{a_p^\dagger a_q^\dagger a_s a_r\}, \{a_p^\dagger a_q^\dagger a_s a_r\}, \cdots \right\} . \tag{3.5}$$

The discussion in Section 1.3.8 then tells us how to represent the relevant operators for the IMSRG in the basis $\mathcal{B}$.

We still must introduce truncations to the operator expressions, since each integration step in the IMSRG flow equations will technically induce new normal ordered operators of higher-body rank. We usually close the flow equations by truncating all operators consistently at a given operator level k, including the initial normal ordered Hamiltonian and observables of interest. This defines the so-called NOkB approximations.

Empirical evidence suggests that in the case of low–momentum interactions, neglecting the normal–ordered three-body component of the Hamiltonian results in a deviation of only 1-2% in the energies of the ground and absolute excited states of light and medium–mass nuclei [7, 29, 31, 85, 86]. This *NO2B approximation* will serve as our primary workhorse in the following. It offers an efficient approach to incorporate the effects of $3N$ forces in nuclear many–body calculations without incurring the computational expense of explicitly considering three-body operators.

3.2 In-Medium SRG Flow Equations

3.2.1 The IMSRG(2) Scheme

As discussed in Section 3.1, we close the IMSRG flow equations by truncating all induced operators above a given rank k, consistent with the NOkB approximation for representing the initial Hamiltonian. In the IMSRG context, this defines the *IMSRG(k) truncation scheme*.

Because of the empirical success of NO2B approximation for low-momentum NN+$3N$ Hamiltonians, where the omission of normal–ordered $3N$ term in exact calculations causes only small deviations of about 1–2% in ground-state energies of in oxygen, calcium, and nickel isotopes [6, 7, 85], we adopt $k = 2$.

Let's assume, then, that for each flow parameter s

$$\eta(s) \approx \eta^{[1]}(s) + \eta^{[2]}(s) \tag{3.6}$$

$$H(s) \approx E(s) + f(s) + \Gamma(s) \tag{3.7}$$

$$\frac{d}{ds}H(s) \approx \frac{d}{ds}E(s) + \frac{d}{ds}f(s) + \frac{d}{ds}\Gamma(s) \tag{3.8}$$

This is the so–called *IMSRG(2) truncation*, the foundation of all the results presented in the remaining part of this dissertation. It is similar to Coupled Cluster with Singles and Doubles (CCSD) [30, 63, 88] and the ADC(3) methods used in Self–Consistent Green's Function Theory [4, 89] to describe the same level of many–body correlations. Therefore, we anticipate similar convergence properties and results for observables obtained with the three techniques.

By inserting Eq. (3.6) – (3.8) into the operator flow equation (2.6) and calculating commutators from Section 1.3.7, we obtain

$$\frac{dE}{ds} = \sum_{ab}(n_p - n_q)\eta_{pq}f_{qp} + \frac{1}{2}\sum_{pqrs}\eta_{pqrs}\Gamma_{rspq}n_p n_q \bar{n}_r \bar{n}_s \tag{3.9}$$

$$\frac{df_{pq}}{ds} = \sum_{r}(1 + P_{pq})\eta_{pr}f_{rq} + \sum_{rs}(n_r - n_s)(\eta_{rs}\Gamma_{sprq} - f_{rs}\eta_{sprq}) \tag{3.10}$$

$$+ \frac{1}{2}\sum_{rst}(n_r n_s \bar{n}_t + \bar{n}_r \bar{n}_s n_t)(1 + P_{pq})\eta_{tprs}\Gamma_{rstq} \tag{3.11}$$

$$\frac{d\Gamma_{pqrs}}{ds} = \sum_t \{(1-P_{pq})(\eta_{pt}\Gamma_{tqrs} - f_{pt}\eta_{tqrs}) - (1-P_{rs})(\eta_{tr}\Gamma_{pqts} - f_{tr}\eta_{pqts})\} \tag{3.12}$$

$$+ \frac{1}{2}\sum_{tu}(1-n_t-n_u)(\eta_{pqtu}\Gamma_{turs} - \Gamma_{pqtu}\eta_{turs}) \tag{3.13}$$

$$+ \sum_{tu}(n_t-n_u)(1-P_{pq})(1-P_{rs})\eta_{tpur}\Gamma_{uqts} \tag{3.14}$$

where we have suppressed the s–dependence has been suppressed for brevity and introduced the permutation symbol P_{ij} to interchange the indices in any expression

$$P_{ij}g(\cdots,i,\cdots,j) \equiv g(\cdots,j,\cdots,i)\,. \tag{3.15}$$

As in chapter 1, $n_a \in \{0,1\}$ designates the particle occupation number and we introduce $\bar{n}_a = 1 - n_a$ the hole occupation number for convenience. Since the reference state is fixed, they do not change during the evolution. In Eqs. (3.9)–(3.14), we note that the occupation number factors effectively restrict the summations to particular combinations of particle and/or hole indices. The terms on the RHS of the energy flow equation (3.9), for example, are restricted to one-body matrix elements between particle and hole (ph) states, and two-body matrix elements with a $pphh$ structure.

To calculate nuclear ground–state energies, we integrate equations (3.9-3.14) from $s = 0$ to $s \to \infty$. We begin with the initial components of a normal–ordered Hamiltonian in NO2B, which are given by equations (1.88). By integrating the flow equations, we incorporate many–body correlations directly into the normal–ordered Hamiltonian. Looking at Eq. (3.9) again and noting that η is constructed from H, we notice a similarity to second-order energy corrections, except that here they would be evaluate for the flowing Hamiltonian $H(s)$. Similarly, the RHSs of Eqs. (3.11) and (3.14) have the structure of many-body corrections

to f and Γ, but since $H(s)$ rather than $H(0)$ are inserted in these expressions, the IMSRG evolution constructs highly nested versions of these corrections — from a Many-Body perturbation Theory perspective, certain classes of terms are included to *all* orders, which is why the IMSRG is a non-perturbative method [39].

3.2.2 Computational Scaling

The computational scaling of the IMSRG(2) scheme is dominated by the two–body flow equation, which naively requires $O(N^6)$ operations, putting it in the same category as CCSD and ADC(3). However, matrix products can be used to express large portions of the flow equations, allowing for the use of optimized linear algebra libraries. To further reduce computational cost, particle and hole states can be distinguished, as N_h, the number of hole states, is typically much smaller than N_p, the number of particle states. The best scaling achievable in IMSRG(2) depends on the choice of generator η: If the one– and two–body parts only consist of ph and $pphh$ type matrix elements and their Hermitian conjugates, the scaling is reduced to $O(N_h^2 N_p^4)$, matching the cost of solving CCSD amplitude equations. We will come back to this discussion in later parts of this dissertation.

3.3 Decoupling

After establishing the IMSRG flow equations, it is necessary to determine the decoupling approach, which involves separating the Hamiltonian into diagonal components to be preserved and off–diagonal components to be suppressed, as described in Sections 2.2 and 2.3. To accomplish this, we utilize the matrix representation of the Hamiltonian in an A-body Slater determinant basis (see Section 1.3.9). It should be noted that the Hamiltonian ma-

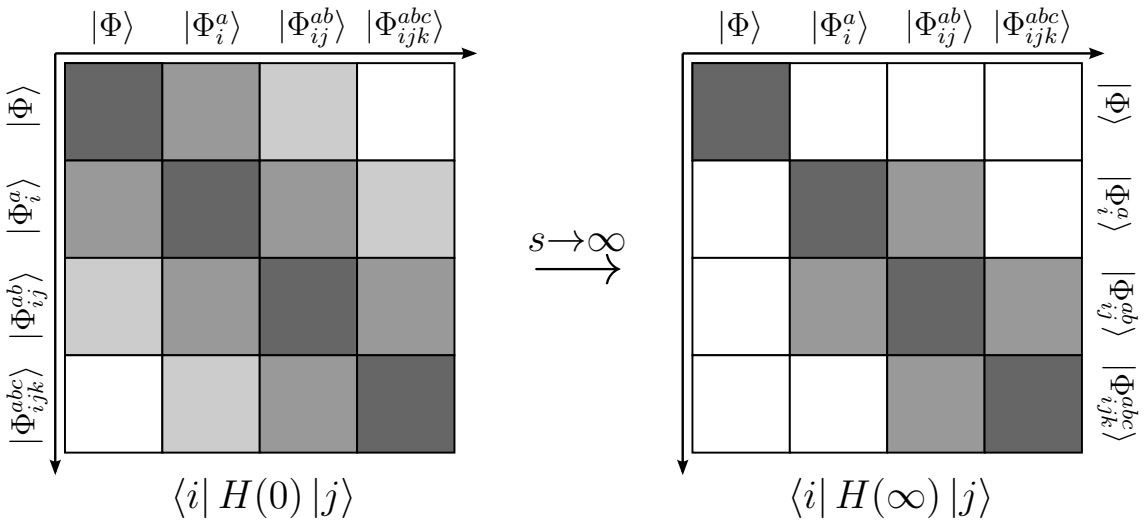

Figure 3.1: Schematic view of IMSRG decoupling in the many-body Hilbert space spanned by a Slater determinant reference $|\Phi\rangle$ and its particle-hole excitations $|\Phi_{i\ldots}^{a\cdots}\rangle$.

trix is not actually constructed in this representation, because its size is prohibitive. Our Slater determinant basis comprises the reference determinant $|\Phi\rangle$ and all of its particle-hole excitations, as discussed in Sections 1.3.6 and 1.3.9:

$$|\Phi\rangle\,, \{a_a^\dagger a_i\}\,|\Phi\rangle\,, \{a_a^\dagger a_b^\dagger a_j a_i\}\,|\Phi\rangle\,, \cdots \tag{3.16}$$

By utilizing Wick's theorem, it can be demonstrated that the particle–hole excited Slater determinants are orthogonal to the reference state and each other (see Sections 1.3.6–1.3.9). In the Hilbert space spanned by this basis, the initial Hamiltonian (in NO2B approximation) has the structure illustrated in the left panel of Figure 3.1. Its matrix representation has a band–diagonal form and can potentially couple excitations involving $npnh$ and $(n \pm 2)p(n \pm 2)h$.

In order to proceed, we must decompose the Hamiltonian into suitable diagonal and off–diagonal parts on the operator level, as outlined in references [55–57]. A broad interpretation of diagonality is not recommended, as it may result in strong in–medium $3N, \cdots$ interactions,

which can violate the truncation of the IMSRG(2). To avoid this, we employ a minimal decoupling scheme that exclusively aims to decouple the one–dimensional block consisting of the reference state from all particle–hole excitations. The right panel of Figure 3.1 provides an illustration of the descired outcome of the evolution.

In the ideal case, if we could implement the minimal decoupling scheme without any approximations, we would extract a single eigenvalue and eigenstate of the many–body Hamiltonian for the nucleus of interest in the limit as $s \to \infty$. The eigenvalue would be equivalent to the zero–body piece of $H(\infty)$, or simply $E(\infty)$, while the eigenstate could be obtained by applying the unitary IMSRG transformation to the reference state, $U^\dagger(\infty)\,|\Phi\rangle$. However, in practice, truncations are inevitable, and we can only obtain an approximate eigenvalue and mapping. It should be noted that the choice of reference state plays a crucial role in determining which eigenvalue and eigenstate of the Hamiltonian can be extracted using our minimal decoupling scheme. An empirical guideline is that the IMSRG flow will connect the reference state to the eigenstate that has the largest overlap with it. In general, if we aim to obtain the exact ground state, a Hartree-Fock Slater determinant is typically the best choice, as it minimizes both the absolute energy and the correlation energy.

By utilizing Wick's theorem to analyze the matrix elements between the reference state and its excitations, we can observe that the Hamiltonian couples the $0p0h$ block to $1p1h$ excitations block through specific matrix elements and their Hermitian conjugates:

$$\begin{aligned}
\langle\Phi|\, H\{a_a^\dagger a_i\}\,|\Phi\rangle &= E\,\langle\Phi|\,\{a_a^\dagger a_i\}\,|\Phi\rangle + \sum_{pq} f_{pq}\,\langle\Phi|\,\{a_p^\dagger a_q\}\{a_a^\dagger a_i\}\,|\Phi\rangle \\
&\quad + \frac{1}{4}\sum_{pqrs}\Gamma_{pqrs}\,\langle\Phi|\,\{a_p^\dagger a_q^\dagger a_s a_r\}\{a_a^\dagger a_i\}\,|\Phi\rangle \\
&= \sum_{pq} f_{pq}\delta_{pi}\delta_{aq} n_p \bar{n}_q
\end{aligned}$$

$$= f_{ia} \tag{3.17}$$

where the contributions arising from the zero–body and two–body components of the Hamiltonian vanish since they represent the expectation values of normal-ordered operators in the reference state — in the latter case, because we cannot fully contract a one- and a two-body operator (cf. Section 1.3.7). Similarly, the $0p0h$ and $2p2h$ blocks are coupled through certain matrix elements and their conjugates:

$$\langle \Phi | H \{ a_a^\dagger a_b^\dagger a_j a_i \} | \Phi \rangle = \Gamma_{ijab} \tag{3.18}$$

The matrix elements of the two–body Hamiltonian are responsible for coupling $npnh$ and $(n \pm 2)p(n \pm 2)h$ states, which includes not only the coupling between $|\Phi\rangle$ and excitations, but the entire outermost side diagonals of the Hamiltonian matrix. This observation implies that we can manipulate the Hamiltonian to take the form depicted in the top right panel of Figure 3.1 by defining its offdiagonal part as

$$H_{od} \equiv \sum_{ai} f_{ai} \{ a_a^\dagger a_i \} + \frac{1}{4} \sum_{abij} \Gamma_{abij} \{ a_a^\dagger a_b^\dagger a_j a_i \} + \text{H.c.} \tag{3.19}$$

In the following section, we will demonstrate that the IMSRG flow exponentially reduces the matrix elements of H_{od} and successfully accomplishes the desired decoupling in the limit $s \to \infty$.

3.4 Generators and Decay scales

Several commonly used generators for the single-reference scenario have the ansatz [37, 41]

$$\eta = \sum_{ai} \eta_{ai} \{a_a^\dagger a_i\} + \frac{1}{4} \sum_{abij} \eta_{abij} \{a_a^\dagger a_b^\dagger a_j a_i\} - \text{H.c.} \tag{3.20}$$

where H.c. denotes the Hermitian conjugate. The matrix elements of the generator are often either directly proportional to those of the off-diagonal Hamiltonian we introduced above, or simple functions of those matrix elements.

The most commonly used IMSRG generators are:

1. The *White generator*, named after S.R. White whose work [106] motivated this ansatz:

$$\eta_{ai} = \frac{f_{ai}}{\Delta_{ai}}, \qquad \eta_{abij} = \frac{f_{abij}}{\Delta_{abij}}, \tag{3.21}$$

   where the quantities

$$\Delta_{ai} = \langle \Phi_i^a | H | \Phi_i^a \rangle - \langle \Phi | H | \Phi \rangle = f_a - f_i - \Gamma_{aiai}, \tag{3.22}$$

$$\begin{aligned} \Delta_{abij} &= \langle \Phi_i^{ab} j | H | \Phi_i^{ab} j \rangle - \langle \Phi | H | \Phi \rangle \\ &= f_a + f_b - f_i - f_j + \Gamma_{abab} + \Gamma_{ijij} - \Gamma_{aiai} - \Gamma_{ajaj} - \Gamma_{bibi} - \Gamma_{bjbj}. \end{aligned} \tag{3.23}$$

   are the differences of the Hamiltonian's diagonal matrix elements for $1p1h$ or $2p2h$ states and the diagonal element for the reference state $|\Phi\rangle$. They play the role of the energy differences that govern the decay scales for the matrix elements of f and Γ, analogous to the free-space SRG discussion in Section 2.2.

2. The *White-ArcTan generator*, also motivated by [106]. Since the matrix elements of

the White generator diverge when the energy differences (3.22) and/or (3.23) vanish, causing the IMSRG flow to stall, it can be useful to work with a "regularized" form of the White generator instead, which is given by

$$\eta_{ai} = \frac{1}{2} \sum_{ai} \arctan \frac{2 f_{ai}}{\Delta_{ai}} , \qquad \eta_{abij} = \frac{1}{2} \sum_{abij} \arctan \frac{2 \Gamma_{abij}}{\Delta_{abij}} . \tag{3.24}$$

Note that for vanishing energy differenes, the matrix elements approach $\frac{\pi}{4}$.

3. The *imaginary time generator* [37, 39, 70], which is inspired by imaginary-time evolution techniques that are frequently used in Quantum Monte Carlo methods. It is defined by

$$\eta_{ai} = \mathrm{sgn}(\Delta_{ai})\, f_{ai} , \qquad \eta_{abij} = \mathrm{sgn}\big(\Delta_{abij}\big)\, f_{abij} . \tag{3.25}$$

4. Finally, the *Wegner generator*, which is given as usual by

$$\eta = \{H_d, H_{od}\} \tag{3.26}$$

with H_{od} defined in Eq. (3.19), and $H_d \equiv H - H_{od}$. Its one- and two-body parts have a similar structure as the IMSRG(2) flow equations (3.11) and (3.14), so we do not include it here, but refer to [37, 39, 41] for the full details. We note that this generator does not reduce to the form (3.20) in general — the Wegner generator can have additional nonzero matrix elements.

One can perform a perturbative analysis along the lines of our discussion in Section 2.2 to determine the asymptotic decay scales for the off-diagonal Hamiltonian's matrix elements

that result from each of the generators [39, 41]. It turns out that

$$\Gamma_{abij}(s) \approx \Gamma_{abij}(0) \exp\left(-|\Delta_{abij}|^n \, s\right) , \tag{3.27}$$

where $n = 0$ for the White generator, $n = 1$ for the imaginary-time generator, and $n = 2$ for the Wegner generator. Note that this implies that s has different units in each case.

3.5 Magnus Formulation of IMSRG

While the computational scaling of the IMSRG(2) approach is modest and comparable to other state-of-the-art many-body methods, we still may need a large number of integration steps to achieve "convergence" to the asymptotic limit of the flow for $s \gg \infty$. It is also necessary to use high-order ODE solvers like fourth-fifth order Runge-Kutta (RK45) when integrating the IMSRG flow equations (3.9)–(3.14) in order to avoid an accumulation of integration-step errors, and such solvers require multiple copies of the solution vector, which in our cases can consist of hundred of millions of evolving matrix elements $f_{pq}(s), \Gamma_{pqrs}(s)$. This is a substantial computational bottleneck of the technique (refer to, for instance, [14, 42, 43]).

Moreover, to calculate the expectation values of observables O in addition to the Hamiltonian, we would in principle need to consistently evolve general operators using the flow equation

$$\frac{dO}{ds} = [\eta, O] , \tag{3.28}$$

with the same generator $\eta[H(s)]$ as in Eq. (2.6). Since storing the generators at every point in the flow trajectory is simply too expensive, we are forced to solve the equation

(5.5) simultaneously with the flow equation for the Hamiltonian. This not only increases the dimension of the ODE system, but may cause additional stiffness, especially if the operators evolve at different characteristic scales than the Hamiltonian.

These limitations can be overcome by applying *Magnus expansion* methods [8, 68, 70] to the the differential equation for the unitary transformation itself,

$$\frac{dU(s)}{ds} = -\eta(s)U(s)\,. \tag{3.29}$$

Mathematically, the solution to this ODE is given by the *s- or path-ordered exponential*:

$$U(s) = \mathcal{S}\exp\int_0^s ds'\eta(s') \tag{3.30}$$

$$\equiv \sum_n \frac{1}{n!}\int_0^s ds_1 \int_0^s ds_2 \cdots \int_0^s ds_n \mathcal{S}\{\eta(s_1)\cdots\eta(s_n)\} \tag{3.31}$$

Due to the dynamical changes that occur in the generator during the evolution, the expression should be merely understood as a short-hand for the Dyson series (3.31). The s–ordering operator $\mathcal{S}$ guarantees that the integrands in question always feature the flow parameters in a descending order, whereby $s_1 > s_2 > \cdots$. However, this form of the solution is of limited practical value in calculations due to several reasons. First, it lacks specific instructions on how the series should be truncated. Second, we would again need to store η for multiple s–values to evaluate it. Finally, it is unclear how the Hamiltontian and other observables can be consistently transformed in a fully linked and size-extensive manner if we inevitably need to introduce truncations [70].

In 1954, Magnus proposed that under unspecified conditions the Dyson series can be

resummed into a proper exponential of an operator,

$$U(s) = e^{\Omega(s)} \tag{3.32}$$

where the Magnus operator $\Omega(s)^\dagger = -\Omega(s)$ is anti-Hermitian and satisfies $\Omega(0) = 0$, and he developed formal techniques for the [68]. The review paper [8] discusses some of the formal conditions for the existence of $\Omega(s)$ as well as the convergence of the series — however, these are difficult to check mathematically in our context. Assuming that the IMSRG transformation can be expressed as in Eq. (3.32), we can obtain a flow equation for $\Omega(s)$:

$$\frac{d\Omega(s)}{ds} = \sum_0^\infty \frac{B_k}{k!} \mathrm{ad}_\Omega^k(\eta) \tag{3.33}$$

where B_k are Bernoulli numbers, and

$$\mathrm{ad}_\Omega^k(\eta) = [\Omega, \mathrm{ad}_\Omega^{k-1}(\eta)], \qquad \mathrm{ad}_\Omega^0(\eta) = \eta\,. \tag{3.34}$$

Similary to the standard IMSRG(2), both η and Ω as well as any of the commutators in the nested series on the RHS of Eq. (3.33) are truncated at the two–body level. This leads to the development of a new computational approach, referred to as the Magnus(2) formulation of the IMSRG. The nested commutators generated by ad_Ω^k are evaluated recursively until satisfactory convergence of RHS of Eq. (3.33) is achieved [8, 18, 24]. At every integration step, the Baker–Campbell–Hausdorff (BCH) formula is utilized to construct the Hamiltonian and other observables,

$$H(s) = e^\Omega H(0) e^{-\Omega} = \sum_{k=0}^\infty \frac{1}{k!} \mathrm{ad}_{\Omega(s)}^k(H(0)) \tag{3.35}$$

$$O(s) = e^{\Omega} O(0) e^{-\Omega} = \sum_{k=0}^{\infty} \frac{1}{k!} \mathrm{ad}^{k}_{\Omega(s)}(O(0)) \tag{3.36}$$

The Magnus formulation offers a significant advantage in that the flow equations for $\Omega(s)$ can be solved using a straightforward first–order Euler step method without compromising accuracy. This leads to considerable memory savings and moderate reduction in CPU time. Although integration–step errors accumulate in $\Omega(s)$ with a first–order method, the transformation remains explicitly unitary upon exponentiation, and the transformed $H(s) = U(s)H(0)U^{\dagger}(s)$ is unitarily equivalent to the initial Hamiltonian, except for the truncations made during the evaluation of BCH formula [70].

Maybe even more importantly, we can store the final $\Omega(\infty)$, and use it to compute any observable of interest by simplify applying Eq. (3.36) at will.

Chapter 4

Factorization Techniques

In this chapter, we will provide an overview of various decomposition techniques. Decomposition methods are essential tools that allow us to represent large and complex matrices as a product of smaller, more manageable matrices, vectors, or tensors. These decomposition techniques provide powerful tools that we hope to use to reduce the computational complexity of the SRG and IMSRG, and can lead to more efficient and accurate simulations of quantum many-body systems. In the following sections, we will delve into each of these techniques in more detail.

4.1 Singular Value Decomposition

Consider an $m \times n$ matrix, A, with real entries, and let r be the smaller of the two dimensions. For any such matrix, a singular value decomposition (SVD) exists in the following form:

$$\underset{m\times n}{A} = \underset{m\times r}{U} \quad \underset{r\times r}{\Sigma} \quad \underset{r\times n}{V}^{\dagger 1} \tag{4.1}$$

where U and V are orthonormal matrices and Σ is a diagonal matrix. The columns $(u_j)_{j=1}^r$ and $(v_j)_{j=1}^r$ of U and V are the *left* and *right singular vectors* of A, respectively. The *singular values* of A are the diagonal entries $(\sigma_j)_{j=1}^r$, which we usually assume to be arranged in

[1] In mathematical formalism, $*$ is sometimes used to represent the conjugate transpose of a matrix.

descending order so that $\sigma_1 \geq \sigma_2 \geq \cdots \geq \sigma_r \geq 0$. To put it another way,

$$U = [u_1 u_2 \cdots u_r], \quad V = [v_1 v_2 \cdots v_r], \quad \Sigma = \mathrm{diag}(\sigma_1, \sigma_2, \cdots, \sigma_r) \tag{4.2}$$

The factorization (4.1) represents A as a sum of r rank-one matrices

$$A = \sum_{j=1}^{r} \sigma_j u_j v_j^\dagger , \tag{4.3}$$

and we are primarily interested in the cases where the singular values σ_j decay rapidly to zero, resulting in the swift convergence of the sum. In such instances, we can approximate $A_k \approx A$, where A_r is defined by the truncated sum

$$A_k = \sum_{j=1}^{k} \sigma_j u_j v_j^\dagger = U_k \Sigma_k V_k^\dagger \tag{4.4}$$

with $k \leq r$. It was proven by Eckart and Young [20] that the truncated SVD gives the optimal, i.e., most precise, rank-k approximation to a matrix A.

4.2 Randomized SVD

The classical algorithms for computing the SVD (4.1) can be computationally expensive for large matrices like the ones we work with in (nuclear) many-body theory since its asymptotic cost is $O(mnr)$, where again $r = \min(m, n)$. Naively, we would first need to calculate the full SVD before applying a truncation to get the optimal low-rank approximation. However, randomized sampling can significantly speed up the algorithms for obtaining the low-rank SVD factorization, with only minor losses in accuracy [32].

In essence, randomized factorization algorithms construct low-rank approximation of a matrix by applying the desired factorization to a smaller matrix derived from the original matrix with random projection techniques. In this section, we focus on constructing an approximate low-rank singular value decomposition using randomization. To obtain a sample of the column space of A, we compute $Y = A\Omega$, where Ω is an $n \times (k+p)$ Gaussian random matrix, k is the desired rank, and p a small oversampling parameter. We then obtain an orthonormal column matrix Q of size $m \times (k+p)$ by performing a QR factorization on Y. If Y captures a good portion of the range of A and assuming that k is large enough relative to the numerical rank of A, we can approximate A with $QQ^\dagger A$. We can then compute the factorization of the smaller $(k+p) \times n$ product matrix $Q^\dagger A$ and multiply the result by Q to obtain an approximation of A. The matrix product $P = QQ^\dagger$ is a projector onto the range of Q and hence onto that of Y, which is obtained via a compact QR factorization of Y. The equality of $QQ^\dagger A$ and A is achieved when Y captures the entire range of A.

Mathematically, if $\mathcal{R}(Q)$[2] $\approx \mathcal{R}(A)$, then $QQ^\dagger A \approx A$ [32]. We may prove this informally by splitting the SVD of A,

$$A = \begin{bmatrix} U_1 & U_2 \end{bmatrix} \begin{bmatrix} \Sigma_1 & 0 \\ 0 & \Sigma_2 \end{bmatrix} \begin{bmatrix} V_1^\dagger \\ V_2^\dagger \end{bmatrix} \tag{4.5}$$

where the left singular matrix U is split into two parts U_1 of size $m \times k$ and U_2 of size $m \times (r-k)$, the singular value matrix Σ into two diagonal matrices Σ_1 and Σ_2 with size $k \times k$ and $(r-k) \times (r-k)$, respectively, and the transpose of the right singular matrix $V^\dagger$ into $V_1^\dagger$ of size $k \times n$ and $V_2^\dagger$ of size $(r-k) \times n$. Now suppose we take a Gaussian independent

[2] $\mathcal{R}$ designates the range, or column space, of a matrix.

identically distributed matrix Ω of size $n \times (k+p)$

$$\begin{aligned} Y = A\Omega &= \begin{bmatrix} U_1 & U_2 \end{bmatrix} \begin{bmatrix} \Sigma_1 & 0 \\ 0 & \Sigma_2 \end{bmatrix} \begin{bmatrix} V_1^\dagger \\ V_2^\dagger \end{bmatrix} \Omega \\ &= \begin{bmatrix} U_1 & U_2 \end{bmatrix} \begin{bmatrix} \Sigma_1 & 0 \\ 0 & \Sigma_2 \end{bmatrix} \begin{bmatrix} V_1^\dagger \Omega \\ V_2^\dagger \Omega \end{bmatrix} \\ &= \begin{bmatrix} U_1 & U_2 \end{bmatrix} \begin{bmatrix} \Sigma_1 \Omega_1 \\ \Sigma_2 \Omega_1 \end{bmatrix} \end{aligned} \tag{4.6}$$

where we define $\Omega_1 \equiv V_1^\dagger \Omega$ and $\Omega_2 \equiv V_2^\dagger \Omega$ of size $k \times (k+p)$ and $(r-k) \times (k+p)$ respectively. Since $\mathcal{R}(Q) = \mathcal{R}(Y)$[3], the projector onto the range of Y is equivalent to that of Q. Thus, we have $P_Y = QQ^\dagger$ and the error of A and A_r is

$$A - QQ^\dagger A = A - P_Y A = (1 - P_Y)A \tag{4.7}$$

In [32], it is demonstrated that if the matrix Ω_1 has a full row rank, then the error of this approximation can be bounded by

$$\|(I - P_Y)A\| \leq \|\Sigma_2\|^2 + \left\|\Sigma_2 \Omega_2 \Omega_1^\dagger\right\|^2 \tag{4.8}$$

where $\|\cdot\|$ is either the spectral or Frobenius norm. Obviously, if A has exactly rank k, then $\Sigma_2 = 0$, causing the right hand side of the equation to be 0. Consequently, $QQ^\dagger A = A$, and Y will cover the range of A. As k gets closer to the rank of A, Y will cover more of $\mathcal{R}(A)$, and the product $QQ^\dagger A$ will converge to A. Therefore, if we can find an orthonormal matrix

[3] This is a result of the orthogonal matrix Q being obtained via a compact QR factorization of Y.

Q such that

$$\left\|(I - QQ^\dagger)A\right\| \leq \epsilon\,, \tag{4.9}$$

we can factorize $Q^\dagger A$ of size $(k+p)\times n$ and multiply the result by Q to obtain an approximate factorization of A with the same approximation error as stated in (4.8) or in (4.9). If k is much smaller than $\min(m,n)$, then $Q^\dagger A$ is considerably smaller than A. We can then compute the SVD of full rank $k+p$ of $Q^\dagger A$ and multiply the result by Q to obtain an approximate SVD of A.

$$\begin{aligned} A \approx Q(Q^\dagger A) &= Q(\tilde{U}DV^\dagger) \\ &= (Q\tilde{U})DV^\dagger \end{aligned} \tag{4.10}$$

where D is the truncated singular value matrix of $Q^\dagger A$, and thus of A, and $Q\tilde{U}$ is the left singular value matrix of A.

4.3 Power Iteration

We now introduce a power iteration method that enhances the accuracy of the low-rank approximation for matrices with large and slowly decaying singular values.

To implement this method, instead of forming the matrix $A\Omega$, we construct a matrix $Y = ((AA^\dagger)^q A)\Omega$, where q is an integer power greater than or equal to 1. We then obtain the orthogonal matrix Q from Y. It is important to note that both A and $(AA^\dagger)^q A$ share the same eigenvectors and corresponding eigenvalues. By substituting the SVD $A = U\Sigma V^\dagger$, we see that

$$(AA^\dagger)^q A = (U\Sigma^2 U^\dagger)^q A = U\Sigma^{2q}U^\dagger U\Sigma V^\dagger = U\Sigma^{2q+1}V^\dagger\,. \tag{4.11}$$

For matrices A with slowly decaying singular values, $(AA^\dagger)^q A$ with $q \geq 1$, exhibits a noticeably accelerated decay rate for its own singular values.

4.4 Algorithms for Low-Rank Approximation via Randomized SVD

To compute a truncated, low–rank singular value decomposition of a matrix A of size $m \times n$, the basic randomized algorithm involves the following steps:

1. Generate a random matrix Ω of size $n \times l$ with $l = k + p$.

2. Form a sample matrix Y of size $m \times l$ by multiplying $Y = A\Omega$.

3. Apply power iteration if necessary.

4. Orthogonalize the sample matrix to obtain the matrix $Q = \mathrm{orth}(Y)$.

5. Project the original matrix A into a lower-dimensional matrix $B = Q^\dagger A$, where B is an $l \times n$ matrix significantly smaller than A.

6. Compute the SVD of the smaller matrix B as $B = \tilde{U}\Sigma V^\dagger$.

7. Form the matrix U by multiplying $U = Q\tilde{U}$.

8. Approximate the rank–k SVD of A by setting

$$U_r = U(:, 1:k), \qquad \Sigma_r = \Sigma(1:r, 1:k), \qquad V_r = V(:, 1:k),$$

so that $A \approx U_k \Sigma_k V_k^\dagger$.

Algorithm 1 RSVD Algorithm Version I

Input : $A \in \mathbb{R}^{m\times n}$, integer rank parameter $k < \min(m,n)$, an integer oversampling parameter $p > 0$, an integer power iteration parameter $q \geq 0$, and an integer re–orthogonalization amount parameter $s \geq 1$.
Output : Matrices $U_k \in \mathbb{R}^{m\times k}, \Sigma_k \in \mathbb{R}^{k\times k}$, and $V_k \in \mathbb{R}^{k\times n}$.

Set $l = k + p$ and initialize a matrix $R \in \mathbb{R}^{n\times l}$ with Gaussian random entries;
Form samples matrix $Y = AR$ and perform optional power iteration;
for $j = 1$ **to** q **do**
    if $\mathrm{mod}((2j-2), s) == 0$ **then**
        $[Y, \cdot] = \mathrm{qr}(Y, 0)$;
    end if
    $Z = A^{\dagger}Y$;
    if $\mathrm{mod}((2j-1), s) == 0$ **then**
        $[Z, \cdot] = \mathrm{qr}(Z, 0)$;
    end if
    $Y = AZ$
end for
Orthonormalize the columns of Y in $[Q, \cdot] = \mathrm{qr}(Y, 0)$;
Construct the smaller matrix $B = Q^{\dagger}A$ derived from A;
Form the even smaller $l \times l$ matrix $T = BB^{\dagger}$;
Perform eigendecomposition of $l \times l$ matrix $[U, D] = \mathrm{eig}(T)$;
Form the approximate low-rank SVD components of A using the results of the eigendecomposition $\Sigma_k = \sqrt{D}, U_k = QU, V_k = B^{\dagger}U\Sigma_k^{-1}$;
Extract components corresponding to the k largest by magnitude singular values $U_k = U_k(:, (p+1) : l)$; $\Sigma_k = \Sigma_k((p+1) : l, (p+1) : l)$; $V_k = V_k(:, (p+1) : l)$;

Next, we present alternative randomized algorithms for approximating low–rank SVD adapted from [97].

Algorithm 1 introduces a modification that obviates the necessity to perform the SVD computation on the substantial $l \times n$ matrix B. This size can persist when the number of columns within matrix A is extensive. Instead, the algorithm leverages the eigendecomposition of the more compact $k \times k$ matrix $BB^{\dagger}$. In contrast, Algorithm 2 takes a diffrent approach by employing the QR factorization of $B^{\dagger}$ to generate a reduced matrix R, which is then used for the subsequent SVD calculation.

It's important to highlight that even the downscaled matrix B, which corresponds to the

Algorithm 2 RSVD Algorithm Version II

Input : $A \in \mathbb{R}^{m\times n}$, integer rank parameter $k < \min(m,n)$, an integer oversampling parameter $p > 0$, an integer power sampling parameter $q \geq 0$, and an integer re–orthogonalization amount parameter $s \geq 1$.
Output : Matrices $U_k \in \mathbb{R}^{m\times k}, \Sigma_k \in \mathbb{R}^{k\times k}$, and $V_k \in \mathbb{R}^{k\times n}$.

Set $l = k + p$ and initialize a matrix $R \in \mathbb{R}^{n\times l}$ with Gaussian random entries;
Form samples matrix $Y = AR$ and utilize optional power scheme;
for $j = 1$ **to** q **do**
    if $\mathrm{mod}((2j-2), s) == 0$ **then**
        $[Y, \cdot] = \mathrm{qr}(Y, 0)$;
    end if
    $Z = A^{\dagger}Y$;
    if $\mathrm{mod}((2j-1), s) == 0$ **then**
        $[Z, \cdot] = \mathrm{qr}(Z, 0)$;
    end if
    $Y = AZ$
end for
Orthonormalize the columns of Y in $[Q, \cdot] = \mathrm{qr}(Y, 0)$;
Compute the smaller matrix $Bt = A^{\dagger}Q$;
Obtain the small $l \times l$ matrix R using a compact QR factorization $[Q, R] = \mathrm{qr}(Bt, 0)$;
Take the SVD of the $l \times l$ matrix R, $[U, \Sigma_k, V] = \mathrm{svd}(R)$;
Form the approximate low rank SVD components of A using the results of the SVD of R. $U_k = QV$, $V_k = QU$;
Extract component corresponding to the k largest by magnitude singular values $U_k = U_k(:, 1:k) \quad \Sigma_k = \Sigma_k(1:k, 1:k); \quad V_k = V_k(:, 1:k)$;

larger matrix A, might still pose challenges for multiplication due to its size. In scenarios where this hold true, a customized adaptation of Algorithm 1 prove useful. This involves assessing the matrix-matrix product $BB^{\dagger}$ column-wise, utilizing standard basis vectors like $BB^{\dagger}e_j$, particularly when matrix B becomes excessively large. This methodology can also be extended to the computation of V_k through the application of the matrix-matrix product $B^{\dagger}U\Sigma^{-1}$.

Part II

Factorization in Few-Body Systems

Chapter 5

SVD-SRG evolution in Two-Nucleon Interactions

Ab initio nuclear many–body theory faces challenges in the coming decade due to the increase in computational and storage costs required for calculations of heavy, neutron-rich, and structurally complex nuclei. This chapter[1] explores the factorization of nuclear interactions as a first step towards solving this issue. SVDs of nucleon–nucleon interactions are performed in partial wave representation, and the dependence of the singular value spectrum on interaction characteristics is studied. Next, an SRG evolution is developed and implemented directly in terms of the relevant singular vectors. Results show that low–resolution interactions allow for the truncation of the SVD at low rank, and a small number of relevant components are sufficient to capture the nuclear interaction and perform an accurate SRG evolution. Importantly, the rank is uniform across all partial waves and almost independent of the basis choice. This chapter also discusses strategies for mitigating the growth of the rank that is caused by the subsequent transformation of the interaction between the center–of–mass and laboratory frames. The low rank approximation to the SRG–evolved interactions is tested in many–body calculations using the in–medium SRG, and the implementation of the SRG using the singular vectors of the interaction is shown

[1] This chapter is adapted from my publication [112].

to not affect the evolution of other observables, which is verified by analyzing nuclear mean-square radii.

5.1 Free-Space SRG

Throughout this chapter, we will be studying SRG evolutions in a momentum-space partial-wave representation, as introduced in chapter 2. We will use the standard generator for performing momentum decoupling (also see [10, 35, 95])

$$\eta(s) = [T, H(s)] \tag{5.1}$$

where T is the relative (or intrinsic) kinetic energy — we drop the label for the sake of brevity. We keep the kinetic energy constant during the flow, hence all s-dependent contributions from evolving T are absorbed into the interaction $V(s)$:

$$H(s) = T + \delta T(s) + \bar{V}(s) \equiv T + V(s) \tag{5.2}$$

with

$$\delta T(0) = 0, \qquad \bar{V}(0) = V(0) \tag{5.3}$$

This partitioning will be important later. Substituting Eq. (5.1) and Eq. (5.2) into Eq. (2.6) and setting $\frac{dT}{ds} = 0$ yields the following equation for $V(s)$ (cf. Eq. (2.24)):

$$\begin{aligned} \frac{d}{ds}V(s) &= [\eta(s), T] + [\eta(s), V(s)] \\ &= [[T, V(s)], T] + [[T, V(s)], V(s)] \,. \end{aligned} \tag{5.4}$$

This evolution can be conveniently implemented in momentum space, where T will be represented by a diagonal matrix.

As discussed in previous chapters, general observables can in principle be calculated by co-evolving them with the Hamiltonian according to

$$\frac{d}{ds}O(s) = [\eta(s), O(s)] \,, \tag{5.5}$$

but each additional observable increases the size of the ODE system by the full dimension of the momentum basis and may affect its overall stiffness. Because we are dealing with matrix-based SRG evolutions here, several methods exist to address this issue. One such method is to obtain the eigenvalue solutions of the initial and final Hamiltonian matrices and construct $U(s)$ in Eq. (2.1) directly as [2, 26, 87].

$$U(s) = \sum_n |\psi_n(s)\rangle \langle \psi_n(0)| \,. \tag{5.6}$$

Another way to obtain $U(s)$ is by directly solving the ODE

$$\frac{d}{ds}U(s) = \eta(s)U(s), \qquad U(s=0) = \mathbb{I}\,, \tag{5.7}$$

and a third option is to employ the Magnus expansion (see Section 3.5), but this approach was found to be susceptible to convergence problems [95].

5.2 SRG evolution of SVD factors

Let us assume that we have successfully performed an SVD decomposition of the initial Hamiltonian $H(0)$,

$$H(0) = \sum_i |u_i(0)\rangle \, \sigma_i \, \langle v_i(0)| \, , \tag{5.8}$$

and consider its SRG evolution. The evolved Hamiltonian can be written as

$$\begin{aligned} H(s) &= \sum_i U(s) \, |u_i(0)\rangle \, \sigma_i \, \langle v_i(0)| \, U^\dagger(s) \\ &\equiv \sum_i |u_i(s)\rangle \, \sigma_i \, \langle v_i(s)| \, , \end{aligned} \tag{5.9}$$

where we have used the invariance of singular values under unitary transformations and defined evolved singular vectors as $|u_i(s)\rangle$ and $|v_i(s)\rangle$. Inserting Eq. (5.9) into the flow equation (2.6),

$$\begin{aligned} \sum_i \frac{d}{ds}\Big(|u_i(s)\rangle \, \sigma_i \, \langle v_i(s)|\Big) &= [\eta(s), H(s)] \\ &= \sum_i \left(\eta(s) \, |u_i(s)\rangle \, \sigma_i \, \langle v_i(s)| - |u_i(s)\rangle \, \sigma_i \, \langle v_i(s)| \, \eta(s)\right) . \end{aligned} \tag{5.10}$$

The LHS of this equation can be rewritten using

$$\frac{d}{ds}\Big(|u_i(s)\rangle \, \sigma_i \, \langle v_i(s)|\Big) = \left(\frac{d}{ds} \, |u_i(s)\rangle\right) \sigma_i \, \langle v_i(s)| + |u_i(s)\rangle \, \sigma_i \left(\frac{d}{ds} \, \langle v_i(s)|\right) . \tag{5.11}$$

By comparing Eq. (5.10) and Eq. (5.11), we can then easily derive flow equations for the singular vectors:

$$\frac{d}{ds} \, |u_i(s)\rangle = \eta(s) \, |u_i(s)\rangle \, , \tag{5.12a}$$

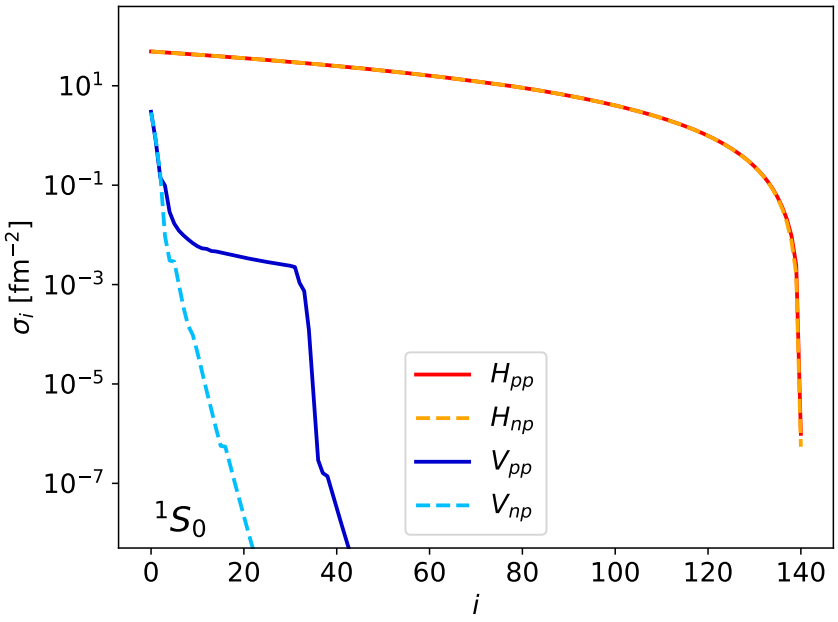

Figure 5.1: Singular value spectra of H and V in the proton–proton (solid curves) and neutron–proton $^1S_0$ partial waves (dashed curves), for a chiral N^{3}LO two–nucleon interaction (EM, cutoff $\Lambda = 500$ MeV/c, see text and Ref. [22]). The units of the singular vectors result from adopting scattering units $\hbar c/mc^2 = 1$ as well as momentum–space discretization discussed in Sec. 2.3.

$$\frac{d}{ds}\,|v_i(s)\rangle = \eta(s)\,|v_i(s)\rangle\ . \tag{5.12b}$$

When attempting to apply the SRG flow to the SVD of the Hamiltonian, a significant obstacle arises due to the unbounded nature of the kinetic energy term. This prevents us from identifying a natural low-rank truncation for the components of $H(0)$, as illustrated in Figure 5.1. Fortunately, Eq. (5.4) suggests that we should consider the SVD of the evolving part of the Hamiltonian anyway, which is $V(s)$ as defined above.

At $s = 0$, the SVD of the interaction is given by

$$V(0) = \sum_{ij} |u_i(0)\rangle\,\sigma_{ij}\,\langle v_j(0)|\,, \qquad \sigma_{ij} = \sigma_i\delta_{ij}\,. \tag{5.13}$$

As an example, Figure 5.1 also displays the singular value spectrum of the proton–proton (pp) and neutron-proton (np) $^1S_0$ partial waves of a realistic chiral N^{3}LO interaction [22]. This spectrum shows that the interaction possesses a low–rank structure. We note that the inclusion of the Coulomb interaction can increase the rank of the interaction in the pp channels, but not to an extent where truncations would be impractical. We also note that the singular values of the interaction decay exponentially, while the kinetic term in the Hamiltonian grows only quadratically. As a result, the singular value spectrum of the generator (5.1) will also decay exponentially. Therefore, the SRG evolution via Eq. (5.4) will not alter the low–rank structure of the interaction, except for potential truncation artifacts.

For $s > 0$, we have

$$V(s) = \sum_{ij} |u_i(s)\rangle \left(\sigma_{ij} + \delta\sigma_{ij}(s)\right) \langle v_j(s)| \tag{5.14}$$

where the set of singular values pertaining to the initial interaction is invariant during unitary evolution but a $\delta\sigma_{ij}(s)$ arises from the incorporation of induced contributions from the evolution of the kinetic energy. By examining the expressions on both sides of Eq. (5.4), we can formulate a flow equation for $\delta\sigma_{ij}(s)$. Substituting Eq. (5.14) into the equation, we obtain

$$\frac{d}{ds}V(s) = [\eta(s), V(s)] + \sum_{ij} |u_i(s)\rangle \left(\frac{d}{ds}\delta\sigma_{ij}(s)\right) \langle v_j(s)| \tag{5.15}$$

Using the orthogonality of the singular vectors, we obtain

$$\frac{d}{ds}\delta\sigma_{ij}(s) = \langle u_i(s)| [\eta(s), T] |v_j(s)\rangle \tag{5.16}$$

In principle, it is necessary to solve this flow equation alongside Eq. (5.12), but it turns out that it can be solved analytically. By expanding the right–hand side and substituting

Eq. (5.12) to convert to derivatives of the singular vectors, we can obtain a closed solution:

$$\begin{aligned}
\frac{d}{ds}\delta\sigma_{ij}(s) &= \langle u_i(s)|\,[\eta(s), T]\,|v_j(s)\rangle \\
&= \langle u_i(s)|\,(\eta(s)T - T\eta(s))\,|v_j(s)\rangle \\
&= \langle u_i(s)|\,\eta(s)T\,|v_j(s)\rangle - \langle u_i(s)|\,T\eta(s)\,|v_j(s)\rangle \\
&= -\langle u_i(s)|\,\eta^\dagger(s)T\,|v_j(s)\rangle - \langle u_i(s)|\,T\eta(s)\,|v_j(s)\rangle \\
&= -\left(\frac{d}{ds}\langle u_i(s)|\right)T\,|v_j(s)\rangle - \langle u_i(s)|\,T\left(\frac{d}{ds}|v_j(s)\rangle\right)
\end{aligned} \tag{5.17}$$

where we recognize that the last line is merely the derivative of $\langle u_i(s)|\,T\,|v_j(s)\rangle$. Integrating both sides, we obtain the closed solution

$$\delta\sigma_{ij}(s) = \langle u_i(0)|\,T\,|v_j(0)\rangle - \langle u_i(s)|\,T\,|v_j(s)\rangle\ , \tag{5.18}$$

i.e., it is necessary to calculate the matrix elements of the kinetic energy within the representation defined by the initial and final singular vectors. However, we can rewrite the first term in Eq. (5.18) as follows:

$$\begin{aligned}
\langle u_i(0)|\,T\,|v_i(0)\rangle &= \langle u_i(0)|\,U^\dagger(s)U(s)TU^\dagger(s)U(s)\,|v_i(0)\rangle \\
&= \langle u_i(s)|\,U(s)TU^\dagger(s)\,|v_i(s)\rangle \\
&= \langle u_i(s)|\,T + \delta T(s)\,|v_j(s)\rangle\ .
\end{aligned} \tag{5.19}$$

Plugging this back into Eq. (5.18), the contributions from T cancel and we see that

$$\delta\sigma_{ij}(s) = \langle u_i(s)|\,\delta T(s)\,|v_j(s)\rangle\ , \tag{5.20}$$

i.e., we only need to evaluate the s–dependent portion of the kinetic energy within the (truncated) basis of evolved singular vectors.

We remark that while the evolved SVD representation of $V(s)$ will have a non-diagonal singular value matrix $\sigma + \delta\sigma(s)$ in the end, we can readily diagonalize it to obtain a "final" set of singular vectors if we so desire, since its dimensions match the rank of the truncated SVD and are therefore small.

The construction SRG transformation $U(s)$ can be readily constructed from the initial and final singular vectors $|u_i(s)\rangle$ and $|v_i(s)\rangle$:

$$U^{(L)}(s) = \sum_i |u_i(s)\rangle \langle u_i(0)| \,, \tag{5.21a}$$

$$U^{(R)}(s) = \sum_i |v_i(s)\rangle \langle v_i(0)| \,. \tag{5.21b}$$

In principle, we need to differentiate between left and right unitary transformations, depending on whether we construct $U(s)$ from the $|u_i(s)\rangle$ or $|v_i(s)\rangle$. Since we are usually interested in the evolution of Hermitian operators, the difference between the left and right singular vectors is merely an irrelevant phase factor. By means of the $U(s)$ constructed from the singular vectors, it is feasible to transform any arbitrary observables O according to

$$O(s) = U(s)O(0)U^\dagger(s) \,. \tag{5.22}$$

5.3 Applications in the Two-Nucleon System

We are now ready to study the interplay of the SVD and SRG in the two-nucleon system. We will first perform SVDs of interactions that have been evolved using the SRG before

applying the SVD-based SRG formalism developed in the previous section.

5.3.1 Momentum Discretization and Conventions

Throughout this section, we will work with the discretized momentum-space partial-wave representation introduced in Section 2.3. In particular, we absorb the weights and q_i^2 factors from the integration measure into the interaction matrices (see Eq. (2.29)), so that they do not appear explicitly in Eq. (5.12). This has the added benefit that it simplifies the comparison of truncated SVDs among different mesh and basis choices, and it may facilitate the interpretation of the singular components as mere representations of particular basis operators for the interaction in the future. When comparing with the existing literature on the SRG transformation of matrix elements (e.g., [10, 35, 95]), we will simply revert back to the original basis.

Figure 5.2 presents our findings regarding the independence of the singular values on the selected mesh for the proton–proton (pp) and neutron–proton (np) partial waves of the NN interaction, using the chiral N^{3}LO interaction with $\Lambda = 500$ MeV/c by Entem and Machleidt as an example. We refer to this interaction as the EM interaction in the subsequent discussion. We found that the singular value spectra for two equidistant meshes with the same maximum momentum but different spacings are practically identical for $\sigma_i \geq 10^{-10}$ fm^{-2}.

The precision with which the input matrix elements are stored affects the singular value spectrum's extension. Specifically, reducing the number of decimal digits from 10 to 6 leads to an elongated tail of unphysical singular values of the order of $\sigma_i \approx 10^{-6}$ fm^{-2}. These contributions to the interaction would not be considered in practical applications anyway — based on the computed spectra, a natural threshold $\sigma_t \approx 10^{-3}$ fm^{-2} emerges that should

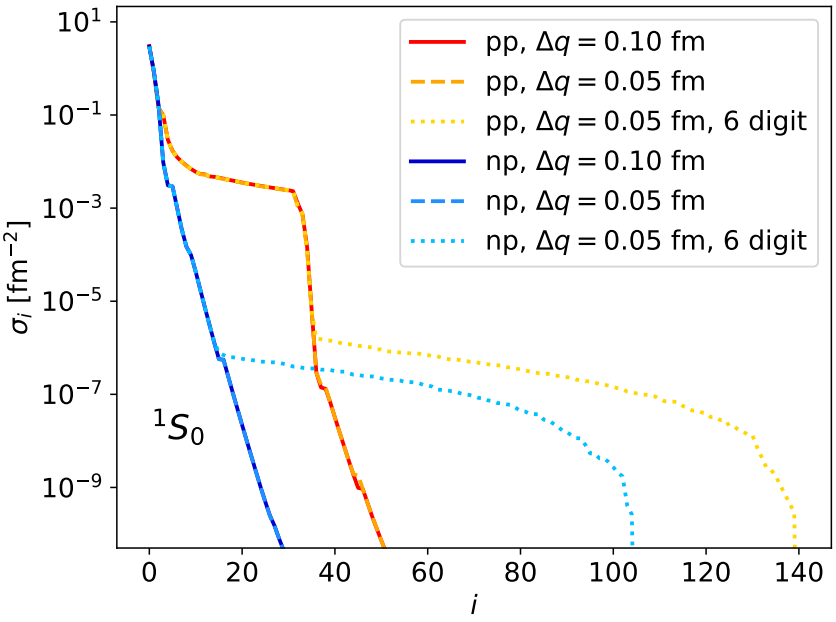

Figure 5.2: Singular value spectra of V in the proton-proton and neutron-proton $^1S_0$ partial waves, for the EM interaction. The solid and dashed curves are obtained on equidistant meshes with the same q_{max} = 7 fm^{-1}, but different spacings Δq. The dotted curve illustrates that the tail of the singular value spectrum is related to the precision of the input data, which is reduced from 10 digits for the other data sets to 6 digits after the decimal. All conventions are the same as in Fig. 5.1.

ensure high accuracy in the *pp* and *np* $^1S_0$ partial waves. This threshold is discussed further in next subsection.

5.3.2 Singular Value Spectra of Nucleon-Nucleon Interaction

With the technical discussion out of the way, we can proceed to analyze the SVDs of NN interactions, such as the EM [22] and AV18 [109] potentials. As mentioned before, these interactions are accurate representations of nucleon-nucleon scattering data, but they have different characteristics. The EM potential is derived using chiral Effective Field Theory (EFT) and has a moderate initial cutoff. The interaction is non–local due to the adopted regularization scheme and is best represented in momentum space. On the other hand,

the AV18 potential is designed for use in coordinate–space Quantum Monte Carlo (QMC) calculations and is constructed to be as local as possible. Consequently, it has a strong, repulsive core in the interaction, which makes its use problematic in many–body methods that rely on basis expansions. Although newer versions of these interactions have been developed, EM and AV18 are still relevant for analysis because they contain all the essential features found in more recently developed interactions, as indicated in recent reviews [23, 79, 82].

As shown in Figures 5.1 and 5.2, the ${}^1S_0$ partial waves of the EM interaction exhibit a low rank structure, as evident from the singular value spectra. In the proton-proton (pp) channel, a "kink" is observed, indicating a natural threshold value of $\sigma_t = 10^{-3}$ fm^{-2} for truncating the SVD. This threshold value is approximately three to four orders of magnitude smaller than the largest singular values in the pp and neutron-neutron (np) channels for all partial waves up to $j = 9$, which are $\sigma_{\max}(pp) \approx \sigma_{\max}(np) \approx 3$ fm^{-2}.

The number of components of the interaction in the pp channel that have singular values above the threshold is approximately 35, while in the np channel, only about 10 components are above the threshold. The reason for this difference is due to the inclusion of the Coulomb interaction in the initial matrix elements, which is long–ranged and lacks an inherent scale. In the absence of a cutoff or regulator, the matrix representation of $(V_C)_{ij} \sim (q_i - q'_j)^{-2}$ would diverge on the diagonal, making it impossible to truncate the SVD in the pp channels. In this study, a hard cutoff is imposed at $R_C = 15$ fm, which serves two purposes: in phase–shift calculations, it provides the matching scale between the momentum–space wave function obtained from the matrix elements of the nuclear and cutoff Coulomb potentials $V_N + V_C$ and the asymptotic Coulomb wave function [64, 96]. In nuclear structure calculations, the impact of imposing this cutoff on Hartree–Fock and IM–SRG ground–state energies is below

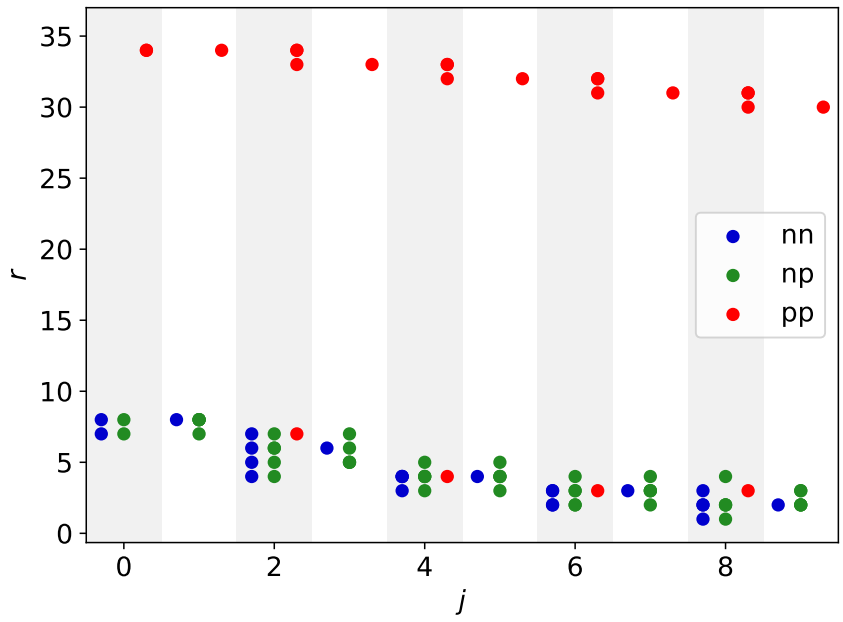

Figure 5.3: Truncated SVD rank r of partial waves up to $j = 9$ for the EM interaction, using a singular value threshold $\sigma_t = 10^{-3}$ fm^{-1}. Points for partial waves with different l and s can overlap. The maximal singular values for the interaction channels are$\{\sigma_{\max}(nn), \sigma_{\max}(np), \sigma_{\max}(pp)\} = \{3.00 \text{ fm}^{-1}, 2.97 \text{ fm}^{-1}, 3.06 \text{ fm}^{-1}\}$, respectively.

1 keV.

It is evident that changing the value of R_C will affect the number of components that exceed a pre-selected singular value threshold. If we are willing to accept a small impact on ground–state energies, which remains negligible compared to other sources of uncertainty, we can reduce the cutoff to $R_C \approx 10$ fm. Doing so would lower the rank of the truncated interactions studied to approximately 20 in the pp partial waves. However, any further decrease in R_C would cause a rapid deterioration in the energies and phase shifts.

The comparatively simple nature of V_C as compared to nuclear interactions could facilitate its efficient inclusion through means other than a truncated SVD in a chosen configuration space. However, in the context of the present study, it is important to note that V_C cannot be treated completely separately as it couples with the other terms in the Hamiltonian during the SRG evolution, even though it evolves weakly. One could try to create an

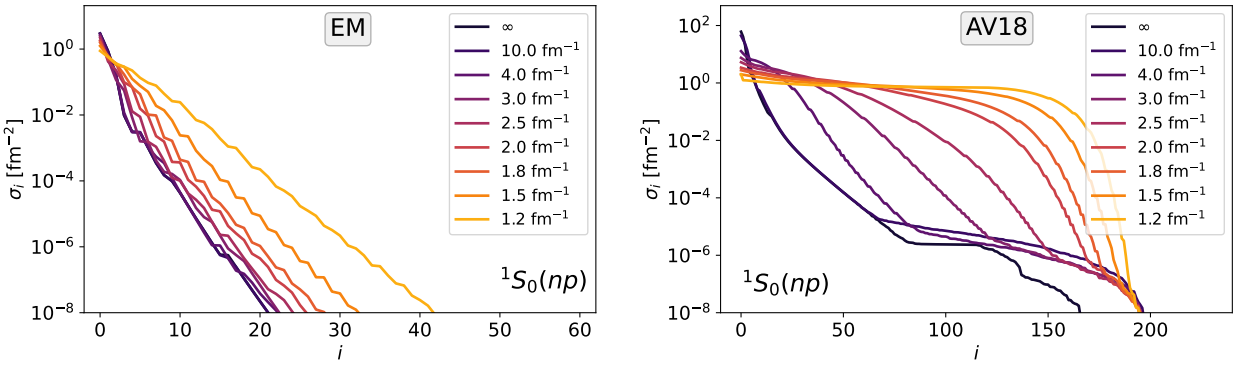

(a) (b)

Figure 5.4: Singular values of the neutron-proton $^1\mathrm{S}_S$ partial wave for the SRG-evolved EM (panel a) and AV18 interactions (panel b) at different resolution scales λ.

SRG evolution from T and the nuclear interaction V_N and apply it to V_C subsequently, as with other observables. However, when we attempted this, it resulted in effects on the order of several percent on the ground–state energies of medium–mass nuclei, which is comparable to or greater than other theoretical uncertainties for these quantities. This topic warrants further detailed exploration in the future.

As we move to higher partial waves, we see a consistent pattern across the different channels as shown in Figure 5.3. The number of singular values above the threshold $\sigma_t = 10^{-3}$ fm^{-2} is between 5 and 10 for np and nn partial waves up to $j = 9$. On the other hand, pp partial waves contain about 35 singular values above the threshold, which is due to the presence of the Coulomb interaction. However, for off–diagonal pp partial waves like $^3P_2 - {}^3F_2$, the number of components is comparable to that in the np and nn channels. This is because the Coulomb interaction cannot contribute to partial waves with $l \neq l'$, which further supports that increased number of relevant components in the $l = l'$ partial waves is due to the presence of V_C. The relative number of components in different partial waves is similar across different channels.

Next, we consider the impact of a free–space SRG transformation on the singular value

distribution. Figure 5.4 shows the singular values in the neutron-proton $^1S_0$ partial wave for the EM and AV18 interactions after they have been evolved to different resolution scales λ. For the EM interaction, we observe that the number of singular values beyond the threshold σ_t does not change substantially as we evolve from the initial interaction to $\lambda = 1.8$ fm^{-1}. However, if we continue to evolve the interaction to $\lambda = 1.5$ fm^{-1} and $\lambda = 1.2$ fm^{-1}, the growth of the rank accelerates, and its value becomes twice the value of the original interaction.

At low resolution scales, the evolution starts to affect the momentum transfers (cf. Eq. (2.26)) that arise from the dynamics of one–pion exchange. In a projective renormalization group (RG) approach, we would say that we are "integrating out" the pion [10, 11]. However, since the SRG is unitary, it cannot eliminate interaction strength, but only redistribute it. Within the two–body sector, the SRG increasingly diagonalizes the $V(s)$ by redistributing interaction strength toward the diagonal. As the band's width becomes narrow enough, the strength begins to move along the diagonal to higher momenta [10], and previously insignificant components of the flowing interaction may now become relevant.

It is crucial to consider the observed growth of the rank when we perform the SRG evolution directly in terms of the SVD factors, as explained in Section 5.3.1. Typically, we evolve the interaction to resolution scales around $\lambda \approx 2.0$ fm^{-1}, which has demonstrated to be an advantageous value for nuclear many–body calculations, thereby avoiding a substantial increase in rank. However, based on our present findings, it is recommended to "over–sample" and include additional components in the process to capture the renormalization group (RG) flow accuracy and prevent any loss of unitary in the two–body system.

In Figure 5.4b, we show the singular value spectrum of the AV18 interaction. The unevolved AV18 has a higher rank than the EM interaction because it has a greater extension in momentum space (also see Fig. 1.1). This is due to the AV18 interaction's hard core,

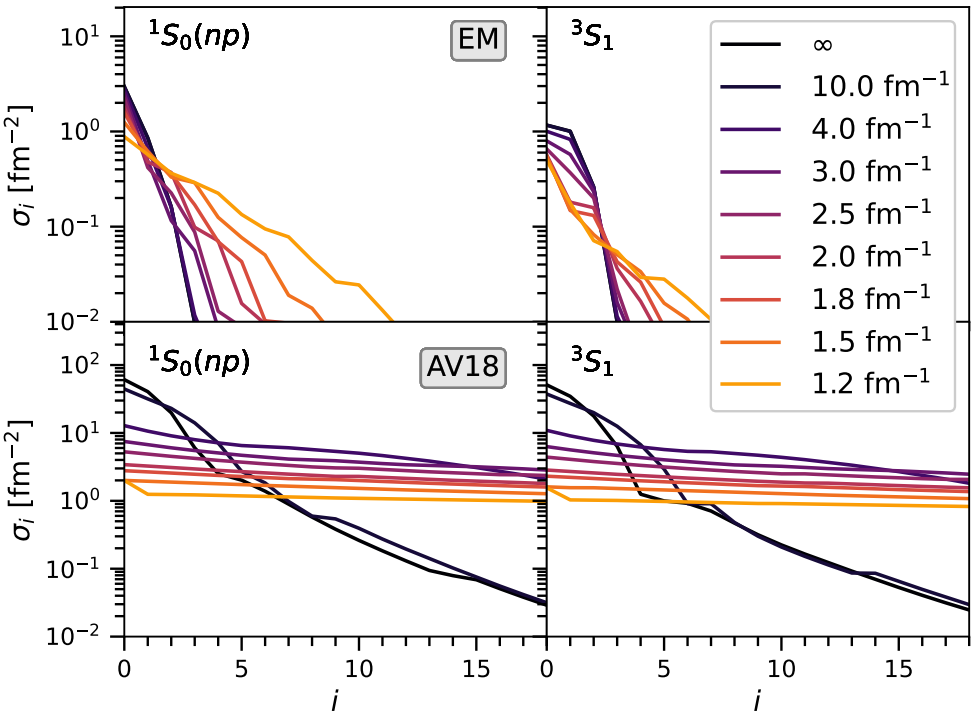

Figure 5.5: Detail view of the dominant singular values in selected S waves of the EM and AV18 interactions at different SRG resolution scales λ.

which allows it to easily connect incoming the outgoing momenta that couple by up to 20 fm^{-1}. When the AV18 interaction undergoes an SRG evolution, there is a significant change: the dominant singular values become smaller, but the rank rapidly expands. As a result, the interaction's spectrum becomes so flat that possible truncation points for the SVD are between 150 and 200 components, which are substantial portions of the full rank of the matrix.

Figure 5.5 presents a detailed view of the dominant singular values in the neutron–proton S waves of our interactions. In particular, for the EM interaction, we observe that only 2–3 singular values are highly dominant before the spectrum drops off rapidly. As we decrease λ, the relative dominance of one of these singular values increases compared to the others, before the growth of the rank becomes problematic beyond $\lambda = 1.8$ fm^{-1}. This finding is consistent

with the analysis of Bogner et al. [12], who showed that low-rank separable approximations to the NN interaction become more accurate as the resolution of the interaction is reduced. This is because the SVD can be considered as a generalization of such techniques.

Interestingly, the analysis presented in Ref. [12] arrived at a similar conclusion for a low-resolution V_{low-k} interaction that was obtained from AV18 through a projective RG decimation [10, 11]. Although only a few singular values dominate the spectrum at the beginning of our SRG evolution, the rapid flattening of the spectrum and the concurrent expansion of the rank seem to contradict the results obtained for V_{low-k}.

To address this discrepancy, we emphasize that the magnitude of a singular value is not always enough to determine whether a component of the interaction is significant for the physics we aim to explain or not. For example, suppose we have a local interaction with matrix elements in momentum space, which we can write schematically as

$$V_{\mathrm{reg}}(q, q') = V(q, q') f\left(\frac{q - q'}{\lambda}\right) \tag{5.23}$$

where f is a local regulator. In momentum space, the interaction between particles can be represented by a matrix that has a band diagonal structure. The parameter λ, which is named suggestively, determines the width of the band. However, both the strength of f and λ do not impose any limit on the total momentum of the particles (represented by $q + q'$). The AV18 potential is an example of a local potential with a strong repulsive core, and it has significant positive matrix elements at high momenta (see Figure 1.1 or Fig. 2 in Ref. [10]). The eigenvalues of the AV18 potential are dominated by the high–momentum region and are larger in magnitude than the negative eigenvalues from the attractive region at low momentum. The singular value spectrum reflects only the absolute value of the two

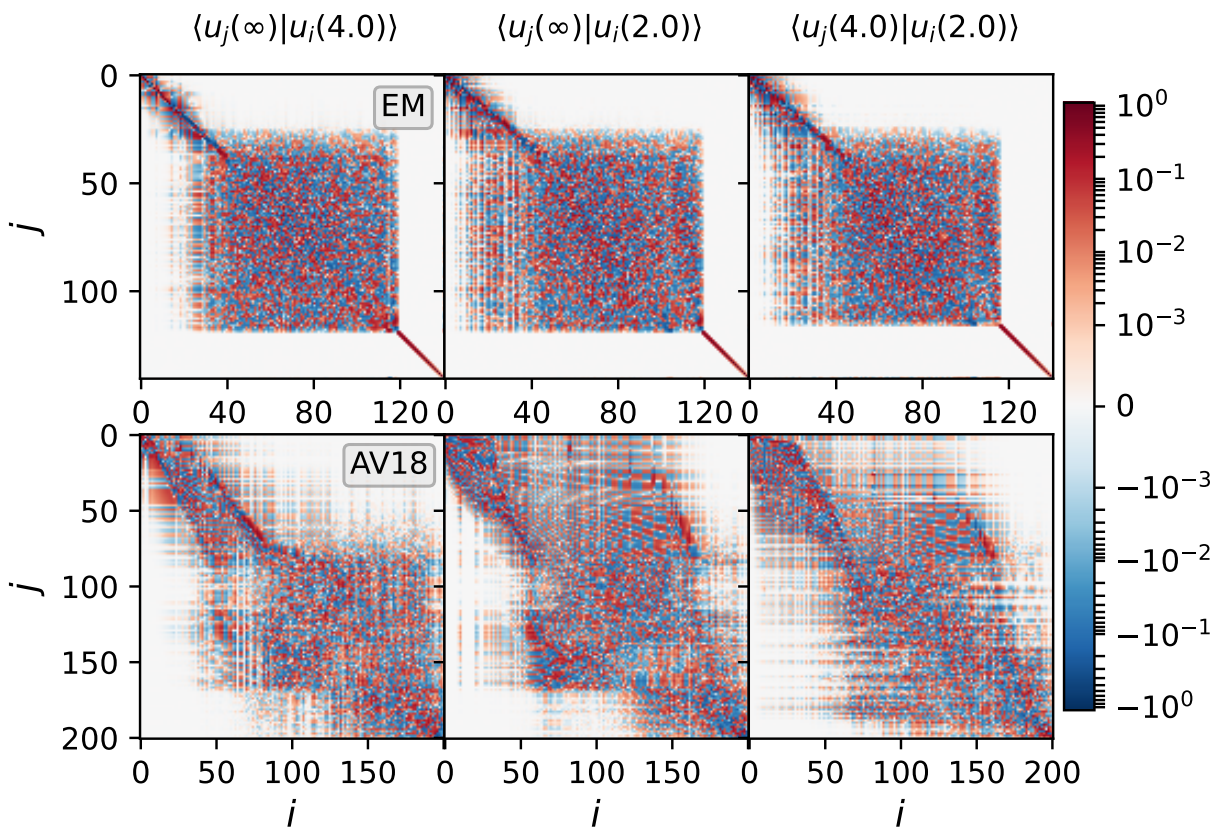

Figure 5.6: Matrix representation of the unitary transformation $U(\lambda_1, \lambda_2) = \langle u_j(\lambda_1)||u_i(\lambda_2)\rangle$ between the initial and final resolution scales $\lambda_1, \lambda_2 \in \{2\ \text{fm}^{-1}, 4\ \text{fm}^{-1}, \infty\}$. Here, we specifically focus on the ${}^1S_0(np)$ partial wave. The basis vectors are ordered by decreasing singular value. Note the logarithmic color scale.

types of eigenvalues, which get mixed together.

Additional information that may aid in determining the relevance of an interaction component is present within the structure of the associated singular vectors. As our primary focus lies in the behavior of these vectors under component–wise SRG evolution, we examine the expansion of one set of singular vectors, denoted as $|u_i(\lambda)\rangle$ (or $|v_i(\lambda)\rangle$), in terms of another set at different λ value. The coefficients of this expansion correspond to the entries of the unitary evolution matrix (5.12), but with the constraint that neither of the scales is set to $\lambda = \infty$ (or, equivalently, $s = 0\ \text{fm}^4$).

Figure 5.6 displays matrices for different values of (λ_1, λ_2), namely $(\infty, 4.0\ \text{fm}^{-1})$, $(\infty, 2.0\ \text{fm}^{-1})$

and $(4.0\ \mathrm{fm}^{-1}, 2.0\ \mathrm{fm}^{-1})$. Considering the EM interaction first, we note that the matrices appear similar , containing a washed out diagonal band in the upper left corner, a large central block, and a sharp diagonal in the lower right corner. It is relatively simple to connect the matrices shown in Figure 5.6 to our findings for the truncated SVD of the interaction. As depicted in Figure 5.4, the upper left and central blocks of the matrices contain the $|u_i\rangle$ of the singular values $\sigma_i \gtrsim 10^{-6}$ and $\sigma_i \lesssim 10^{-6}$, respectively. The separation point between the blocks is likely determined by the precision settings of the ODE solver, as revealed in our analysis. Additionally, the lower right block of the matrices comprises the singular vectors that remain constant, indicating that $V = 0$ and $H = T$. The block structure is the result of the nonlocal regularization of the interaction. This regularization suppresses the momentum space matrix elements *independently* for incoming and outgoing momenta, as indicated by the equation

$$V_{\mathrm{reg}} = V(q, q') \exp\left(-\left(\frac{q}{\Lambda}\right)^{2n}\right) \exp\left(-\left(\frac{q'}{\Lambda}\right)^{2n}\right) \tag{5.24}$$

where $n = 2$ or $n = 3$ and $\Lambda = 2.5\ \mathrm{fm}^{-1}$ [22]. Due to the matrices' structure, the first r singular vectors remain nearly unconnected from the rest of the spectrum as we evolve. However, it should be noted that the central block extends towards lower indices in the $U(\infty, 2.0)$ matrix, indicating a slight increase in rank, as also noted in our discussion of Fig. 5.4 and 5.5. This phenomenon is less apparent in $U(4.0, 2.0)$ because the two evolved bases are more alike.

In the case of AV18, the structure of the unitary transformations is considerably more intricate. The constituents that will have the greatest impact on the low–momentum region are distributed throughout the basis, making it challenging to identify ahead of the evolution. As we evolve, the $U(\infty, \lambda)$ matrices become less organized, which corresponds to the increase

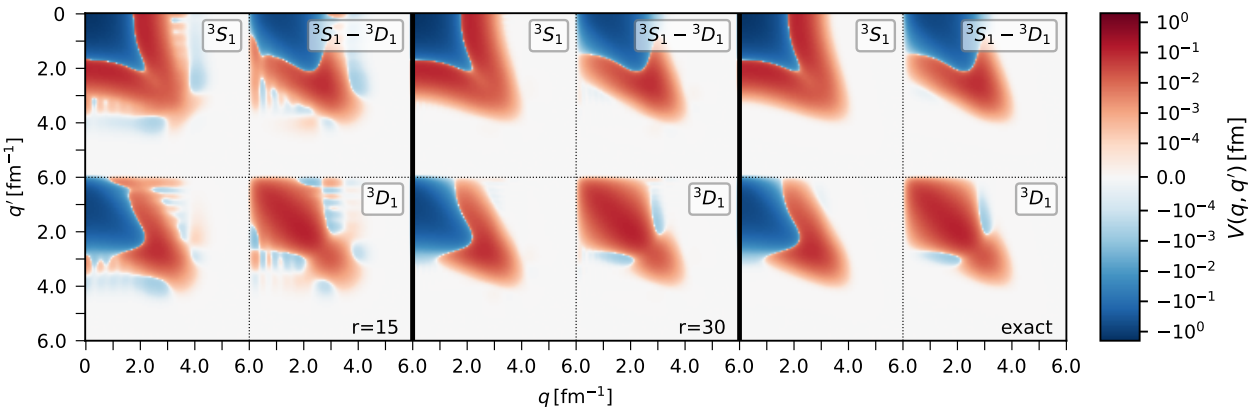

Figure 5.7: Momentum-space matrix elements of the EM interaction at $\lambda = 2.0$ fm^{-1} in selected uncoupled partial waves. The top panels are by SVD-SRG, the bottom panels by conventional matrix-based SRG evolution. The matrix elements are given in scattering units ($\hbar = c = \hbar^2/m = 1$). Not the logarithmic color scale.

in rank observed in Figure 5.4. The matrices indicate that we can expect to use around 160 to 170 out of 200 interaction components to apply the SRG using the interaction's factorized form. However, there is a simplification in the structure of the $U(4.0, 2.0)$ matrix. If we perform the SVD at $\lambda = 4.0$fm^{-1}, we may be able to enhance the low–rank structure by safely removing the high–momentum components that are already decoupled, similar to what is done in V_{low-k}. In the next subsection, we will see further evidence of this when we discuss the deuteron ground-state energy for AV18 (cf. Figure 5.12).

The main conclusion from our analysis is that while the magnitude of the singular values is an important factor to consider when determining the necessary singular vectors for an effective low–rank representation of interaction in the low–momentum regime, it alone is not sufficient. In addition, other criteria that account for the momentum structure of the singular vectors may need to be taken into consideration. Specifically, when dealing with chiral interactions that employ nonlocal regulators, the selection process based solely on the singular values can be effective if the initial cutoff is not set too high, as there are generally not many strongly positive eigenvalues present in this scenario.

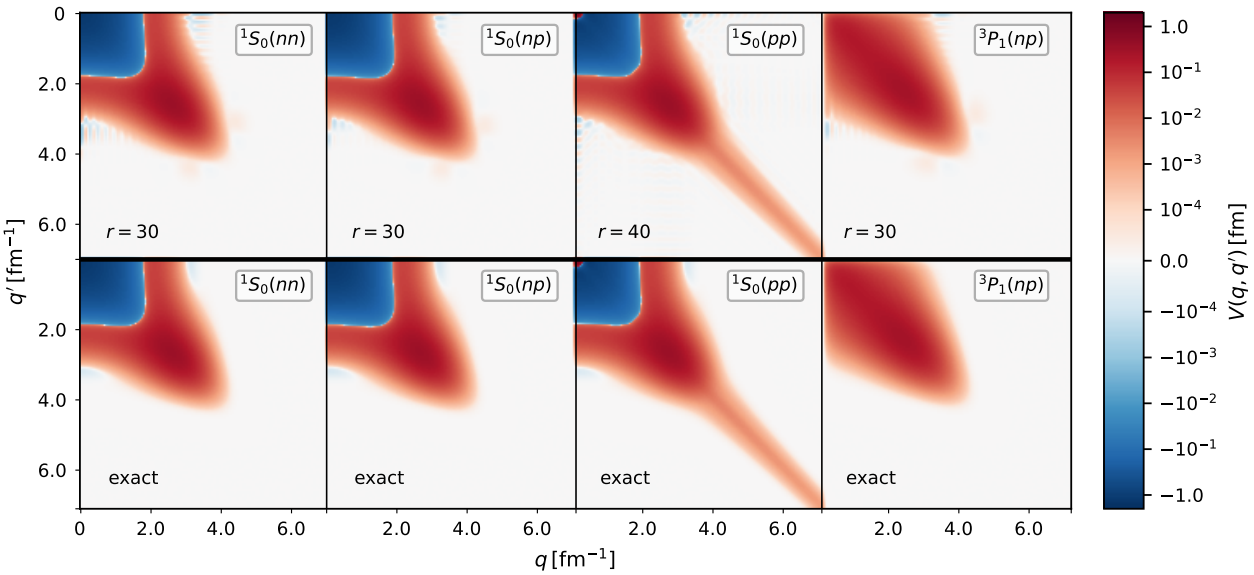

Figure 5.8: Momentum-space matrix elements of the EM interaction at $\lambda = 2.0$ fm^{-1} in selected uncoupled partial waves. The top panels are obtained with SVD-SRG, the bottom panels with conventional matrix-based SRG evolution. The matrix elements are given in scattering units ($\hbar = c = \hbar^2/m = 1$). Note the logarithmic color scale.

The situation is more complex when dealing with local interactions, as the potential's behavior and regularization at both short and long distances impact the interaction's rank. Although the Coulomb interaction is singular in S waves as the distance between particles approaches zero, its rank is predominantly influenced by the regularization of its long–range behavior, thus allowing for an accurate low–rank expansion. In contrast, the AV18 interaction cannot undergo significant rank reduction because it strong short-range coordinate-space potentials that parameterize (multi)meson exchange interactions, and we are sensitive to their effects because of AV18's high resolution scale. Comparable issues are likely to arise with local or semi-local chiral interactions, as noted in previous studies [23, 79], although their lower resolution scale could help mitigate these concerns.

5.3.3 SVD-Based SRG Evolution

In this section, we implement the SRG evolution of an SVD–factorized interaction, abbreviated as SVD–SRG, using the framework developed in Section 5.2. As an example, we perform the SVD–SRG evolution of the EM interaction at $\lambda = 2.0$ fm^{-1}. Figure 5.7 depicts the momentum space matrix elements in the deuteron channel for various SVD ranks. Using only 15 components per partial wave, some distortion is still observed. However, with 30 components, the SVD-SRG evolution reproduces the results from evolving with the complete matrix accurately, with absolute deviations of roughly 10^{-4} that are only visible upon close examination. It is worth noting that we did not attempt to fine–tune the rank r using the information from the previous section (e.g., Figure 5.3). Instead, the decision to employ the same rank for all partial waves was solely made for the sake of convenience.

In Figure 5.8, we investigate the efficacy of the SVD–SRG approach in other selected partial waves. The matrix elements for the neutron–neutron and neutron–proton partial waves were obtained using 30 components, while 40 components were necessary for the $^1S_0$ proton–proton partial wave due to the presence of the Coulomb interaction, as evidenced by the Coulomb tail along the diagonal, which is absent in other isospin channels. Weak oscillations and "fraying" can be observed around the edges of the primary structures, but the deviations' absolute values are again at or below 10^{-4}.

Given the efficacy of the SVD–SRG on the matrix element level, we have utilized the factorized interactions to calculate nucleon–nucleon observables, such as scattering phase shifts and the binding energy of the deuteron. In Figure 5.9, we present the *np* phase shifts and mixing parameter of the SVD–SRG evolved EM interaction in the deuteron channel, as well as selected partial waves. The results indicate that about 5 to 10 interaction components

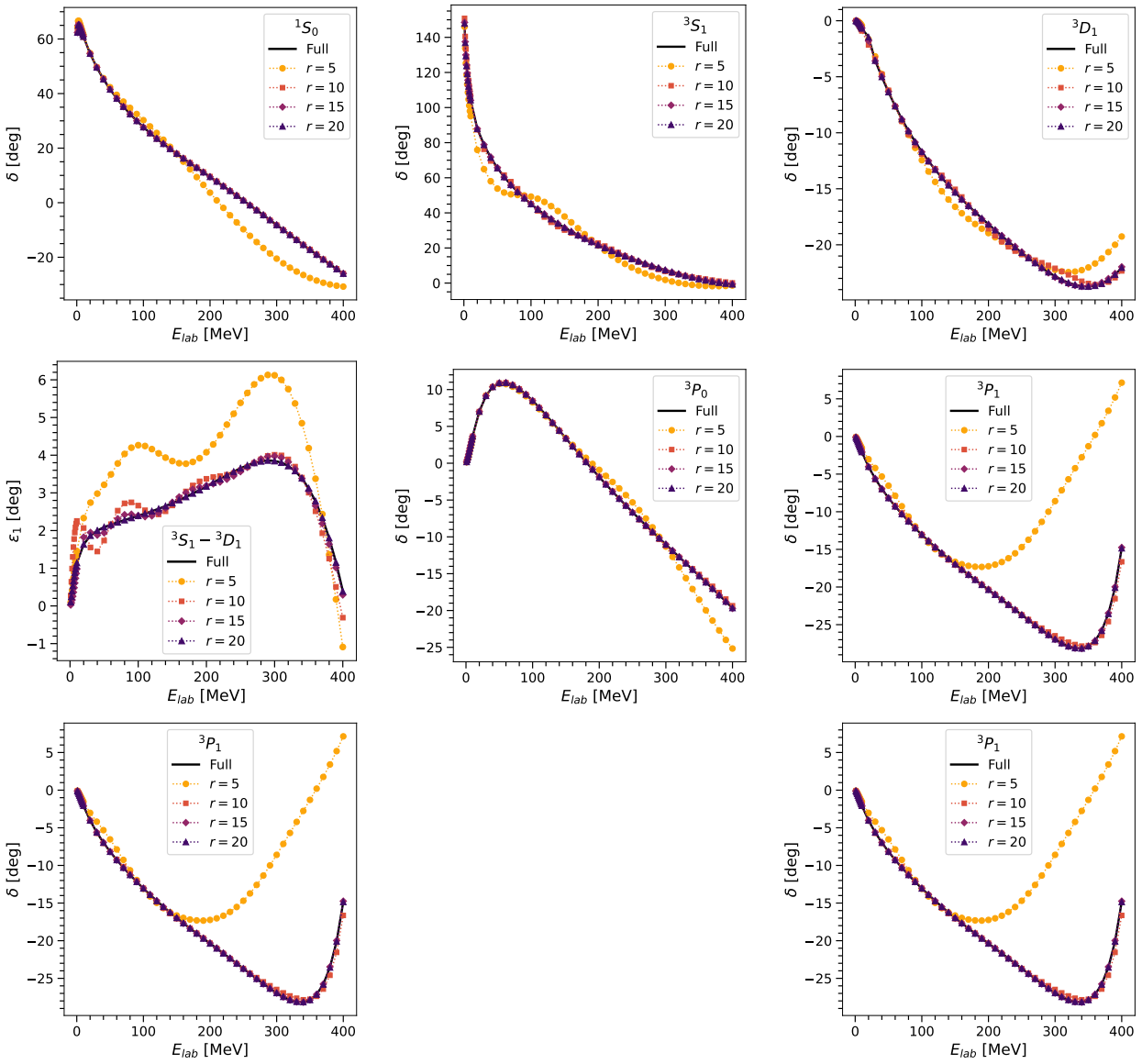

Figure 5.9: Selected neutron–proton phase shifts and mixing angles of the EM interaction resolution λ = 2.0 fm^{-1}. The SVD–SRG evolution for different ranks is compared to the matrix–based evolution, which exactly preserves the phase shifts of the unevolved EM interaction by construction.

are sufficient to achieve agreement with conventional matrix–based evolution, with only the ${}^3S_1 - {}^3D_1$ mixing angle ϵ_1 requiring a few additional components. These findings align with our expectations based on the SVD of the initial interaction (cf. Figure 5.3), and the need to accommodate a slight increase in rank via "over-sampling" as we evolve to $\lambda = 2.0$ fm^{-1}.

When dealing with the Coulomb interaction in the proton–proton channel, we have found it necessary to increase the number of components to $30-35$, as indicated by the partial wave and mixing angle results in Figure 5.10. Initially, the convergence of the phase shift with the rank r may appear irregular. However, this is a result of gradually including components based on the size of the associated singular value alone, regardless of whether they are dominated by the Coulomb or the nuclear interaction. As we increase the rank from 25 to 30, we add components that are primarily influenced by V_C, which significantly affects the phase shifts at low energy or long distances. While this effect is somewhat obscured by the overall size of δ in the ${}^1S_0$ phase shift plot, it is quit clear in higher partial waves. Increasing the rank from $30-35$ adds components that are dominated by nuclear interactions, which have a substantial impact on the $E_{\text{lab}} = 100-250$ MeV region, and for $r > 35$, the phase shift is essentially converged.

Next, we investigate the SVD–SRG evolution of the deuteron ground–state energy E_d as a function of resolution scale and rank per partial wave in Figure 5.11. The energy E_d should be unaffected by unitary transformations in the two–body system, and therefore, the curves for different resolution scales (λ) should collapse once sufficient components have been included. At $r = 12$, the deviations from the exact outcome are in the few–keV range, consistent with the slower convergence of the mixing angle ϵ_1 with rank r than with other np scattering quantities discussed earlier. At lower ranks r, we observed that the artifacts due to the violation of the unitarity of the evolution get more pronounced as λ decreases.

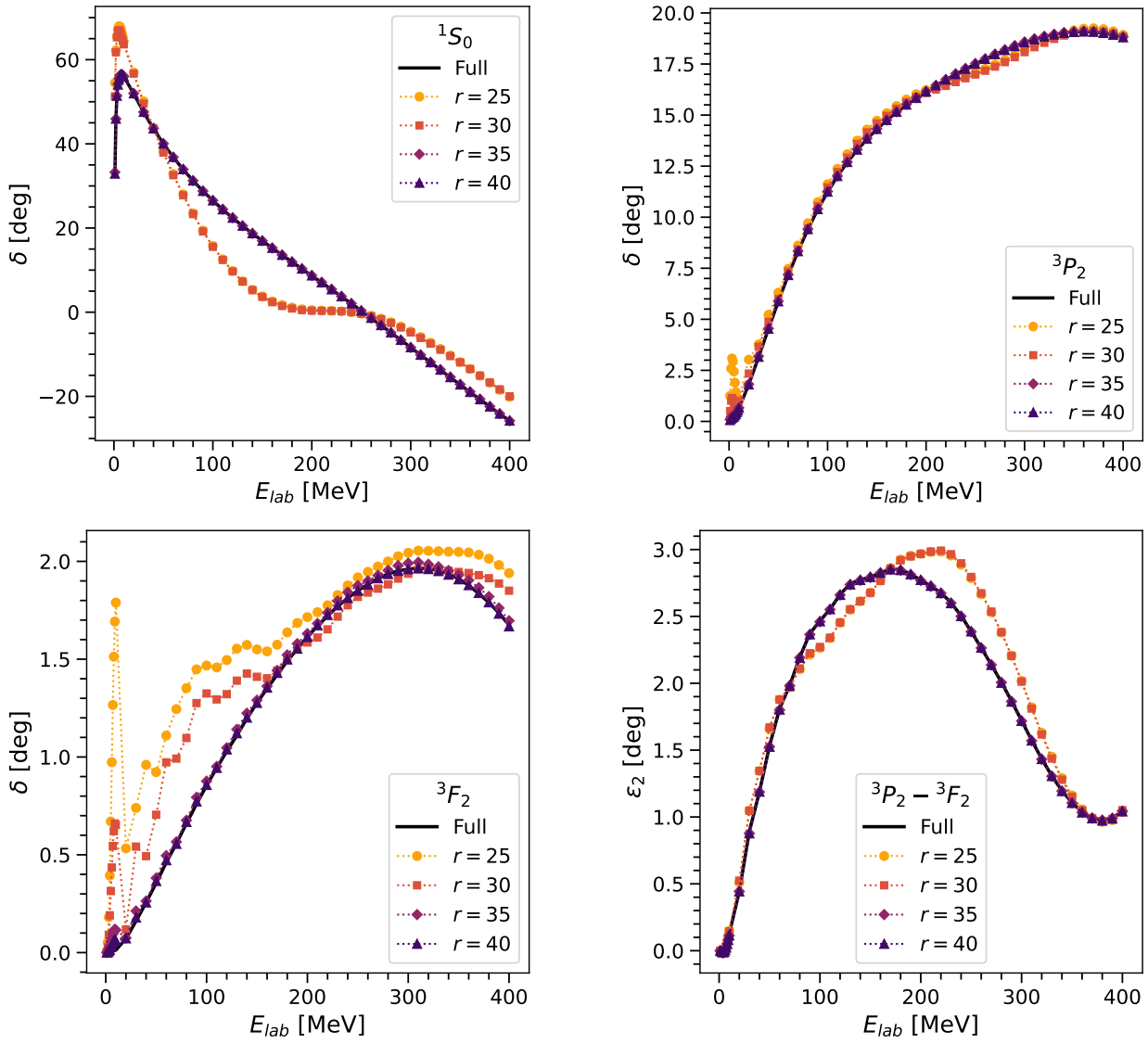

Figure 5.10: Selected proton-proton phase shifts and mixing-angles of the EM interaction resolution λ = 2.0 fm^{-1}. Note the higher ranks for the SVD-SRG evolution compared to Figure 5.9.

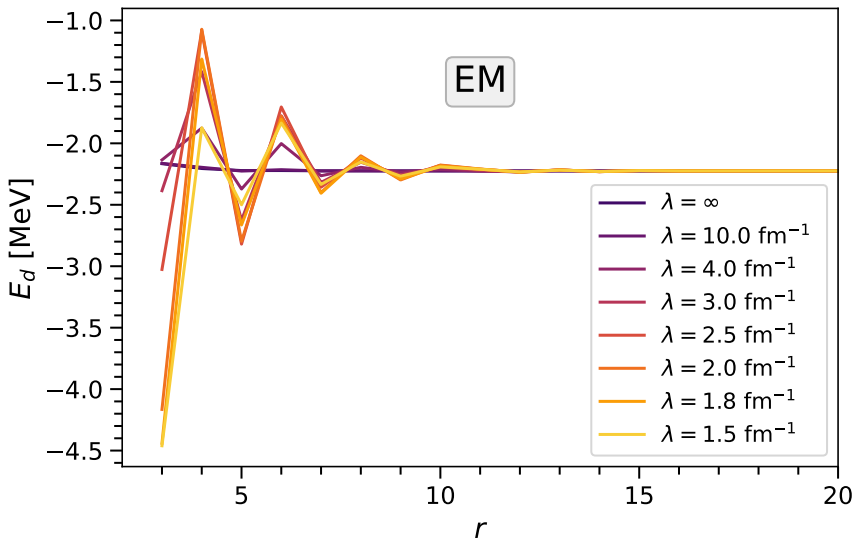

Figure 5.11: Ground-state energy of the deuteron for the SVD-SRG-evolved EM interaction at different resolution scales λ. Here, r refers to the number of components per partial wave.

This is because the rank of the interaction starts to grow more rapidly once the SRG begins to reshuffle the long-range pion physics, as explained in Section 5.3.2.

In general, the outcomes of SVD–SRG evolution for the EM interaction indicate that the method is effective for chiral NN interactions, especially for those that adopt nonlocal regularization schemes. However, for a hard interaction such as AV18, the story is quite different. When we apply the SVD method based on the singular values of AV18, almost all components must be kept to reproduce observables in the two–nucleon system. We present the AV18 deuteron ground–state energy in Figure 5.12 as an example, where approximately 170 singular components are required to maintain the invariance of the energy. At lower resolution λ, there are plateaus, indicating that many interaction components no longer contribute to the energy due to the decoupling of momentum scales. As λ decreases, these plateaus become more prominent, indicating that low–rank approximations to the evolved AV18 interaction are more accurate, as observed in the V_{low-k} approach by Bogner [12] et al., and in line with our discussion in Section 5.3.2. Unfortunately, the structure of unitary

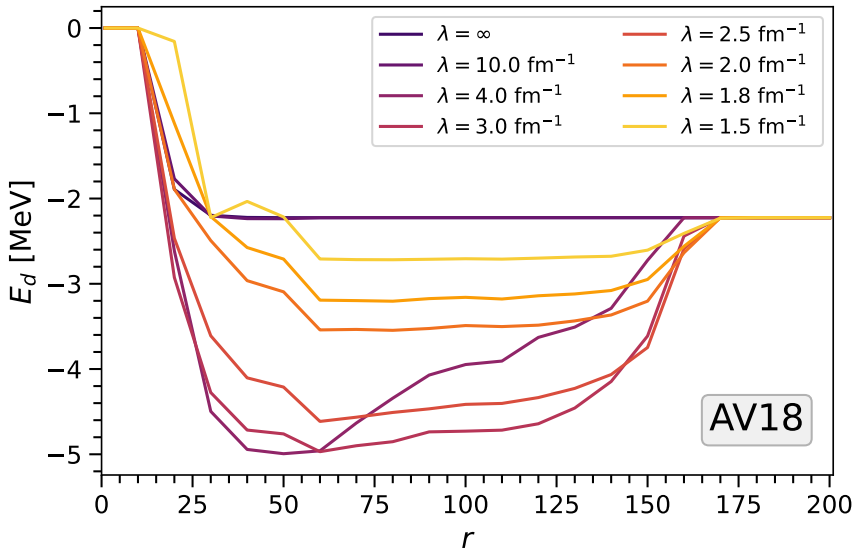

Figure 5.12: Ground–state energy of the deuteron for the SRG–evolved rank–r approximation of AV18 at different resolution scales λ.

transformation (5.12) (cf. Figure 5.6) is too complex to allow us to restrict the evolution only to these components early in the flow.

5.3.4 Harmonic Oscillator Basis

In the process of preparing the nuclear interaction for many–body methods in configuration space, at some point a basis change from relative momentum states to (spherical) harmonic oscillator (HO) states is performed. The HO basis is commonly used in nuclear many-body calculations because it allows the exact separation of the center–of–mass and intrinsic degrees of freedom in many–body states, especially when working in E_{max}–complete Hilbert spaces. In such spaces, the total energy of the oscillator state is characterized by $E_{max} = \sum_i (2n_i + l_i)$, as explained in previous works (e.g., [39]). In this study, we have two options to perform the SRG evolution: either change the basis of the singular vectors from momentum to HO states through a unitary transformation or directly implement the SVD–SRG in HO representation. The latter option is more practical when evolving three–nucleon

forces in an E_{max}–complete Jacobi–HO representation, because the antisymmetrizer has a block–diagonal structure that makes it easier to implement [34, 35, 49, 74, 84].

In this study, we have implemented both the momentum–space and harmonic oscillator (HO) approaches and demonstrated that they produce consistent results for the deuteron ground–state energy. This is illustrated for the SVD–SRG evolved EM interaction at a resolution scale of $\lambda = 2.0$ fm^{-1}, as shown in Figure 5.13. Similarly to Figure 5.11, the behavior of E_d should become invariant under SVD–SRG evolution once the rank is sufficiently high. We observe that this occurs at $r \approx 15$, which is independent of the HO energy scale $\hbar\omega$. For $r < 15$, the behavior of E_d is similar to that of the momentum–space SVD-SRG, which is also shown for comparison (as seen in Figure 5.11). It should be noted that the magnitude of the deviations from the exact value weakly depends on $\hbar\omega$, and deviations from the momentum–space curve are more significant for the lowest and highest value of $\hbar\omega$. These choices correspond to adjusting the effective infrared and ultraviolet cutoffs of the finite HO basis to the scales of the problem (in this case, the deuteron wave function). This topic has received significant attention in recent years in the context of large-basis extrapolations [19, 28, 54, 69, 76, 105].

The key point that we can take away from our analysis is that the SVD–SRG method performs as well in the harmonic oscillator representation as it does in the momentum–space framework, and the conclusions regarding the rank of nuclear interactions hold true, whether for the better (EM) or worse (AV18) case. Furthermore, the representations of the nuclear potential in the momentum and harmonic oscillator bases are quite similar, and although the kinetic energy operator is tri-diagonal rather than diagonal in the harmonic oscillator representation, it can only connect basis states that are close in energy. Therefore, the structure and action of the generator will also be very similar.

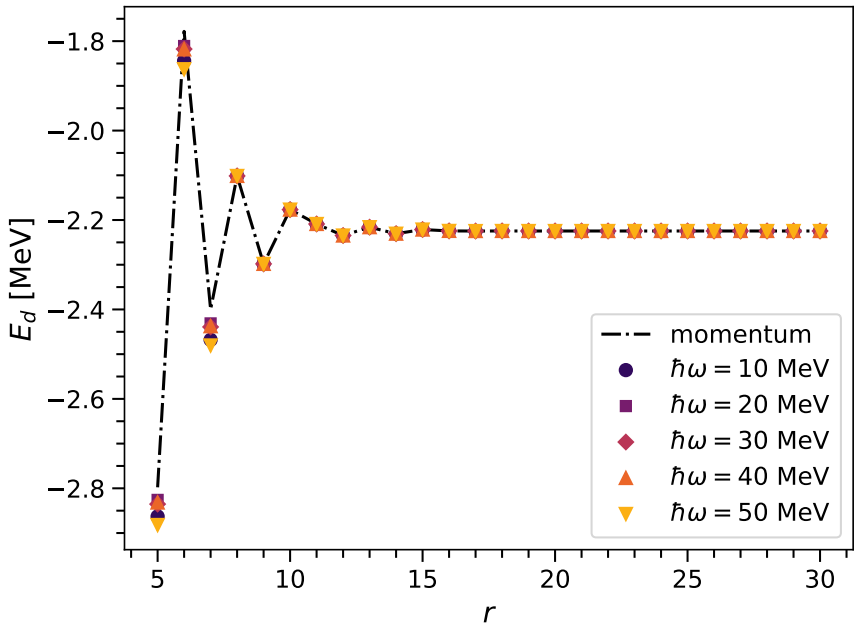

Figure 5.13: Deuteron ground–state energy of the SVD–SRG evolved EM interaction at $\lambda = 2$ fm^{-1} as a function of the rank. The SVD–SRG and subsequent diagonalization are performed in relative HO bases with different $\hbar\omega$.

5.4 Transformation to the Laboratory Frame

Moving on from investigating the SVD and SVD–SRG in the two–body system, our next objective is to employ factorized interactions in many-body computations. To that end, we need to analyze the Talmi-Moshinsky transformation of the interaction from the intrinsic frame, which is described by center-of-mass and Jacobi HO states, to the laboratory frame [51]). The singular vectors are coupled to the center–of–mass HO states

$$|N_{\mathrm{cm}} L_{\mathrm{cm}}, u_i \alpha; JM\rangle \equiv \sum_{M_{\mathrm{cm}} m} \langle L_{\mathrm{cm}} M_{\mathrm{cm}} j m \,|\, JM\rangle \, |N_{\mathrm{cm}} L_{\mathrm{cm}} M_{\mathrm{cm}}\rangle \bigotimes |u_i \alpha j m\rangle \tag{5.25}$$

where we have defined the collective partial wave index $\alpha \equiv (lsTM_T)$ for brevity. The corresponding right singular vectors can be constructed analogously. All singular vectors can be transformed individually using the unitary Talmi-Moshinsky transformation matrix.

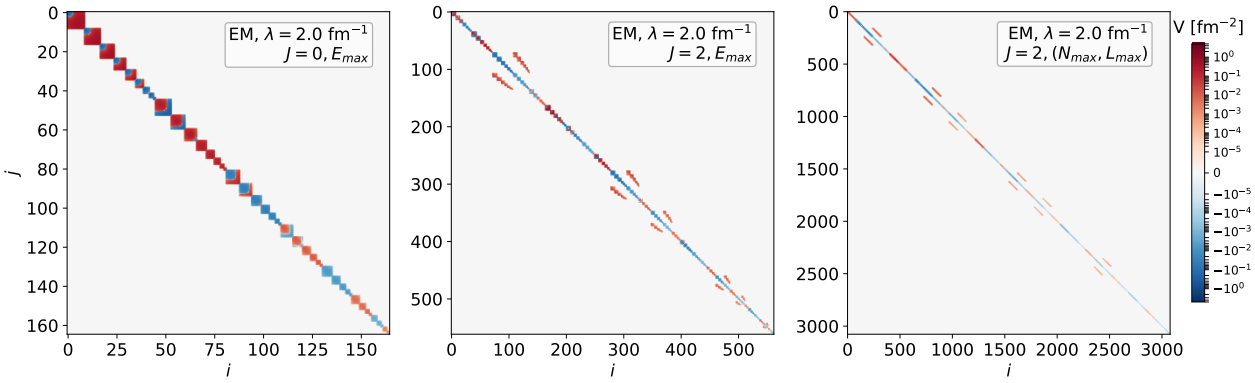

Figure 5.14: Matrix elements in the $J = 0$ and $J = 2$ channels of the EM interaction at resolution scale $\lambda = 2.0$ fm^{-1}, represented in the HO states $|N_{\rm cm}L_{\rm cm}, n(ls)j; JTM_T\rangle$. The left and center panels are obtained with an $E_{\rm max} = 16$ truncations, while the right panel uses $(N_{\rm cm}, L_{\rm cm}) = (8, 16)$ (see text).

It is evident from Eq. (5.25) that every singular vector and singular value will appear k times, where k is the number of center–of–mass states. In the extended basis (5.25), the matrix representation of V can be obtained by performing the Kronecker product of the identity matrix in the center–of–mass space with the factorized interaction in the relative space. For illustration, we present the matrices obtained for the EM interaction at $\lambda = 2.0$ fm^{-1} in the $J, T, M_T = (0, 1, 0)$ and $(2, 1, 0)$ channels in Figure 5.14. The size and structure of the matrices are dependent on the truncation we apply to the oscillator basis: We can use an $E_{\rm max}$ truncation and require

$$\begin{aligned} E &= 2N_{\rm cm} + L_{\rm cm} + 2n + l \\ &= 2n_1 + l_1 + 2n_2 + l_2 \leq E_{\rm max} \end{aligned} \tag{5.26}$$

(with single–particle oscillator quantum numbers n_i, l_i in the laboratory frame), or we can introduce independent truncations $N_{\rm cm}, n \leq N_{\rm max}$ and $L_{\rm cm}, l \leq L_{\rm max}$. In the $E_{\rm max}$ truncation, we decrease the size of the partial-wave copies as $N_{\rm cm}$ grows (as depicted in the left and center panels of Figure 5.14), leading to a change in the size of the singular values resulting

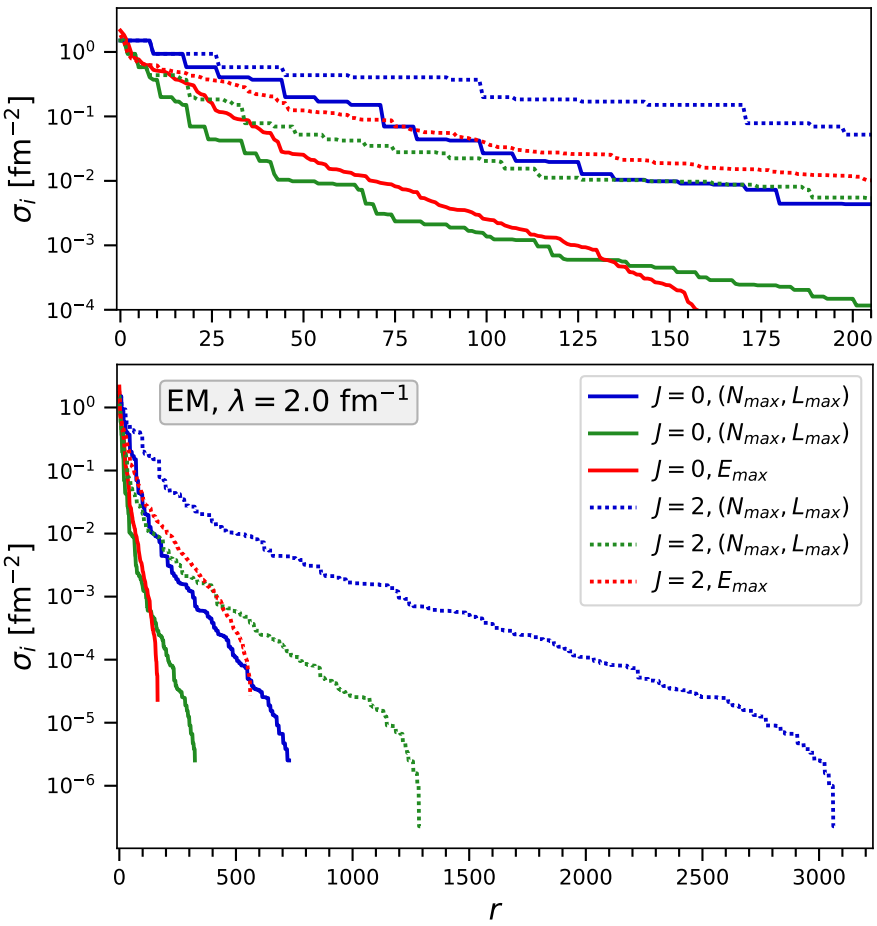

Figure 5.15: Singular values of matrices shown in Figure 5.14 (plus the $J = 0$ channel in $(N_{\max}, L_{\max}) = (8, 16)$ truncation). The green curves are obtained by compressing duplicate singular values from the full $(N_{\max}, L_{\max}) = (8, 16)$ sets.

from the projection into a smaller space. In contrast, an $(N_{\max}, L_{\max})$ truncation yields exact replicas of the partial waves (as shown in the right panel).

Figure 5.15 illustrates the singular value spectra of the aforementioned matrices. It is not surprising that the factorized matrix with truncation $(N_{\max}, L_{\max})$ has more significant singular vectors than the $E_{\max}$ truncation. However, the former is easier to compress because we would only need to store one representative for each group of identical copies of a given partial wave. On the other hand, the factorized matrix in $E_{\max}$ truncation is not readily compressible due to the projection of the relative partial wave into smaller bases, and the

resulting change of the singular values. Although the ranks of the $E_{\max}$ and $(N_{\max}, L_{\max})$ matrices are roughly similar overall, a closer examination of the dominant singular vectors indicates a slight advantage for the latter (see top panel of Fig. 5.15).

In the case of $(N_{\max}, L_{\max})$, the rank of the interaction in each channel is determined by adding the ranks of the partial waves that meet the selection rules for angular momentum and parity. For instance, in the $(J, T, M_T) = (0, 1, 0)$ channel, the rank is the summation of the ranks of all $T = 1$ neutron-proton partial waves, where each relative angular momentum j is coupled with the corresponding $L_{\rm cm}$ to yield a total angular momentum $J = 0$. For the $(J, T, M_T) = (2, 1, 0)$ channel, all partial waves with $|L_{\rm cm} - 2| \leq j \leq L_{\rm cm}+2$ are permitted, and the number of allowed couplings will increase with the total J. This observation aligns with a recent investigation that applied tensor factorizations to nuclear interactions and found that their rank increases with J [94].

In summary, we observed that the embedding of partial-wave factorized interactions into a larger space ahead of the Talmi–Moshinsky transformation to the laboratory frame, creates duplicates of the singular values that formally increase the rank of the interaction. Our analysis suggests that the best approach to address this issue in a matrix formulation is to perform the transformation in $(N_{\max}, L_{\max})$ truncation, as this ensures that the duplicates are identical and eliminates the need for additional storage. A more significant version of this problem emerges in the SVD-SRG implementation for three–body forces, where embedding the two–body relative partial waves into the three–body relative partial waves is necessary to track induced forces [35]. We will come back to this problem in chapter 6.

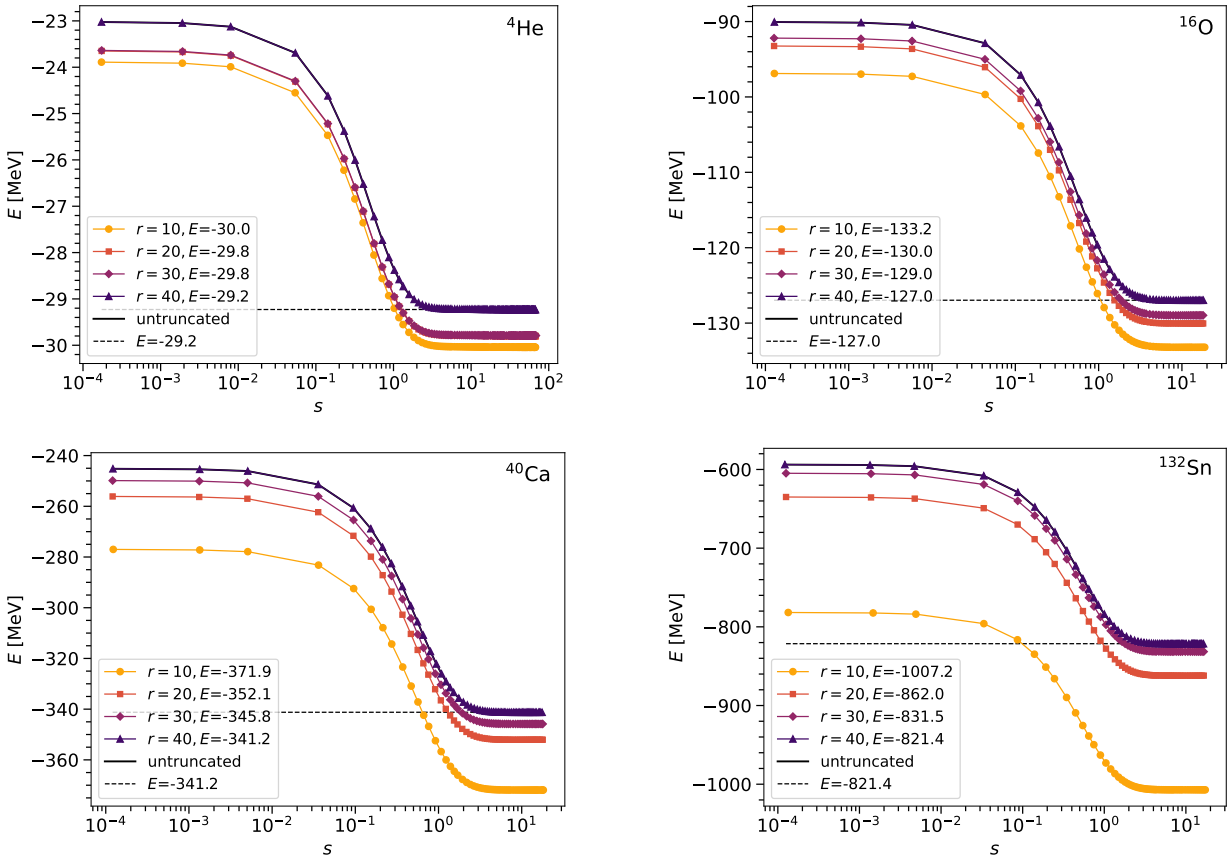

Figure 5.16: IMSRG(2) ground–state energies of selected closed–shell nuclei as a function of the flow parameter s for the EM1.8/2.0 $NN+3N$ interaction (see [33] and text). The SVD–SRG with different ranks (per partial wave) is used to construct the evolved NN component of the interaction. The results are obtained for a HO basis with $e_{\max} = 8, E_{3\max} = 14$ and $\hbar\omega = 20$ MeV, which is sufficiently close to convergence with respect to basis truncations for the EM1.8/2.0 interaction and these nuclei.

5.5 Many–Body Calculations

The final topic we want to address in this chapter is the application of the factorized interactions in many–body calculations. Here, we focus on testing the accuracy of rank–r SVDs by reconstructing the interactions from the factors as we feed them into our many-body methods. In chapter 7, we will attempt to reformulate the IMSRG approach to leverage the factorization directly.

In Figure 5.16, we present results of ground–state energy computations for closed–shell

nuclei in the IMSRG(2) approach [37, 39]. They were obtained using the EM1.8/2.0 interaction, which encompasses the EM interaction progressed to λ = 1.8 fm^{-1} and an NNLO $3N$ interaction with cutoff λ = 2.0 fm^{-1}. The low–energy constants of this interaction have been calibrated to the triton binding energy and ^4He charge radius [33, 75]. Although this interaction is not entirely consistent from the chiral EFT perspective, it has been empirically successful in describing the ground–state energies of a large number of nuclei, albeit while underestimating radii by a few percent (see [40] and the cited literature, particularly [91]). Thus, we view calculations with EM1.8/2.0 as a benchmark for the performance of the factorized interactions under "realistic" conditions. If we solely rely on the SVD–SRG evolved NN interaction, it is well known that nuclei will be overbound and much too small (see [39] and the behavior of the NN-only triton energy in Fig. 2.4, for example).

We find that we need 30–40 components per partial wave in the SVD–SRG interaction to recover the results without factorization accurately, with no attempts to fine tune the decomposition at this stage. This observation is in line with our findings in the two–nucleon system. This encompasses both the Hartree–Fock calculations used to prepare the reference states for normal ordering (cf. Section 1.3.7) and the full IMSRG(2) flow of the ground–state energy concerning as a function of the flow parameter s (cf. Chapter 3 and Refs. [37, 39]). As in our applications in the two-nucleon system, the need to include 30–40 components is primarily driven by the SVD of the Coulomb interaction V_C between the protons — for calculations with the strong interaction alone, 5 to 10 components are sufficient for highly precise reproduction of the full flow, but the results do not describe realistic nuclei.

Looking in more detail, it is evident that the convergence of the studied nuclei is not completely uniform. For example, the ground–state energy of ^4He remains almost the same as the rank increases form r = 20 to 30, while ^{16}O and ^{40}Ca experience a significant gain

of several hundred keV and a few MeV, respectively. Additionally, we note that further increasing the rank to 40 results in more considerable changes in the ground–state energies of ^4He and ^{16}O, while the change in ^{40}Ca is smaller. As noted in our discussion of the *pp* phase shifts in Section 5.3.3, these findings can be attributed to the inclusion of interaction components based on the size of their associated singular values alone, leading to an alternation between components of the nuclear and Coulomb interactions that affects these nuclei differently, given the significantly different proton numbers. Furthermore, $^4He, ^{16}O$ and ^{40}Ca probe the interaction at increasingly higher (laboratory–frame) angular momenta, hence it is reasonable to expect that specific interaction components may only become relevant for heavier masses.

We have confirmed that the ground–state energies of the chosen nuclei reach convergence by gradually increasing the rank from 40 to the full rank. We have not included the graphs of these curves in Figure 5.16 to avoid confusion, but we refer the reader to Figure 5.17, which illustrates that the rank of 40 produces a precise and convergent replication not just of the ground-state energies but also of the root-mean-square radii of the studied nuclei.

To explore the performance of the SVD–SRG for general observables, we construct the evolved mean-square radius operator by starting from the initial form

$$R^2 = \frac{1}{A^2}\sum_{i=1}^{A}(\vec{r}_i - \vec{R}_{\text{cm}})^2\,, \quad \vec{R}_{\text{cm}} = \frac{1}{A}\sum_{i=1}^{A}\vec{r}_i\,. \tag{5.27}$$

and using Eq. (5.12) to derive the unitary transformation in the two–body system in terms of the singular vectors of the truncated SVD. The expectation value of the evolved R^2 is then computed in IMSRG(2).

Figure 5.17 illustrates the relationship between the rank of the SVD and root–mean–

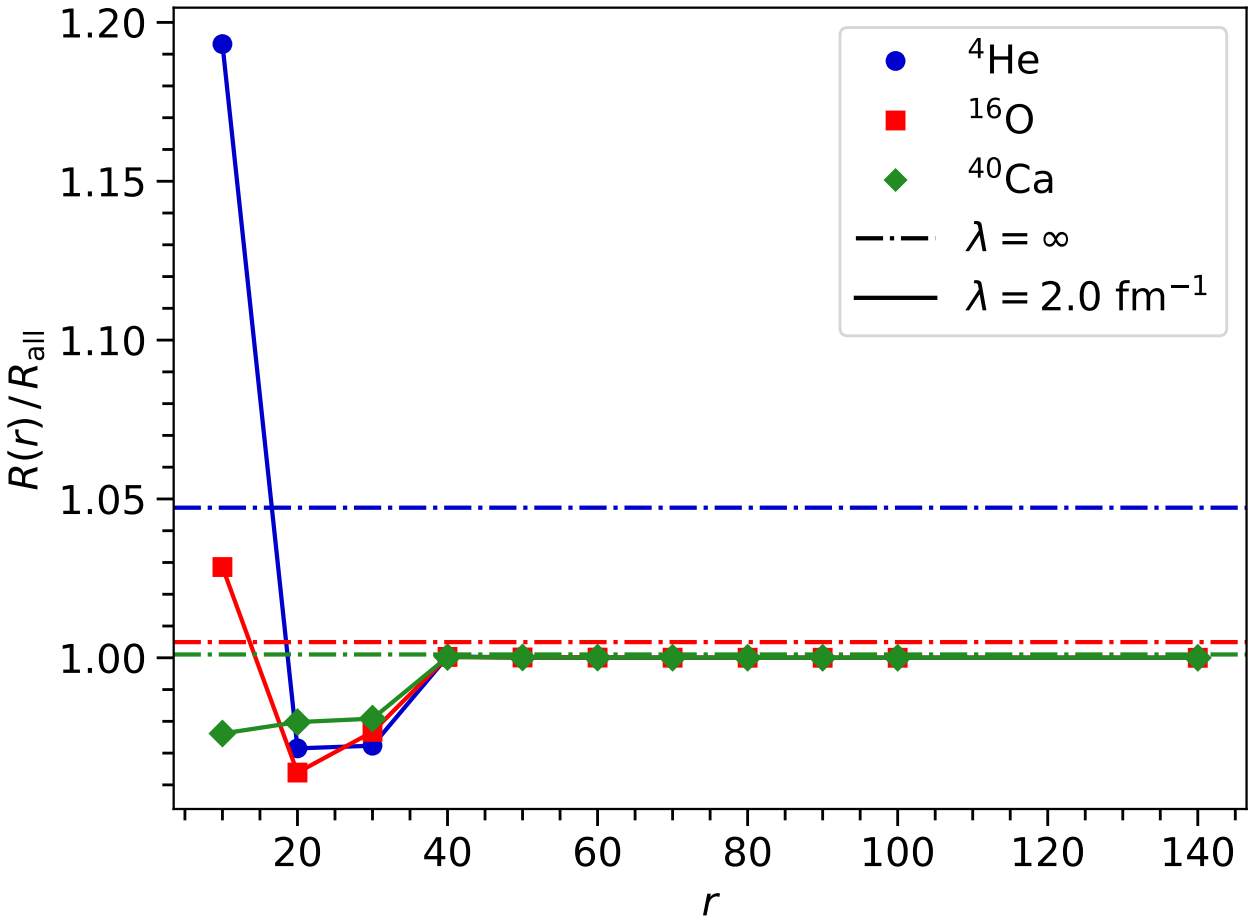

Figure 5.17: Accuracy of the SVD–SRG evolution for the root–mean–square radius of selected closed–shell nuclei: The curves show the ratio R/R_{all} as a function of the rank r, where R_{all} is obtained from a conventional matrix–based SRG evolution. The results for the bare operator are shown for comparison (dash–dotted lines). All calculations were performed with the EM1.8/2.0 interaction, using the IMSRG(2) truncation, $e_{\text{emax}} = 8, E_{3\text{max}} = 14$ and $\hbar\omega = 20$ MeV (cf. Figure 5.16).

square radii $R \equiv \sqrt{\langle R^2 \rangle}$ of $^4He, ^{16}O$ and ^{40}Ca in the IMSRG(2). As in the case of the ground-state energy energy, a rank of 30 to 40 is adequate to achieve an accurate reconstruction of the unitary transformation. We also include the radii obtained with the unevolved R^2 operator for comparison, which vary by about 5%, 0.5% and 0.1% in ^4He,^{16}O and ^{40}Ca, respectively. Since the SRG evolution aims for physics at high–momentum or short–range, its impact on a long–ranged operator like R^2 is weak and negligible when compared to other sources of uncertainty at present.

We conclude our discussion by stating although R^2 is undoubtedly one of the simplest observables to examine besides the energy, we anticipate no problems in using the factorized unitary transformation for more complicated operators, like in applications for electroweak transitions [26, 78, 110]. The reason is that ultimately, $U(s)$ is entirely determined by the characteristics of the Hamiltonian.

5.6 Conclusions and Directions for Future Research

In this chapter, we used the SVD to perform principal-component analyses of nucleon-nucleon interactions, using the chiral N^3LO interaction by Entem and Machleidt [22] and the Argonne V18 interaction [109] as representative examples. Our findings demonstrated that the EM interaction can be easily represented by a low–rank model that is constructed by truncating the SVD based on the magnitude of the singular values. Conversely, the AV18 interaction proved to be a much more challenging case because of its local nature and the resulting structure in momentum space, as well as its high implicit resolution scale.

We have merged the SVD and SRG techniques and demonstrated that the low–rank representation can be effectively evolved to lower resolution scales. However, the efficiency of this approach compared to traditional SRG depends on the rank of the original interaction. While the evolution of two-nucleon interactions using SRG is a well–established process, the next step is to extend these techniques to three-nucleon forces, where much more substantial efficiency improvements can be achieved — this will be the subject of Chapter 6.

We have carried the factorized representation of NN interactions through the various stages of the many-body theory workflows, and identified challenges, in particular when switching from the intrinsic/center-of-mass frame to the laboratory frame. At the final

stage, however, we resorted to reconstructing the input matrix elements from the factors, since formulating many–body methods capable of exploiting thes factorization more directly is a highly challenging task — we will come back to this issue in Chapter 7.

While our primacy focus lies in the aforementioned developments, there are additional interesting directions for future research:

1. In light of the adverse impact of the Coulomb interaction on the achievable rank compression in pp channels, it is worth exploring alternative treatments of V_C for addressing this issue.

2. The consistent ranks we observed across all partial waves of the interaction suggests that it may be a manifestation of a few essential operators projected into the different channels. Investigating such a possible connection may offer new ways of constructing compact operator bases for SRG and IMSRG flows.

3. The implementation of the Talmi-Moshinsky transformation on the SVD factors demonstrated how embedding an operator in larger product Hilbert spaces artifically increases the rank of its matrix representations through redundant copies. Given that many–body Hilbert spaces themselves possess a product structure, tensor representations appear to be a particularly suitable candidate for efficiently handling the physical information encoded in an operator.

Chapter 6

SVD-SRG for Three-Nucleon Interactions

Nucleon–Nucleon interactions alone are insufficient to accurately describe low–energy states in light nuclei, hence we are forced to include at least three–body ($3N$) interactions in our calculations (and in the worst case, even higher many-body forces, although we expect them to only matter in systems with large A or infinite matter, if at all, as discussed in Sections 2.4). The computational cost and memory requirements for handling $3N$ forces are substantial, we will explore their factorization and the development of an SVD-SRG for $3N$ interactions in this chapter.

6.1 Three-Body Basis States

We will begin by focusing on the fundamental basis set, which pertains to the eigenstates of the harmonic oscillator (HO). These eigenstates are established in relation to the Jacobi coordinates, which serve the purpose of untangling the motion involving the relative positioning from that of the overall center-of-mass movement. This disentanglement is povital as it grants us a direct avenue to explore the inherent structural characteristics of the nucleus under scrutiny. It is worth noting that there exist multiple options for selecting these coordinates. In the context of this study, we adopt the same definition as employed in pre-

vious references, namely references [16, 35, 71, 72], for the spatial Jacobi coordinates. This particular choice of coordinates has proven to be effective in previous research endeavors.

$$\begin{aligned}\vec{\xi}_0 &= \sqrt{\frac{1}{A}}[\vec{r}_1 + \vec{r}_2 + \cdots + \vec{r}_A] \\ \vec{\xi}_n &= \sqrt{\frac{n}{n+1}}\left[\frac{1}{n}(\vec{r}_1 + \vec{r}_2 + \cdots + \vec{r}_n) - \vec{r}_{n+1}\right]\end{aligned} \tag{6.1}$$

and for the Jacobi momenta

$$\begin{aligned}\vec{\pi}_0 &= \sqrt{\frac{1}{A}}\,[\vec{p}_1 + \vec{p}_2 \cdots + \vec{p}_A] \\ \vec{\pi}_n &= \sqrt{\frac{n}{n+1}}\left[\frac{1}{n}(\vec{p}_1 + \vec{p}_2 + \cdots + \vec{p}_n) - \vec{p}_{n+1}\right]\end{aligned} \tag{6.2}$$

where $\vec{r}_i$ and $\vec{p}_i$ represent the individual positional coordinates and momenta of the i-th particle, repectively, within the system. the coordinates ξ_0 and π_0 are directly related to the center-of-mass properties of the entire A-body configuration. Meanwile, the Jacobi coordinates ξ_n and π_n, where n ranges from 1 to $(A-1)$, capture the relative motion of the A-body system. These Jacobi coordinates are characterized by their role in describing the distance of the $(n-1)$-th particle from the center-of-mass of the first n particles, along with corresponding analogs from π_n

In Section 5.4, we previously encountered the HO basis states for the intrinsic frame in a two-nucleon system, which are given by

$$|N_{\rm cm} L_{\rm cm} M_{L_{\rm cm}}\rangle \bigotimes |N_1; (L_1 S_1) J_1 M_{J_1}; T_1 M_{T_1}\rangle_a \,. \tag{6.3}$$

Here, the subscript "cm" identifies the quantum numbers of the center-of-mass state encoding the collective motion of the system as a whole, rather than the individual particles within it.

The quantum numbers N_1 and L_1 refer to the radial and orbital angular momentum, of an oscillator state in the first Jacobi coordinate. S_1, T_1 and M_{T_1} denote the spin and isospin quantum numbers, as usual, and the angular momentum of the relative two-nucleon state and its projection are denoted as J_1 and M_{J_1}, respectively. We use the subscript a in (6.3) to indicate that the state describing the two-nucleon (sub)system has been antisymmetrized. This implies that its quantum numbers satisfy the condition $(-1)^{L_1+S_1+T_1} = 1$.

Generalizing (6.3) to the three-body system, we introduce the basis states (see Ref. [16, 35] for a detailed discussion)

$$|N_{\rm cm}L_{\rm cm}\rangle \bigotimes |N_1N_2;[(L_1S_1)J_1,(L_2\frac{1}{2})J_2]J_{12};(T_1\frac{1}{2})T_{12}\rangle_{a_1} \,. \tag{6.4}$$

Let us unpack the structure of these states in detail:

- N_2 and L_2 are the radial and orbital angular momentum quantum numbers associated with the second Jacobi coordinate.

- Based on the radial and orbital angular momentum quantum numbers, we can see that the total HO energy of (6.4) is given by $E = E_{\rm cm} + E_{12}$, where $E_{\rm cm} = 2N_{\rm cm} + L_{\rm cm}$ represents the center-of-mass contribution and E_{12} corresponds to the relative HO energy given by $E_{12} = (2N_1 + L_1) + (2N_2 + L_2)$.

- The total relative angular momenta associated with the two coordinates, J_1 and J_2, are coupled to J_{12}. Since the interactions are rotationally invariant, we drop the angular momentum projection quantum numbers for brevity.

- The third nucleon adds additional spin and isospin degrees of freedom to (6.4), but it is clear that we must always have $S_2 = \frac{1}{2}$ and $T_2 = \frac{1}{2}$, and we indicate so explicitly. The

total isospin of the three-nucleon state is obtained by coupling $T_1 = 0, 1$ and T_2, which means that we can have $T_{12} = \frac{1}{2}, \frac{3}{2}$.

- The subscript a_1 specifically indicates that this state is only *partially antisymmetric*, namely with respect to the exchange of the first two nucleons that are associated with the first Jacobi coordinate.

The partially antisymmetric three-body basis is introduced because we need to embed the evolving two-body interaction into the three-body system in order to track the induced interactions discussed in Section 2.4.

Of course, we eventually must antisymmetrize the three-body states completely if we want to obtain physical results in few- and many-body calculations. The most practical approach is to work with the antisymmetrizer $\mathcal{A}$: We can represent $\mathcal{A}$ in the partially antisymmetric Jacobi-HO basis (as given in 6.4) and diagonalize the corresponding matrix to obtain the eigenstates of this operator [16, 35, 74].

We see that the antisymmetrizer is block-diagonal in the Jacobi-HO basis, as briefly mentioned in Chapter 5. Specifically, the energy E_{12}, angular momentum J_{12}, and isospin T_{12} are conserved quantum numbers. As a result, the diagonalization can be performed separately for each $(E_{12}J_{12}T_{12})$-block. The fully antisymmetric eigenstates are associated with the eigenvalue (-1), and these eigenstates can be presented as a linear combination of the partially antisymmetric states (6.4) in each block.

Since the antisymmetrization does not affect the rotational symmetry of the states 6.4, the $3N$ interaction will be diagonal in the angular momentum J_{12}, and it is also diagonal in parity $(-1)^\pi = (-1)^{L_1+L_2}$. In many-body calculation, one usually also ignores isospin-breaking effects in the $3N$ interaction because they are small compared to the various sources

uncertainty. Thus, the $3N$ interaction will also be diagonal in isospin T_{12}. Overall, we can separate the $3N$ interaction matrix into antisymmetrized $J^{\pi}_{12}T_{12}$ blocks.

The introduction of the antisymmetric Jacobi-HO basis also has a practical benefit, because the number of interaction matrix elements is reduced compared to the partially antisymmetric basis. This reduction is about an order of magnitude. As a final remark, we note that the antisymmetrization procedure discussed here cannot be directly applied in arbitrary basis sets, because the antisymmetrizer [35] will not be block-diagonal in general and other approaches for ensuring the proper antisymmetry are needed [34, 35, 74, 104]. A particularly important example is the $3N$ partial wave momentum basis [34, 35].

6.2 SRG Evolution in the Three-Nucleon System

Let us now discuss the SRG evolution for a three-nucleon system.

One thing we can use is that what we called the "α" basis[1] is partially antisymmetric under exchanging particles 1 and 2, but has no symmetry with respect to exchanges involving particle 3. So, whenever we encounter something like V_{23} [2], we can always rewrite it in terms of V_{12} [3]:

$$V_{23} = P_{13}V_{12}P_{13} = P_{12}P_{23}P_{12}V_{12}P_{12}P_{23}P_{12} \tag{6.5a}$$

$$V_{13} = P_{23}V_{12}P_{23} \tag{6.5b}$$

Here we used $P_{13} = P_{12}P_{23}P_{12}$, where P_{13} is a permutation operator that permutes two

[1] α basis is introduced to represent the second term in Eq. 6.4, where $\alpha_{12} = \{L_1, S_1, J_1, L_2, J_2, J_{12}, T_1, T_{12}\}$

[2] V_{23} designates the potential between the particle 2 and particle 3.

[3] V_{12} designates the potential between the particle 1 and particle 2.

particles indicated (to swap particles 1 and 3 in $|abc\rangle$ is equivalent to swap particle 1 and 2, $|bac\rangle$, then swap 2 and 3, $|bca\rangle$, then 1 and 2 again, $|cba\rangle$). Note that the permutation operators commute with their corresponding 2-body potentials, like $[P_{12}, V_{12}] = 0$, etc.

Due to antisymmetry, the matrix elements of V_{23} and V_{13} are the same:

$$\langle\alpha'|\, V_{23}\,|\alpha\rangle = \langle\alpha'|\, P_{12}P_{23}V_{12}P_{23}P_{12}\,|\alpha\rangle = (-1)^2\,\langle\alpha'|\, P_{23}V_{12}P_{23}\,|\alpha\rangle \tag{6.6}$$

The same works for the kinetic energy. The P_{23} operator is unitary and Hermitian, and thus $P_{23}^2 = 1$. This implies that its only eigenvalues are +1 and −1. The CFPs are the eigenvectors to eigenvalue -1. so we can write P_{23} in spectral representation:

$$P_{23} = 1 - 2\sum_{E,i} |\mathrm{CFP}, E, i\rangle\,\langle \mathrm{CFP}, E, i| \tag{6.7}$$

What we have to do is to find the ODE for the 3-body part (induced + initial). The general flow equation will also contain 2-body parts with a spectator, which have to be separated out. The flow equation is now given by [34, 35, 49]

$$\begin{aligned}\frac{dH}{ds} &= [\eta, H] = [[T, V], H] \\ &= [[T_{12} + T_{13} + T_{23}, V_{12} + V_{13} + V_{23} + V_{123}], T_{12} + T_{13} + T_{23} + V_{12} + V_{13} + V_{23} + V_{123}]\end{aligned} \tag{6.8}$$

Using that we keep T constant, we split the flow equation into four classes of terms:

$$\frac{dV}{ds} \equiv \frac{dV_a}{ds} + \frac{dV_b}{ds} + \frac{dV_c}{ds} + \frac{dV_d}{ds} \tag{6.9}$$

with

$$\frac{dV_a}{ds} \equiv [[T_{12}, V_{12}], T_{12} + V_{12}] + [[T_{13}, V_{13}], T_{13} + V_{13}] + [[T_{23}, V_{23}], T_{23} + V_{23}], \tag{6.10a}$$

$$\begin{aligned}\frac{dV_b}{ds} \equiv &[[T_{12}, V_{12}], T_{13} + V_{13}] + [[T_{12}, V_{12}], T_{23} + V_{23}] \\ &+ [[T_{13}, V_{13}], T_{12} + V_{12}] + [[T_{13}, V_{13}], T_{23} + V_{23}] \\ &+ [[T_{23}, V_{23}], T_{12} + V_{12}] + [[T_{23}, V_{23}], T_{13} + V_{13}],\end{aligned} \tag{6.10b}$$

$$\begin{aligned}\frac{dV_c}{ds} \equiv &[[T_{12}, V_{13} + V_{23}], T_{12} + T_{13} + T_{23} + V_{12} + V_{13} + V_{23}] \\ &+ [[T_{13}, V_{12} + V_{23}], T_{12} + T_{13} + T_{23} + V_{12} + V_{13} + V_{23}] \\ &+ [[T_{23}, V_{12} + V_{13}], T_{12} + T_{13} + T_{23} + V_{12} + V_{13} + V_{23}],\end{aligned} \tag{6.10c}$$

and

$$\begin{aligned}\frac{dV_d}{ds} \equiv &[[T_{12} + T_{13} + T_{23}, V_{123}], T_{12} + T_{13} + T_{23} + V_{12} + V_{13} + V_{23}] \\ &+ [[T_{12} + T_{13} + T_{23}, V_{123}], V_{123}] \\ &+ [[T_{12} + T_{13} + T_{23}, V_{12} + V_{13} + V_{23}], V_{123}]\end{aligned} \tag{6.10d}$$

The first class, $\frac{dV_a}{ds}$, are merely the evolution of the pairwise two-nucleon interactions embedded in the presence of a spectator nucleon. The contributions $\frac{dV_b}{ds}$ and $\frac{dV_c}{ds}$ are given in terms of two-body operators, but all three nucleons are actively affected by the evolution, hence they generate induced three-body forces from the two-body interactions. Finally, $\frac{dV_d}{ds}$ is the induced force due to the flowing three-body interaction.

We can simplify the expression: In the end, we are only interested in the antisymmetric matrix elements $\langle E', i'| \frac{dV}{ds} |E, i\rangle = \langle E', i'| \mathcal{A} \frac{dV}{ds} |E, i\rangle$, where $\mathcal{A}$ is the antisymmetrizer. For

any permutation operator P_{ij}, we have $\mathcal{A}P_{ij} = P_{ij}\mathcal{A} = -\mathcal{A}$, so whenever we can pull out one of the permutations, we can replace it by a minus sign.

Applying this idea to the first class of terms, Eq. (6.10a), we get

$$\begin{aligned}\mathcal{A}\frac{dV_a}{ds}\mathcal{A} &= \mathcal{A}[[T_{12},V_{12}],T_{12}+V_{12}]\mathcal{A} + \mathcal{A}P_{23}[[T_{12},V_{12}],T_{12}+V_{12}]P_{23}\mathcal{A} + \\ &\quad \mathcal{A}P_{13}[[T_{23},V_{23}],T_{23}+V_{23}]P_{13}\mathcal{A} \\ &= 3\mathcal{A}[[T_{12},V_{12}],T_{12}+V_{12}] \end{aligned} \tag{6.11}$$

This is just the two-body derivative embedded into three-body space, which is subtracted out.

For $\frac{dV_b}{ds}$ (Eq. (6.10b)), we obtain

$$\begin{aligned}\mathcal{A}\frac{dV_b}{ds}\mathcal{A} &= \mathcal{A}[[T_{12},V_{12}],T_{13}+V_{13}]\mathcal{A} + \mathcal{A}[[T_{12},V_{12}],T_{23}+V_{23}]\mathcal{A} + \\ &\quad \mathcal{A}[[T_{13},V_{13}],T_{12}+V_{12}]\mathcal{A} + \mathcal{A}[[T_{13},V_{13}],T_{23}+V_{23}]\mathcal{A} + \\ &\quad \mathcal{A}[[T_{23},V_{23}],T_{12}+V_{12}]\mathcal{A} + \mathcal{A}[[T_{23},V_{23}],T_{13}+V_{13}]\mathcal{A} \\ &= \mathcal{A}P_{12}[[T_{12},V_{12}],T_{23}+V_{23}]P_{12}\mathcal{A} + \mathcal{A}[[T_{12},V_{12}],T_{23}+V_{23}]\mathcal{A} + \\ &\quad \mathcal{A}P_{12}[[T_{23},V_{23}],T_{12}+V_{12}]P_{12}\mathcal{A} + \mathcal{A}P_{23}[[T_{12},V_{12}],T_{23}+V_{23}]P_{23}\mathcal{A} + \\ &\quad \mathcal{A}[[T_{23},V_{23}],T_{12}+V_{12}]\mathcal{A} + \mathcal{A}P_{23}[[T_{23},V_{23}],T_{12}+V_{12}]P_{23}\mathcal{A} + \\ &= 3\mathcal{A}[[T_{12},V_{12}],T_{23}+V_{23}]\mathcal{A} + 3\mathcal{A}[[T_{23},V_{23}],T_{12}+V_{12}]\mathcal{A} \\ &= 3\mathcal{A}[[T_{12},V_{12}],T_{23}+V_{23}]\mathcal{A} + 3\mathcal{A}P_{12}P_{13}P_{23}[[T_{12},V_{12}],T_{23}+V_{23}]P_{23}P_{13}P_{12}\mathcal{A} \\ &= 6\mathcal{A}[[T_{12},V_{12}],T_{23}+V_{23}]\mathcal{A}\,, \end{aligned} \tag{6.12}$$

and $\frac{dV_c}{ds}$ (Eq. (6.10c)) can be simplified to

$$\begin{aligned}
\mathcal{A}\frac{dV_c}{ds}\mathcal{A} &= \mathcal{A}[[T_{12}, V_{13}+V_{23}], T_{12}+T_{13}+T_{23}+V_{12}+V_{13}+V_{23}]\mathcal{A} + \\
&\quad \mathcal{A}[[T_{13}, V_{12}+V_{23}], T_{12}+T_{13}+T_{23}+V_{12}+V_{13}+V_{23}]\mathcal{A} + \\
&\quad \mathcal{A}[[T_{23}, V_{12}+V_{13}], T_{12}+T_{13}+T_{23}+V_{12}+V_{13}+V_{23}]\mathcal{A} \\
&= [\mathcal{A}[T_{12}, V_{13}+V_{23}]\mathcal{A}, \mathcal{A}(T_{12}+T_{13}+T_{23}+V_{12}+V_{13}+V_{23})\mathcal{A}] + \\
&\quad [\mathcal{A}[T_{13}, V_{12}+V_{23}]\mathcal{A}, \mathcal{A}(T_{12}+T_{13}+T_{23}+V_{12}+V_{13}+V_{23})\mathcal{A}] + \\
&\quad [\mathcal{A}[T_{23}, V_{12}+V_{13}]\mathcal{A}, \mathcal{A}(T_{12}+T_{13}+T_{23}+V_{12}+V_{13}+V_{23})\mathcal{A}] \\
&= [\mathcal{A}[T_{12}, V_{13}+V_{23}]\mathcal{A}, 3\mathcal{A}(T_{12}+V_{12})\mathcal{A}] + \\
&\quad [\mathcal{A}[P_{23}T_{13}P_{23}, P_{23}(V_{12}+V_{23})P_{23}]\mathcal{A}, 3\mathcal{A}(T_{12}+V_{12})\mathcal{A}] + \\
&\quad [\mathcal{A}[P_{13}T_{23}P_{13}, P_{13}(V_{12}+V_{13})P_{13}]\mathcal{A}, 3\mathcal{A}(T_{12}+V_{12})\mathcal{A}] \\
&= 3[\mathcal{A}[T_{12}, V_{13}+V_{23}]\mathcal{A}, 3\mathcal{A}(T_{12}+V_{12})\mathcal{A}] \\
&= 9[\mathcal{A}[T_{12}, P_{12}V_{13}P_{12}+V_{23}]\mathcal{A}, \mathcal{A}(T_{12}+V_{12})\mathcal{A}] \\
&= 18[\mathcal{A}[T_{12}, V_{23}]\mathcal{A}, \mathcal{A}(T_{12}+V_{12})\mathcal{A}]
\end{aligned} \tag{6.13}$$

Here, we have used that for any unitary operator U we can write

$$\begin{aligned}
[B, C] &= BC - CB = UU^\dagger BUU^\dagger CUU^\dagger - UU^\dagger CUU^\dagger BUU^\dagger \\
&= U[U^\dagger BU, U^\dagger CU]U^\dagger
\end{aligned} \tag{6.14}$$

and for any idempotent operator $A^2 = A$ that commutes with C, we have

$$A[B, C]A = ABCA - ACBA = ABA^2CA - ACA^2BA$$

$$= [ABA, ACA] \tag{6.15}$$

Finally, the terms involving the flowing three-body interaction (Eq. (6.10d)) can be rewritten as

$$\begin{aligned}
\mathcal{A}\frac{dV_d}{ds}\mathcal{A} &= \mathcal{A}[[T_{12}+T_{13}+T_{23}, V_{123}], T_{12}+T_{13}+T_{23}+V_{12}+V_{13}+V_{23}]\mathcal{A} + \\
&\quad \mathcal{A}[[T_{12}+T_{13}+T_{23}, V_{123}], V_{123}]\mathcal{A} + \\
&\quad \mathcal{A}[[T_{12}+T_{13}+T_{23}, V_{12}+V_{13}+V_{23}], V_{123}]\mathcal{A} \\
&= 3[[\mathcal{A}T_{12}\mathcal{A}, V_{123}], 3\mathcal{A}(T_{12}+V_{12})\mathcal{A}+V_{123}] + \\
&\quad 9[[\mathcal{A}T_{12}\mathcal{A}, \mathcal{A}V_{12}\mathcal{A}], V_{123}]
\end{aligned} \tag{6.16}$$

Since $\frac{dV_a}{ds}$ is the flowing two-nucleon part, the rest must be the ODE for the genuine three-body terms. Together, we have

$$\frac{dV_{12}}{ds} = [[T_{12}, V_{12}], T_{12}+V_{12}] \tag{6.17}$$

$$\begin{aligned}
\frac{dV_{123}}{ds} &= 6\mathcal{A}[[T_{12}, V_{12}], T_{23}+V_{23}]\mathcal{A} + 18[\mathcal{A}[T_{12}, V_{23}]\mathcal{A}, \mathcal{A}(T_{12}+V_{12})\mathcal{A}] + \\
&\quad 3[[\mathcal{A}T_{12}\mathcal{A}, V_{123}], 3\mathcal{A}(T_{12}+V_{12})\mathcal{A}+V_{123}] + 9[[\mathcal{A}T_{12}\mathcal{A}, \mathcal{A}V_{12}\mathcal{A}], V_{123}]
\end{aligned} \tag{6.18}$$

In the initial phase, we solve a set of ODEs within the context of the two-body interaction in two-body space. Subsequently, these two-body interactions are integrated into the broader three-body interaction space, and they undergo a joint evolutionary process. Upon the end of this evolution, we perform a subtraction operation, effectively removing the evolved two-body interactions from the three-body interaction space. This procedure yields two critical outcomes: the evolved three-body interactions and the induced three-body interactions

together, which encapsulate the intricate dynamics of the system under investigation.

The SRG evolution is performed in the antisymmetric Jacobi-HO basis, which is truncated based on the maximum total energy. The symmetries of the Hamiltonian allow for separate evolution of each $J_{12}^{\pi}T_{12}$ block, enabling numerical feasibility for large model spaces. To begin the evolution, a matrix representation of the initial Hamiltonian is computed, After the evolution, the matrix elements of the Hamiltonian consist of a combination of two-body and three-body term, as discussed above. These terms need to be separated as they scale differently in many-body calculations.

6.3 Singular Value Decomposition of 3N Interactions

In this particular section, we shall undertake an in-depth examination into the singular value spectrum of interactions involving three-body, as well as two-body interaction in 3B space.

Initially, we proceed by employing Singular Value Decomposition (SVD) to decompose pure three-body interactions, By utilizing this technique, we aim to investigate the spectra associated with these interactions at various resolution scales. The Fig. 6.1 unveils the singular spectra of a three-body interaction at various differential partial waves, as indicated in the sub-captions. This interaction is an N2LO (Next-to-Next-to-Leading Order) three-nucleon interaction with a cutoff value of $\lambda = 2.0$ fm^{-1}. It has been tailored to complement an SRG-evolved Entem-Machleidt N3LO nucleon-nucleon interaction, where the SRG cutoff is also set to $\lambda = 2.0$ fm^{-1}, corresponding to $s = 0.0625$ fm^4($\lambda = s^{-1/4}$). The last three numbers in the subtitles indicate the specific partial wave, denoted as twoT = 1 (representing $T = 1/2$), twoJ = 1 (representing $J = 1/2$), and $\pi = 0$ (parity even). The first and second numbers

indicate T and J, respectively, where twoT can only be 1 or 3, and twoJ can take values such as 1,3,5,7,9,11,13,15, and so on. Within the figure, a red circular dot is employed to denote that the cumulative sum of singular values accounts for 99% of the total singular values. Additionally, a red square dot is used to indicate that the cumulative sum of singular values represents 99.9% of the total singular values.

The plots also provide information regarding the dimensionality of the block that we are working with corresponding to specific quantum numbers. It is evident from the graphs that the singular values exhibit a rapid decay, reaching magnitudes below 10^{-10} within approximately one-fourth of the total dimensions. This observation implies that only a few hundred singular components are necessary to capture the essential physics of the system.

While we have previously observed a low-rank structure within the realm of pure three-body interactions, our investigation into the evolutionary dynamics of the combined two-body and three-body interactions tells a different story. Figure 6.2 vividly illustrate that, upon evolving these interactions, the resultant induced interaction does not exhibit the characteristic low-rank structure.

In light of this compelling empirical evidence, we are compelled to draw the conclusions that the amalgamation of the SVD technique with the SRG approach (SVD-SRG) proves to be impractical and ineffective when applied within the intricate landscape of the three-body interaction dynamics. This observation, while challenging, serves as a valuable contribution to the ongoing discourse in nuclear physics. It underscores the inherent complexities and nuances associated with three-body interactions, illuminating the limitations of the SVD-SRG methodology within this specific domain.

In our quest for continued advancement, it becomes evident that an avenue worthy of exploration lies in the incorporation of tensor factorization methodologies, such as the ap-

plication of non-linear Principal Component Analysis (PCA). This direction of investigation holds the potential to refine our analytical techniques and deepen our comprehension of intricate nuclear systems, particularly within the context of three-body interactions. By venturing into the domain of non-linear PCA and assessing its applicability, we aspire to unearth fresh insights and sophisticated computational tools.

6.4 Randomized SVD on Three-Body Interaction

As previously demonstrated, our research has successfully identified the low-rank structure inherent in t pure three-body interactions. Building upon this foundation, the current section delves into a comprehensive exploration of the algorithms associated with Randomized SVD (RSVD). Within this framework, we apply these algorithms to the rand-reduce matrices, thereby offering an in-depth investigation into the efficacy and potential of these computational techniques. This includes a rigorous examination of their time complexity, as well as a meticulous analysis of the associated errors.

Figure 6.3 presents a comprehensive analysis of computational running times for the regular SVD method applied to low-rank matrices of varying dimensions. To establish a meaningful comparison with RSVD, we adopted a truncation criterion wherein 99.9% of the total singular values were retained, while maintaining a fixed oversampling parameter of 10. By systematically varying the oversampling parameter within the RSVD framework, our observations revealed a striking advantage of RSVD over regular SVD, showcasing 2 orders of magnitude improvement in computational efficiency. Furthermore, our investigation into different power schemes (q) highlighted that, when appropriately chosen (as depicted in Fig 6.3a), the choice of q has a negligible impact on running time, further reinforcing the

computational benefits of RSVD. In Fig 6.3b, we delve deeper into RSVD variants, with RSVD-3, denoted as Algorithm 2, emerging as the front runner in terms of computational performance. This nuanced analysis underscores the potential of RSVD methodologies to significantly enhance computational efficiency numerical simulations and modeling in this field.

Figure 6.4 presents a comparative analysis between the conventional SVD and a range of RSVD variants. The primacy focus of this comparison lies in the examination of deviations within the singular value spectra tails. It is worth noting that all the RSVD variants consistently yield error percentage below the 1% threshold, as evident in Fig. 6.4a. In Fig. 6.4b we explore results obtained through the application of Algorithm 1, which displays distinct tail behaviors compared to the previous approach, yet maintains a comparable level of error percentage. Fig. 6.4c introduces a novel RSVD variant, one that imposes constraints solely on the symmetry of the matrices. Following QR decomposition, this variant projects the low-rank matrix into the basis defined by the unitary matrix Q and subsequently conducts SVD decomposition within this Q-space. Notably, this algorithm exhibits substantial digression when compared to other RSVD variants. However, Fig. 6.4d demonstrates that with the implementation of an approximate power scheme, this digression can be further mitigated, showcasing the potential for enhanced accuracy in our numerical simulations.

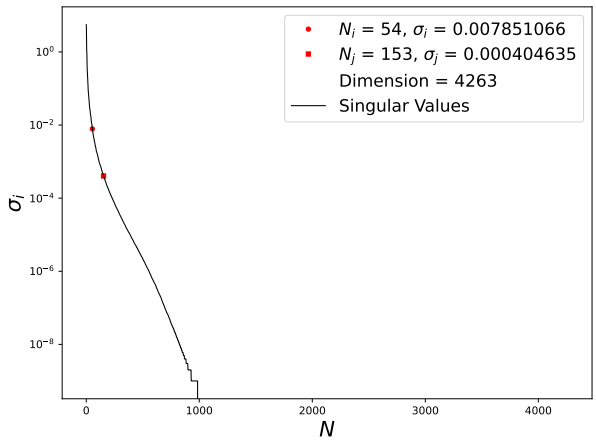

(a) $T = \frac{1}{2}$ $J = \frac{1}{2}$ $\pi = 0$

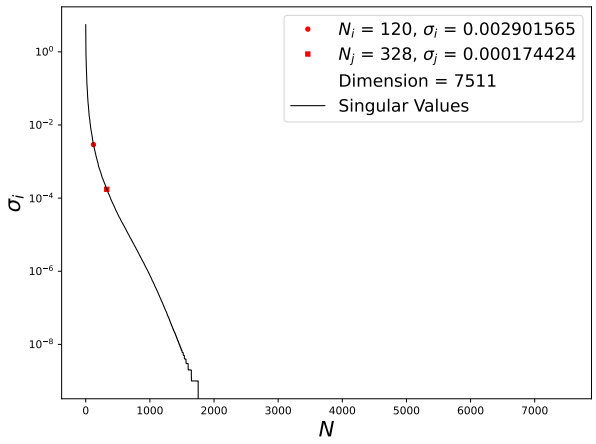

(b) $T = \frac{1}{2}$ $J = \frac{3}{2}$ $\pi = 1$

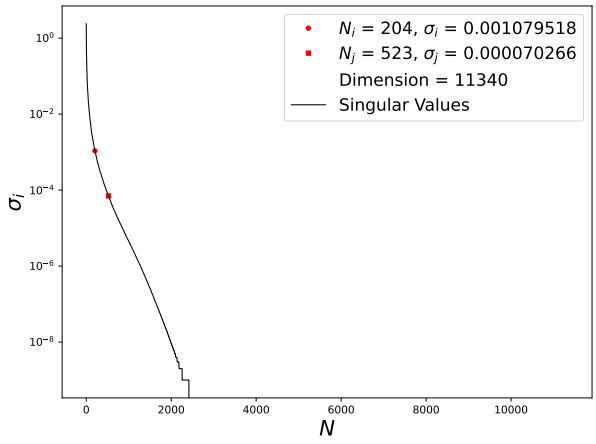

(c) $T = \frac{1}{2}$ $J = \frac{5}{2}$ $\pi = 0$

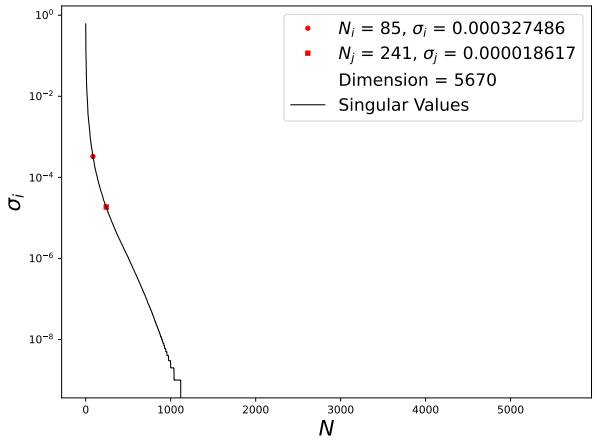

(d) $T = \frac{3}{2}$ $J = \frac{5}{2}$ $\pi = 0$

Figure 6.1: Singular value spectra of 3B interaction at differential partial waves indicated in sub-captions. This is an N2LO three-nucleon interaction with cutoff $\lambda = 2.0$ fm^{-1} that has been fit to accompany an SRG-evolved Entem-Machleidt N3LO nucleon-nucleon interaction (SRG $\lambda = 2.0$ fm^{-1}, so that $s = 0.0625$ fm^4($\lambda = s^{-1/4}$). The last three numbers indicated in the subtitles are the specific partial wave – should be twoT = 1 (i.e., $T = \frac{1}{2}$), twoJ = 1 (i.e., $J = \frac{1}{2}$), $\Pi = 0$ (parity even). The first and second number are T and J, respectively: twoT can only be 1 or 3, twoJ can be 1,3,5,7,9,11,13,15,...The red circular dot signifies that the cumulative sum of singular values constitutes 99% of the total singular values, whereas the red square dot indicates the cumulative sum of singular values constitutes 99.9%

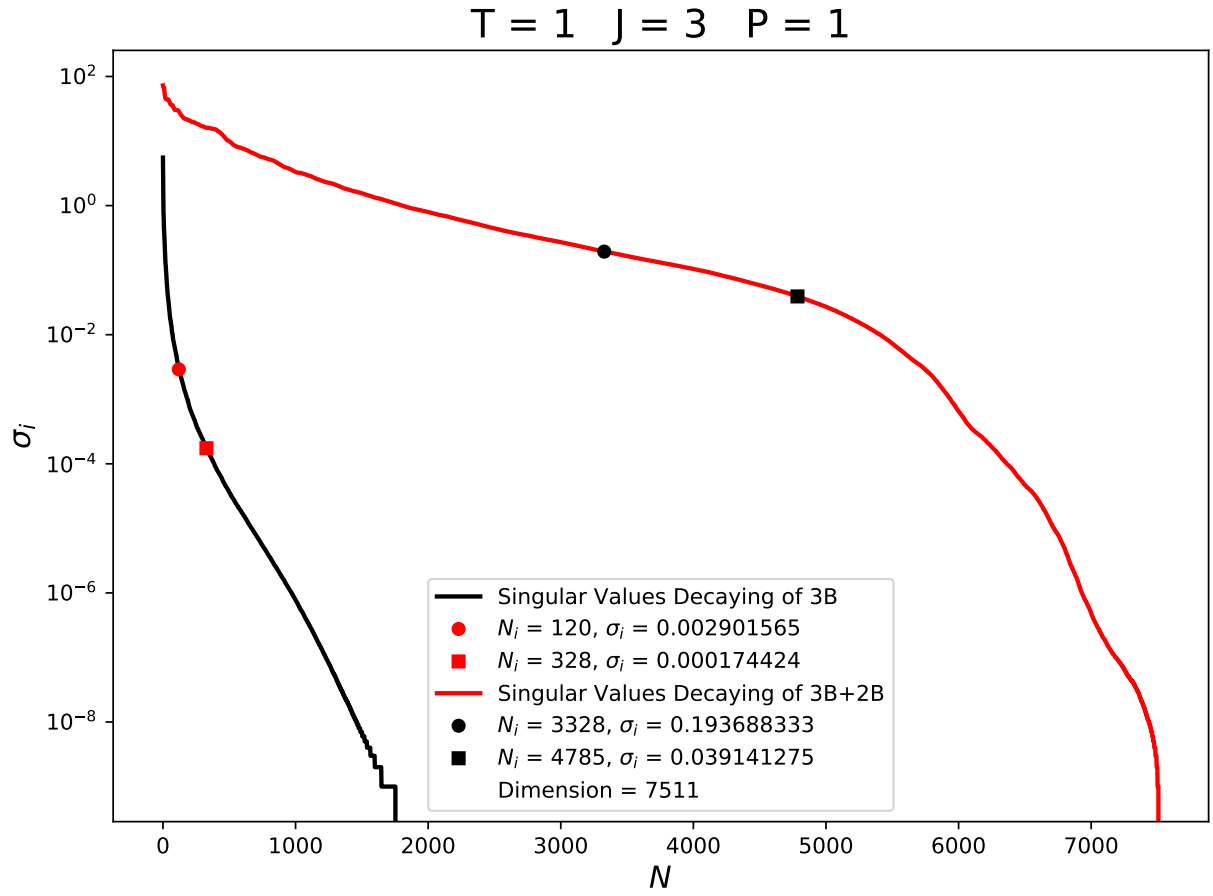

Figure 6.2: The Singular spectra of 3B interaction at $s = 0$ in black and evolved $s = \infty$ 2B+3B interactions in red.

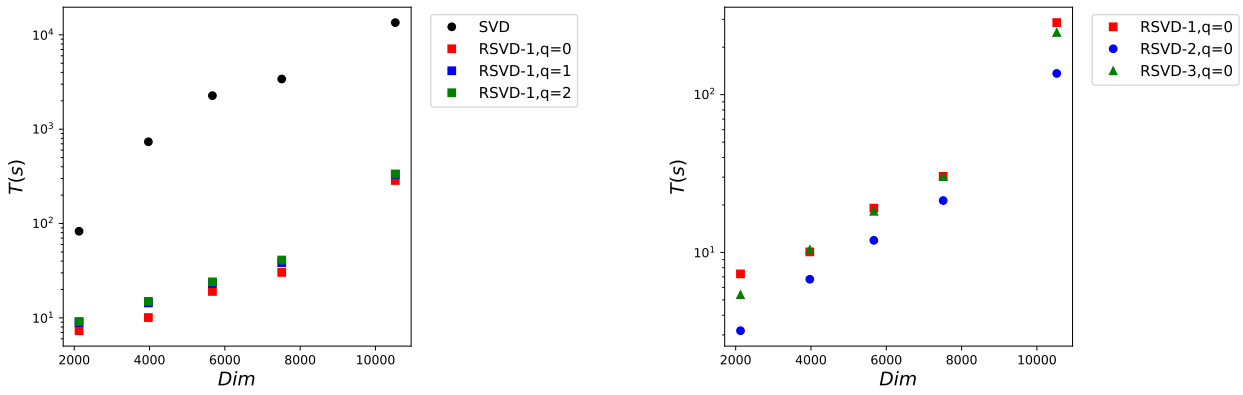

(a) (b)

Figure 6.3: *Panel (a)*: "Comparing Running Times - Regular SVD vs. RSVD with Varied Power Scheme". *Panel (b)*: "Exploring RSVD Variants - Run-Time Analysis"

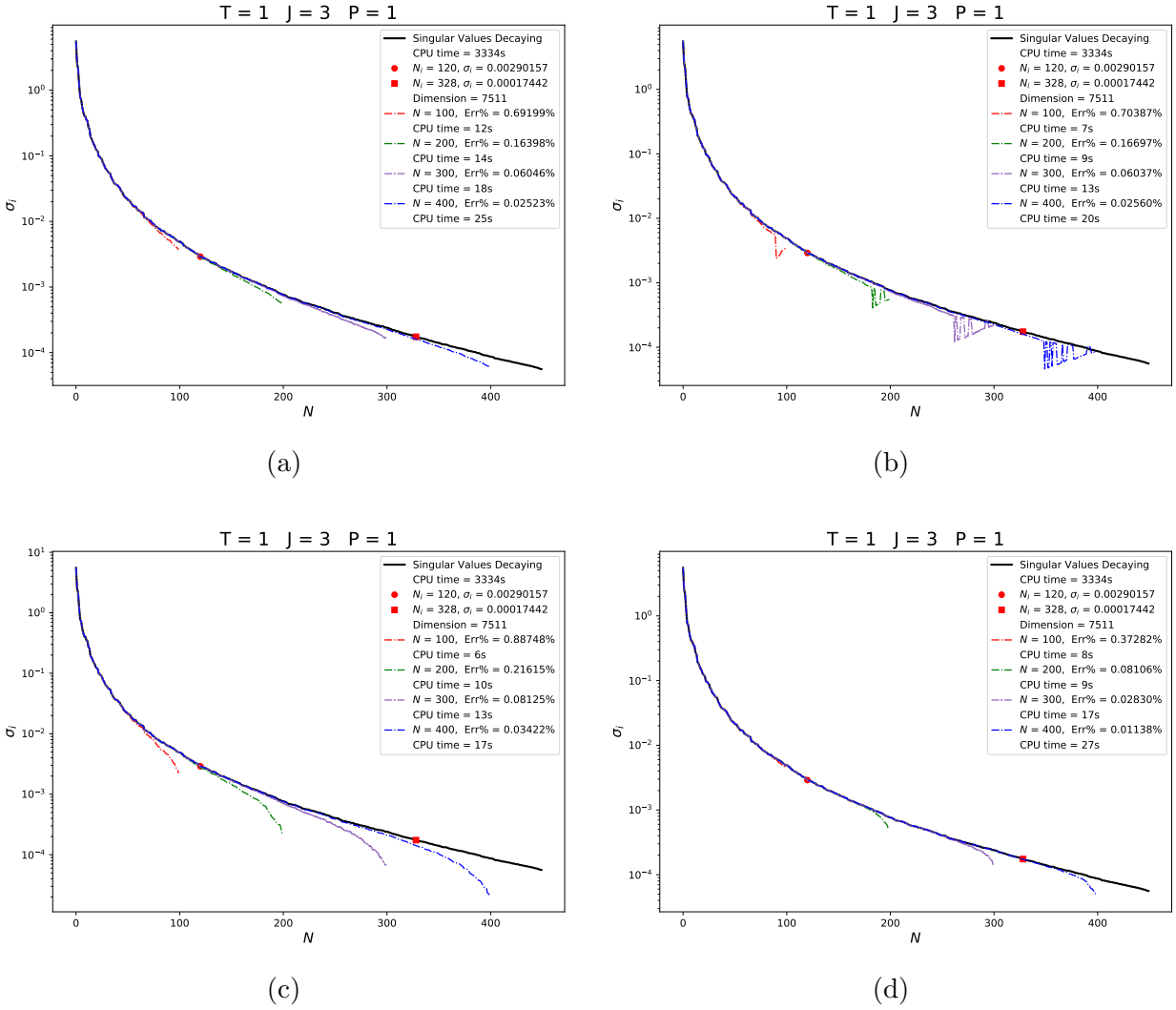

Figure 6.4: Comparative Analysis of SVD Techniques: Regular SVD vs. Randomized SVD and Variants

Part III

Factorization in Many-Body Systems

Chapter 7

SVD and IMSRG

We now move from the few-body systems discussed in the previous chapters to many-body systems, with the goal of applying SVDs to factorize the quantities that appear in the IMSRG flow equations. In Section 5.4, we saw that it is not straightforward to "transfer" low-rank structures that were identified in the intrinsic frame to the laboratory frame, because embeddings of the factors into larger Hilbert spaces and basis transformations can inflate the rank of the interaction again. However, there are compelling reasons for exploring SVDs of the normal-ordered Hamiltonian and generator appearing in the IMSRG: As discussed in Section 3.4, the latter has the structure

$$\eta = \sum_{ai} \eta_{ai} \{a_a^\dagger a_i\} + \frac{1}{4} \sum_{abij} \eta_{abij} \{a_a^\dagger a_b^\dagger a_j a_i\} - \text{H.c.}\,, \tag{7.1}$$

and the $N_p^2 \times N_h^2$ matrix η_{abij} is flat and wide in realistic applications because $N_h \ll N_p$. Thus, its numerical rank should satisfy $k \leq N_h^2$, which is much smaller than the naive rank N^4 for normal-ordered two-body operators.

In the present chapter, we reformulate the IMSRG(2) (cf. Section 3) in a way that allows us exploit a rank reduction, if revealed through SVD. In subsequent chapters, we will apply this new formulation to a schematic model, as well as infinite nuclear matter. We note that similar ideas have been explored in Coupled Cluster calculations in quantum chemistry; after

first attempts in Refs. [44, 53], significant progress has been made in just the last couple of years, in parallel to the work described here [45, 46, 61, 62, 77].

7.1 The IMSRG(2) in Rank-Reduced Form

To start, we assume that

$$f_{pq} = \sum_{\mu\nu} u_p^\mu f^{\mu\nu} u_q^\nu \tag{7.2}$$

$$\Gamma_{pqrs} = \sum_{\alpha\beta} U_{pq}^\alpha \Gamma^{\alpha\beta} U_{rs}^\beta \tag{7.3}$$

where f and Γ are the one- and two-body parts of the normal-ordered Hamiltonian, as discussed in Section 1.3.8. The coefficients u_p^μ and U_{pq}^α are the elements of basis transformations in the one- and two-body spaces — the idea is that these coefficients could be obtained as singular vectors of a truncated SVD of f, Γ or other appropriate one- and two-body operators. Denoting the ranges of the transformed one- and two-body bases by d_μ and D_α, respectively, we ideally would like that

$$d_\mu \ll N\,, \quad D_\alpha \ll N^2\,, \tag{7.4}$$

so that there will be a significant compression in comparison to the working basis. While we have touched upon the tensor structure of our operators and many-body wave functions in Chapters 1 and 5, we work with matrix representations in the following — the exploration of tensor representations will be left for future work.

In analogy to Eqs. (7.2) and (7.3), we define the transformed generator as

$$\eta_{pq} = \sum_{\mu\nu} u_p^\mu \eta^{\mu\nu} u_q^\nu \,, \tag{7.5}$$

$$\eta_{pqrs} = \sum_{\alpha\beta} U_{pq}^\alpha \eta^{\alpha\beta} U_{rs}^\beta \,. \tag{7.6}$$

In our first attempt at merging SVD and IMSRG, we take a slightly different approach than in the SVD-SRG: Instead of evolving both the singular value matrices and left and right singular vectors, We assume that the transformations u_p^μ and U_{pq}^α defined by the singular vectors remain fixed, and we evolve the (reduced) quantities $f^{\mu\nu}$ and $\Gamma^{\alpha\beta}$.

Let us now consider the zero-body flow equation (3.9) and plug in Eqs. (7.2)–(7.6). First, we split the equation into two contributions:

$$\frac{dE}{ds} = \underbrace{\sum_{pq} (n_p - n_q) \eta_{pq} f_{qp}}_{①} + \underbrace{\frac{1}{2} \sum_{pqrs} \eta_{pqrs} \Gamma_{rspq} n_r n_s \bar{n}_p \bar{n}_q}_{②} \,. \tag{7.7}$$

Defining the transformed density matrix

$$\rho^{\mu\nu} \equiv \sum_p u_p^\mu n_p u_p^\nu \,, \tag{7.8}$$

and assuming that the reduced basis u^μ is still orthonormalized (which would be true for a basis of singular vectors),

$$\sum_p u_p^\mu u_p^\nu = \delta^{\mu\nu} \,, \tag{7.9}$$

we obtain

$$
\begin{aligned}
① &= \sum_{ab}(n_a - n_b)\sum_{\mu\nu}\sum_{\mu'\nu'} u_a^{\mu}\eta^{\mu\nu}u_b^{\nu}u_b^{\mu'}f^{\mu'\nu'}u_a^{\nu'} \\
&= \sum_{\mu\nu}\sum_{\mu'\nu'}\left(\sum_a u_a^{\mu}n_a u_a^{\nu'}\sum_b u_b^{\nu}u_b^{\mu'} - \sum_b u_b^{\nu}n_b u_b^{\mu'}\sum_a u_a^{\mu}u_a^{\nu'}\right)\eta^{\mu\nu}f^{\mu'\nu'} \\
&= \sum_{\mu\nu}\sum_{\mu'\nu'}\left(\rho^{\mu\nu'}\delta^{\nu\mu'} - \rho^{\nu\mu'}\delta^{\mu\nu'}\right)\eta^{\mu\nu}f^{\mu'\nu'} \\
&= \sum_{\mu\mu'\nu'}\left(\eta^{\mu\mu'}f^{\mu'\nu'}\rho^{\nu'\mu}\right) - \sum_{\mu\mu'\nu}\left(\rho^{\nu\mu'}f^{\mu'\mu}\eta^{\mu\nu}\right) \\
&= \sum_{\lambda\mu\nu}\left(\eta^{\lambda\mu}f^{\mu\nu} - f^{\lambda\mu}\eta^{\mu\nu}\right)\rho^{\nu\lambda} \\
&= \mathrm{Tr}\left(\eta f\rho - f\eta\rho\right) .
\end{aligned}
\tag{7.10}
$$

Similarly, we can introduce the two-body particle and hole density matrices

$$
\mathrm{P}^{\alpha\beta} \equiv \sum_{pq} U_{pq}^{\alpha}n_p n_q U_{pq}^{\beta} = \sum_{ij} U_{ij}^{\alpha}n_i n_j U_{ij}^{\beta} , \tag{7.11a}
$$

$$
\overline{\mathrm{P}}^{\alpha\beta} \equiv \sum_{pq} U_{pq}^{\alpha}\bar{n}_p\bar{n}_q U_{pq}^{\beta} = \sum_{ab} U_{ab}^{\alpha}\bar{n}_a\bar{n}_b U_{ab}^{\beta} , \tag{7.11b}
$$

and rewrite the second term as

$$
\begin{aligned}
② &= \frac{1}{2}\sum_{pqrs}\sum_{\alpha\beta}\sum_{\alpha'\beta'} U_{pq}^{\alpha}\eta^{\alpha\beta}U_{rs}^{\beta}U_{rs}^{\alpha'}\Gamma^{\alpha'\beta'}U_{pq}^{\beta'}n_p n_q\bar{n}_r\bar{n}_s \\
&= \frac{1}{2}\sum_{\alpha\beta}\sum_{\alpha'\beta'}\left(\sum_{pq}U_{pq}^{\alpha}n_p n_q U_{pq}^{\beta'}\right)\left(\sum_{rs}U_{rs}^{\beta}\bar{n}_r\bar{n}_s U_{rs}^{\alpha'}\right)\eta^{\alpha\beta}\Gamma^{\alpha'\beta'} \\
&= \frac{1}{2}\sum_{\alpha\beta}\sum_{\alpha'\beta'}\eta^{\alpha\beta}\overline{\mathrm{P}}^{\beta\alpha'}\Gamma^{\alpha'\beta'}\mathrm{P}^{\beta'\alpha} \\
&= \frac{1}{2}\,\mathrm{Tr}\left(\eta\overline{\mathrm{P}}\Gamma\mathrm{P}\right) .
\end{aligned}
\tag{7.12}
$$

Putting the two terms together, we obtain

$$\frac{dE}{ds} = \mathrm{Tr}\left(\eta f \rho - f \eta \rho\right) + \frac{1}{2}\,\mathrm{Tr}\left(\eta \overline{\mathrm{P}} \Gamma \mathrm{P}\right)\,, \tag{7.13}$$

and we see that the flow of the energy can be easily computed in terms of the reduced quantities. Ultimately, this is not surprising, because the RHS of the flow equation is given in terms of traces that must be invariant under basis changes.

Next, we consider the one-body flow equation (3.11). First, we note that

$$n_a - n_b = n_a - n_b + n_a n_b - n_a n_b = n_a(1 - n_b) - n_b(1 - n_a) = n_a \bar{n}_b - \bar{n}_a n_b\,, \tag{7.14}$$

hence we can rewrite the flow equation as

$$\begin{aligned}\frac{df_{pq}}{ds} = &\sum_r (1 + P_{pq})\eta_{pr} f_{rq} + \sum_{rs} (n_r \bar{n}_s - \bar{n}_r n_s)(\eta_{rs}\Gamma_{sprq} - f_{rs}\eta_{sprq}) \\ &+ \frac{1}{2}\sum_{rst}(n_r n_s \bar{n}_t + \bar{n}_r \bar{n}_s n_t)(1 + P_{pq})\eta_{tprs}\Gamma_{rstq}\,.\end{aligned} \tag{7.15}$$

Applying the transformation to the reduced representation and summing, we obtain

$$\begin{aligned}\frac{df^{\mu\nu}}{ds} = &\underbrace{\sum_{pq} u_p^\mu \left(\sum_r (1 + P_{pq})\eta_{pr} f_{rq}\right) u_q^\nu}_{①} + \underbrace{\sum_{pq} u_p^\mu \left(\sum_{rs} (n_r \bar{n}_s - \bar{n}_r n_s)(\eta_{rs}\Gamma_{sprq} - f_{rs}\eta_{sprq})\right) u_q^\nu}_{②} \\ &+ \underbrace{\sum_{pq} u_p^\mu \left(\frac{1}{2}\sum_{rst}(n_r n_s \bar{n}_t + \bar{n}_r \bar{n}_s n_t)(1 + P_{pq})\eta_{tprs}\Gamma_{rstq}\right) u_q^\nu}_{③} \\ = &\,(\eta f - f\eta)^{\mu\nu} + \left(\Upsilon\overline{\Upsilon}\eta\Gamma - \overline{\Upsilon}\Upsilon\eta\Gamma - \Upsilon\overline{\Upsilon}f\eta + \overline{\Upsilon}\Upsilon f\eta\right)^{\mu\nu} \\ &+ \frac{1}{2}\left(\mathrm{P}\overline{\Xi}\eta\Gamma - \mathrm{P}\Xi\eta\Gamma + \mathrm{P}\overline{\Xi}'\eta\Gamma - \mathrm{P}\Xi'\eta\Gamma\right)^{\mu\nu}\end{aligned} \tag{7.16}$$

where we have defined

$$\Upsilon^{\mu\nu\alpha} \equiv \sum_{pq} u_p^\mu u_q^\nu U_{qp}^\alpha n_q \,, \qquad \overline{\Upsilon}^{\mu\nu\alpha} \equiv \sum_{pq} u_p^\mu u_q^\nu U_{qp} \bar{n}_q \,, \tag{7.17}$$

and

$$\Xi^{\alpha\beta\mu\nu} \equiv \sum_{pqr} U_{rp}^\alpha U_{rq}^\beta u_p^\mu u_q^\nu n_r \,, \qquad \overline{\Xi}^{\alpha\beta\mu\nu} \equiv \sum_{pqr} U_{rp}^\alpha U_{rq}^\beta u_p^\mu u_q^\nu \bar{n}_r \,. \tag{7.18}$$

In detail,

$$\begin{aligned}
① &= \sum_{ij} u_i^\mu \sum_a \left(\eta_{ia} f_{aj} + \eta_{ja} f_{ai}\right) u_j^\nu \\
&= \sum_{ij} \sum_a \sum_{\mu'\nu'} \sum_{\mu''\nu''} u_i^\mu \left(u_i^{\mu'} \eta^{\mu'\nu'} u_a^{\nu'} u_a^{\mu''} f^{\mu''\nu''} u_j^{\nu''} + u_j^{\mu'} \eta^{\mu'\nu'} u_a^{\nu'} u_a^{\mu''} f^{\mu''\nu''} u_i^{\nu''} \right) u_j^\nu \\
&= \sum_{ij} \sum_{\mu'\nu'} \sum_{\mu''\nu''} u_i^\mu \left(u_i^{\mu'} \eta^{\mu'\nu'} \delta^{\nu'\mu''} f^{\mu''\nu''} u_j^{\nu''} + u_j^{\mu'} \eta^{\mu'\nu'} \delta^{\nu'\mu''} f^{\mu''\nu''} u_i^{\nu''} \right) u_j^\nu \\
&= \sum_{ij} \sum_{\mu'\nu'\nu''} u_i^\mu \left(u_i^{\mu'} \eta^{\mu'\nu'} f^{\nu'\nu''} u_j^{\nu''} + u_j^{\mu'} \eta^{\mu'\nu'} f^{\nu'\nu''} u_i^{\nu''} \right) u_j^\nu \\
&= \sum_{ij} \sum_{\mu'\nu''} u_i^\mu \left(u_i^{\mu'} (\eta f)^{\mu'\nu''} u_j^{\nu''} + u_j^{\mu'} (\eta f)^{\mu'\nu''} u_i^{\nu''} \right) u_j^\nu \\
&= \sum_{\mu'\nu''} \delta^{\mu\mu'} (\eta f)^{\mu'\nu''} \delta^{\nu''\nu} + \delta^{\nu\mu'} (\eta f)^{\mu'\nu''} \delta^{\nu''\mu} \\
&= (\eta f)^{\mu\nu} + (\eta f)^{\nu\mu} \\
&= (\eta f - f\eta)^{\mu\nu}
\end{aligned} \tag{7.19}$$

where in the last equality, we used the symmetry of f and antisymmetry of η,

$$② = \sum_{ij} u_i^\mu \left(\sum_{ab} (n_a - n_b)(\eta_{ab} \Gamma_{biaj} - f_{ab} \eta_{biaj}) \right) u_j^\nu$$

$$
\begin{aligned}
&= \sum_{ij}\sum_{ab}(n_a - n_b)\left(u_i^{\mu}u_j^{\nu}u_a^{\mu'}\eta^{\mu'\nu'}u_b^{\nu'}U_{bi}^{\alpha}\Gamma^{\alpha\beta}U_{aj}^{\beta} - u_i^{\mu}u_j^{\nu}u_a^{\mu''}f^{\mu''\nu''}u_b^{\nu''}U_{bi}^{\alpha'}\eta^{\alpha'\beta'}U_{aj}^{\beta'}\right)\\
&= \sum_{\mu'\nu'}\sum_{\alpha\beta}\left(\Upsilon^{\nu\mu'\beta}\overline{\Upsilon}^{\mu\nu'\alpha} - \overline{\Upsilon}^{\nu\mu'\beta}\Upsilon^{\mu\nu'\alpha}\right)\eta^{\mu'\nu'}\Gamma^{\alpha\beta} -\\
&\qquad\qquad \sum_{\mu''\nu''}\sum_{\alpha'\beta'}\left(\Upsilon^{\nu\mu''\beta'}\overline{\Upsilon}^{\mu\nu''\alpha'} - \overline{\Upsilon}^{\nu\mu''\beta'}\Upsilon^{\mu\nu''\alpha'}\right)f^{\mu''\nu''}\eta^{\alpha'\beta'}\\
&= \sum_{\mu'\nu'}\sum_{\alpha\beta}\left(\Upsilon^{\nu\mu''\beta'}\overline{\Upsilon}^{\mu\nu''\alpha'} - \overline{\Upsilon}^{\nu\mu''\beta'}\Upsilon^{\mu\nu''\alpha'}\right)\left(\eta^{\mu'\nu'}\Gamma^{\alpha\beta} - f^{\mu'\nu'}\eta^{\alpha\beta}\right)\\
&= \left(\Upsilon\overline{\Upsilon}\eta\Gamma\right)^{\mu\nu} - \left(\overline{\Upsilon}\Upsilon\eta\Gamma\right)^{\mu\nu} - \left(\Upsilon\overline{\Upsilon}f\eta\right)^{\mu\nu} + \left(\overline{\Upsilon}\Upsilon f\eta\right)^{\mu\nu}\,, \qquad (7.20)
\end{aligned}
$$

and

$$
\begin{aligned}
③ &= \sum_{ij}u_i^{\mu}\left(\frac{1}{2}\sum_{abc}(n_an_b\bar{n}_c + \bar{n}_a\bar{n}_bn_c)(1+P_{ij})\eta_{ciab}\Gamma_{abcj}\right)u_j^{\nu}\\
&= \frac{1}{2}\sum_{ij}\sum_{abc}(n_an_b\bar{n}_c + \bar{n}_a\bar{n}_bn_c)\left(U_{ci}^{\alpha}U_{ab}^{\beta}U_{ab}^{\alpha'}U_{cj}^{\beta'}u_i^{\mu}u_j^{\nu}\right)\left(1+P_{ij}\right)\eta^{\alpha\beta}\Gamma^{\alpha'\beta'}\\
&= \frac{1}{2}\left(\sum_{ab}U_{ab}^{\beta}U_{ab}^{\alpha'}n_an_b\sum_{ijc}U_{ci}^{\alpha}U_{cj}^{\beta'}u_i^{\mu}u_j^{\nu}\bar{n}_c - \sum_{ab}U_{ab}^{\beta}U_{ab}^{\alpha'}\bar{n}_a\bar{n}_b\sum_{ijc}U_{ci}^{\alpha}U_{cj}^{\beta'}u_i^{\mu}u_j^{\nu}n_c\right)\times\\
&\qquad\qquad \left(1+P_{ij}\right)\eta^{\alpha\beta}\Gamma^{\alpha'\beta'}\\
&= \frac{1}{2}\left(\mathrm{P}^{\beta\alpha'}\Xi^{\alpha\mu\beta'\nu} - \overline{\mathrm{P}}^{\beta\alpha'}\Xi^{\alpha\mu\beta'\nu} + \mathrm{P}^{\beta\alpha'}\overline{\Xi}^{\alpha\nu\beta'\mu} - \overline{\mathrm{P}}^{\beta\alpha'}\Xi^{\alpha\nu\beta'\mu}\right)\eta^{\alpha\beta}\Gamma^{\alpha'\beta'}\\
&= \frac{1}{2}\left(\mathrm{P}\overline{\Xi}\eta\Gamma - \mathrm{P}\Xi\eta\Gamma + \mathrm{P}\overline{\Xi}'\eta\Gamma - \mathrm{P}\Xi'\eta\Gamma\right)^{\mu\nu} \qquad (7.21)
\end{aligned}
$$

with P and $\overline{\mathrm{P}}$ as defined in 7.11.

For the two-body flow equation (3.14),

$$
\begin{aligned}
\frac{d\Gamma_{ijkl}}{ds} &= \sum_{\alpha\beta} U^{\alpha}_{ij} \frac{d\Gamma^{\alpha\beta}}{ds} U^{\beta}_{kl} \\
&= \sum_{a} (1-P_{ij})(\eta_{ia}\Gamma_{ajkl} - f_{ia}\eta_{ajkl}) - (1-P_{kl})(\eta_{ak}\Gamma_{ijal} - f_{ak}\eta_{ijal}) \\
&\quad + \frac{1}{2}\sum_{ab}(1-n_a-n_b)(\eta_{ijab}\Gamma_{abkl} - \Gamma_{ijab}\eta_{abkl}) \\
&\quad + \sum_{ab}(n_a-n_b)(1-P_{ij})(1-P_{kl})\eta_{aibk}\Gamma_{bjal} \\
\frac{d\Gamma^{\alpha\beta}}{ds} &= \sum_{ijkl} \underbrace{U^{\alpha}_{ij}\sum_{a}\{(1-P_{ij})(\eta_{ia}\Gamma_{ajkl} - f_{ia}\eta_{ajkl}) - (1-P_{kl})(\eta_{ak}\Gamma_{ijal} - f_{ak}\eta_{ijal})\}U^{\beta}_{kl}}_{①} \\
&\quad + \underbrace{\frac{1}{2}\sum_{ijkl} U^{\alpha}_{ij}\sum_{ab}(1-n_a-n_b)(\eta_{ijab}\Gamma_{abkl} - \Gamma_{ijab}\eta_{abkl})U^{\beta}_{kl}}_{②} \\
&\quad + \underbrace{\sum_{ijkl} U^{\alpha}_{ij}\sum_{ab}(n_a-n_b)(1-P_{ij})(1-P_{kl})\eta_{aibk}\Gamma_{bjal}U^{\beta}_{kl}}_{③} \\
&= \left(\widetilde{\Upsilon}\eta\Gamma - \widetilde{\Upsilon} f\eta - \widetilde{\Upsilon}'\eta\Gamma - \widetilde{\Upsilon}' f\eta\right)^{\alpha\beta} + \frac{1}{2}\left(\eta(\overline{\mathrm{P}}-\mathrm{P})\Gamma - \Gamma(\overline{\mathrm{P}}-\mathrm{P})\eta\right)^{\alpha\beta} + dfadfasfa
\end{aligned}
\tag{7.22}
$$

where we have

$$
① = \sum_{ijkl}\sum_{a}\left(1-P_{ij}\right)\left(U^{\alpha}_{ij}U^{\beta}_{kl}u^{\mu}_{i}u^{\nu}_{a}U^{\alpha'}_{aj}U^{\beta'}_{kl}\right)\left(\eta^{\mu\nu}\Gamma^{\alpha'\beta'} - f^{\mu\nu}\eta^{\alpha'\beta'}\right) \tag{7.23}
$$

$$
- \sum_{ijkl}\sum_{a}\left(1-P_{kl}\right)\left(U^{\alpha}_{ij}U^{\beta}_{kl}u^{\mu}_{a}u^{\nu}_{k}U^{\alpha'}_{ij}U^{\beta'}_{al}\right)\left(\eta^{\mu\nu}\Gamma^{\alpha'\beta'} - f^{\mu\nu}\eta^{\alpha'\beta'}\right) \tag{7.24}
$$

$$
= \widetilde{\Upsilon}^{\nu\alpha'\mu\alpha}\left(\eta^{\mu\nu}\Gamma^{\alpha'\beta} - f^{\mu\nu}\eta^{\alpha'\beta}\right) - \widetilde{\Upsilon}^{\mu\beta'\nu\beta}\left(\eta^{\mu\nu}\Gamma^{\alpha\beta'} - f^{\mu\nu}\eta^{\alpha\beta'}\right) \tag{7.25}
$$

$$
= \left(\widetilde{\Upsilon}\eta\Gamma - \widetilde{\Upsilon} f\eta - \widetilde{\Upsilon}'\eta\Gamma - \widetilde{\Upsilon}' f\eta\right)^{\alpha\beta} \tag{7.26}
$$

where Υ is defined as

$$\widetilde{\Upsilon} = \sum_{ijkl} \sum_{a} U_{ij} u_i u_a U_{aj} \tag{7.27}$$

$\widetilde{\Upsilon}$ demonstrates marginal dissimilarity compared to the definition of Υ or $\overline{\Upsilon}$ provided in equation (7.17), where the former encompasses summation across the entirety of the single-particle axis. $\widetilde{\Upsilon}$ and $\widetilde{\Upsilon}'$ exhibit permutation-induced variation in indices.

$$\begin{aligned}
② &= \frac{1}{2} \sum_{ijkl} U_{ij}^{\alpha} \sum_{ab} (\bar{n}_a \bar{n}_b - n_a n_b) \left(U_{ij}^{\alpha'} U_{ab}^{\beta'} U_{ab}^{\alpha''} U_{kl}^{\beta''} - U_{ij}^{\alpha''} U_{ab}^{\beta''} U_{ab}^{\alpha'} U_{kl}^{\beta'} \right) U_{kl}^{\beta} \eta^{\alpha'\beta'} \Gamma^{\alpha''\beta''} \\
&= \frac{1}{2} \left(\delta^{\alpha\alpha'} \delta^{\beta\beta''} \overline{\mathrm{P}}^{\beta'\alpha''} - \delta^{\alpha\alpha''} \delta^{\beta\beta'} \overline{\mathrm{P}}^{\beta'\alpha''} - \delta^{\alpha\alpha'} \delta^{\beta\beta''} \mathrm{P}^{\beta'\alpha''} + \delta^{\alpha\alpha''} \delta^{\beta\beta'} \mathrm{P}^{\beta'\alpha''} \right) \eta^{\alpha'\beta'} \Gamma^{\alpha''\beta''} \\
&= \frac{1}{2} \left(\eta^{\alpha\beta'} \left(\overline{\mathrm{P}}^{\beta'\alpha''} - \mathrm{P}^{\beta'\alpha''} \right) \Gamma^{\alpha''\beta} - \Gamma^{\alpha\beta''} \left(\overline{\mathrm{P}}^{\beta'\alpha''} - \mathrm{P}^{\beta'\alpha''} \right) \eta^{\alpha'\beta} \right) \\
&= \frac{1}{2} \left(\eta(\overline{\mathrm{P}} - \mathrm{P})\Gamma - \Gamma(\overline{\mathrm{P}} - \mathrm{P})\eta \right)^{\alpha\beta}
\end{aligned} \tag{7.28}$$

where the final term involves a straightforward matrix multiplication operation.

$$\begin{aligned}
③ &= \sum_{ijkl} U_{ij}^{\alpha} U_{kl}^{\beta} \sum_{ab} (n_a \bar{n}_b - \bar{n}_a n_b) \left(1 - P_{ij} - P_{kl} + P_{ij} P_{kl} \right) \sum_{\alpha'\beta'} \sum_{\alpha''\beta''} U_{ai}^{\alpha'} U_{bk}^{\beta'} U_{bj}^{\alpha''} U_{al}^{\beta''} \\
&= \sum_{ijkl} U_{ij}^{\alpha} U_{kl}^{\beta} \left(1 - P_{ij} - P_{kl} + P_{ij} P_{kl} \right) \sum_{\alpha'\beta'} \sum_{\alpha''\beta''} \\
&\qquad \sum_{ab} \left[(U_{ai}^{\alpha'} U_{al}^{\beta''} n_a)(U_{bk}^{\beta'} U_{bj}^{\alpha''} \bar{n}_b) - (U_{ai}^{\alpha'} U_{al}^{\beta''} \bar{n}_a)(U_{bk}^{\beta'} U_{bj}^{\alpha''} n_b) \right] \eta^{\alpha'\beta'} \Gamma^{\alpha''\beta''} \\
&= \left(1 - P_{ij} - P_{kl} + P_{ij} P_{kl} \right) \sum_{\alpha'\beta'} \sum_{\alpha''\beta''} \sum_{ijkl} U_{ij}^{\alpha} U_{kl}^{\beta} \left(\mathrm{T}_{il}^{\alpha'\beta''} \overline{\mathrm{T}}_{kj}^{\beta'\alpha''} - \overline{\mathrm{T}}_{il}^{\alpha'\beta''} \mathrm{T}_{kj}^{\beta'\alpha''} \right) \eta^{\alpha'\beta'} \Gamma^{\alpha''\beta''} \\
&= \left(1 - P_{ij} - P_{kl} + P_{ij} P_{kl} \right) \sum_{ijkl} \sum_{\beta'\beta''} U_{ij}^{\alpha} U_{kl}^{\beta} \left((\mathrm{T}\eta)_{il}^{\beta''\beta'} (\overline{\mathrm{T}}\Gamma)_{kj}^{\beta''\beta'} - (\overline{\mathrm{T}}\eta)_{il}^{\beta''\beta'} (\mathrm{T}\Gamma)_{kj}^{\beta''\beta'} \right) \\
&= \left(1 - P_{ij} - P_{kl} + P_{ij} P_{kl} \right) \sum_{ijkl} U_{ij}^{\alpha} U_{kl}^{\beta} \left(\square_{ilkj} - \square_{kjil} \right)
\end{aligned} \tag{7.29}$$

$$\tag{7.30}$$

where we can choose to retain the indices (i, j, k, l) in the preceding expression at this intermediate stage, opting against further contraction. Subsequent contraction would exacerbate the computational intricacies involved. It is worth emphasizing that this particular term holds sifnificant importance in the context of the SVD-IMSRG development, which will be elaborated upon in the subsequent section. Here, we have formally defined

$$\square = \sum_{\beta\beta'} (\mathrm{T}\eta)^{\beta\beta'} (\overline{\mathrm{T}}\Gamma)^{\beta\beta''}, \qquad \mathrm{T}_{ij} = \sum_{i} U_a i U_a j n_a, \qquad \overline{\mathrm{T}}_{ij} = \sum_{i} U_{ai} U_{aj} \bar{n}_a \tag{7.31}$$

7.2 Computational Scaling

Let's briefly discuss the computational scaling of the SVD-IMSRG(2) approach compared with IMSRG(2) before delving into its implementation in the following section. During a single integration step, the zero-body flow equation (7.13) required $\mathcal{O}(r^4)$ compared to $\mathcal{O}(N^4)$ in IMSRG(2), where N indicates the size of the single particle basis and r scales as N, $r < N$ in rank-reduced space. The computational effort is dominated by the two-body flow equation (3.14), which naively required $\mathcal{O}(N^6)$ operations IMSRG(2). In the context of SVD-IMSRG(2), a notable achievement is the successful compression of the ladder term (7.28) from its original complexity of $\mathcal{O}(N^6)$ to $\mathcal{O}(r^6)$ using SVD. It is imperative to recognize that the intricacy in the particle-hole term (7.29) remains unaltered, thereby necessitating a comprehensive exploration of alternative contraction methodologies or diverse decomposition techniques to effectively tackle this aspect. Moreover, there arises a demand for the retention of specific matrices or tensors, essential for matrices/tensors precomputed and stored before the flow equations. Notably, the tonsorial representation of these flow equations introduces auxiliary tensors, thereby requiring their temporary storage to ensure

seamless implementation.

Chapter 8

SVD-IMSRG for Schematic Models

In the following section, we will explore the application of the SVD-IMSRG in a family of schematic models based on pairing and pair-breaking interactions. We will see that the enhanced computational scheme can lead to significant speedups compared to the conventional IMSRG approach, provided the pair-breaking interaction is weak.

8.1 The Schematic Models

8.1.1 The Pairing Model

The so-called pairing model Hamiltonian describes a quantum system of A fermions in a set of uniformly spaced energy levels, each having a spin degeneracy of two. The Hamiltonian is given by

$$H = \underbrace{\delta \sum_{p\sigma} (p-1) a^\dagger_{p\sigma} a_{p\sigma}}_{\equiv H_0} \underbrace{- \frac{1}{2} g \sum_{pq} a^\dagger_{p+} a^\dagger_{p-} a_{q-} a_{q+}}_{\equiv V} . \tag{8.1}$$

Here, p is the energy quantum number of a single-particle state, and σ denotes the spin projection. In the one-body operator H_0, the constant δ controls the spacing of the energy levels. V is a two-body interaction term with a coupling constant g, which describes the interactions of pairs of particles with the same energy but opposite spin projection.

As a concrete example, let us consider $A = 4$ particles in $N = 8$ single-particle states. Since

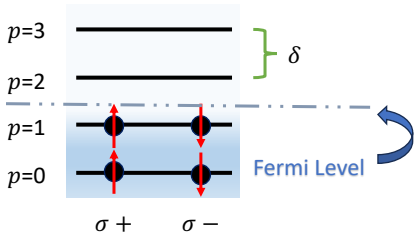

Figure 8.1: Illustration of the pairing model configuration with 8 single-particle states and 4 particles, the first two levels with shading represent hole states, while the above two levels depict particle states. The particles are arranged within their respective states, showcasing the pairing of particle in this quantum system.

H_0 is a diagonal one-body operator, we know that its eigenstates are Slater determinants (cf. Sec. 1.3.9) that correspond to all the possible ways in which we can distribute 4 particles into 8 levels — $\binom{8}{4} = 70$ in total. We can then use these states as a basis for our many-body Hilbert space. In Fig. 8.1, we illustrate the basis configuration corresponding to the ground state of H_0, with the lowest two energy levels occupied by pairs.

Upon further inspection, we note that H does conserve the total spin projection M_S: Since H_0 is diagonal, it merely counts whether a given single-particle state $|p, \sigma\rangle$ is occupied or not, and V only acts on pairs with spin projection 0, either counting them (for $p = q$) or scattering them to different energy ($p \neq q$). Thus, the Hamiltonian matrix consists of blocks with constant M_S (see Fig. 8.2). From Fig. 8.1 it is apparent that the possible values of M_S range from -2 (all 4 particles with in states with spin $-\frac{1}{2}$) to $+2$ (all 4 particles in states with spin $+\frac{1}{2}$). Since V only acts on pairs of nucleons, as explained above, the number of pairs N_P is an additional conserved quantity, so there will be sub-blocks with constant N_P within each M_S block. We can easily find their dimensions: For $M_S = \pm 2$, all four particles will be in different energy levels, and there will be no pairs. There is just one possible arrangement (since the fermions are undistinguishable), hence the dimension of these blocks is just 1. For $M_S = \pm 1$, we have need to have three particles with the same spin projection, and one with

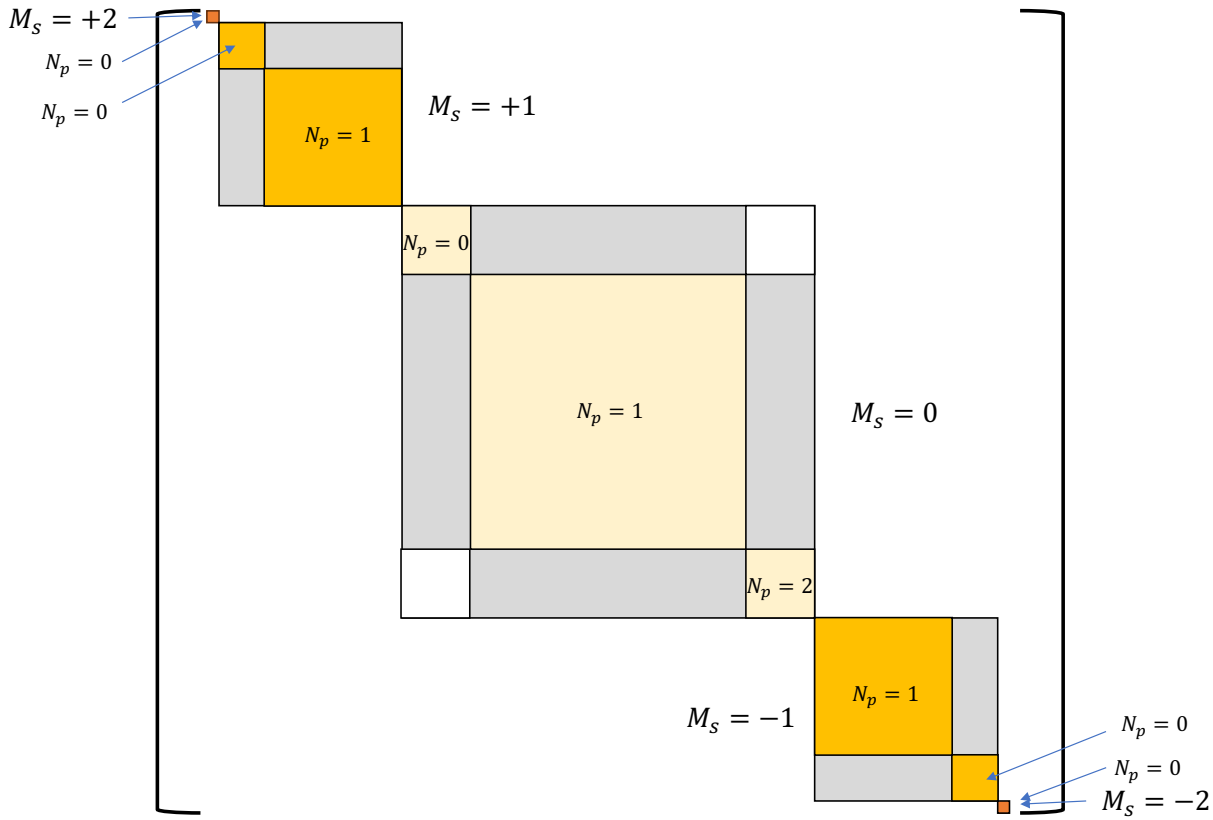

Figure 8.2: Illustration of the structure of the Hamiltonian matrix with M_s blocks in a 4-particle-8-state system, from -2 to 2. Revealing the Inner Symmetry of N_p-paired blocks.

the opposite projection. Thus, the total dimension of each of these blocks is

$$\binom{N_+}{3} \times \binom{N_-}{1} = \binom{N_+}{1} \times \binom{N_-}{3} = 4 \times 4 = 16\,.$$

Within these blocks, there are 12 states for which there is one pair, i.e., when one spin-up and one spin-down fermion have the same energy, and four states in which the single-particle energies are all distinct. Finally, we need to consider the $M_S = 0$ block, for which we have

$$\binom{N_+}{2} \times \binom{N_-}{2} = 36\,.$$

Among these states, there are three possible numbers of pairs: $N_P = 2, 1, 0$. For $N_P = 2$, the

spin-up and spin-down fermions must occupy the same energy levels, so there are $\binom{4}{2} = 6$ options in total. For $N_P = 1$, we place one pair in one of the energy levels, and the spin-up and spin-down fermions must be assigned to levels with different energies. There are four possible choices for the pair, three for the first unpaired fermion, and then two for the remaining one, which implies that the dimension of the block is $4 \times 3 \times 2 = 24$. Finally, for $N_P = 0$, there are six configurations in which the particles are completely unpaired.

Since the overall dimension of the Hamiltonian matrix in our example is rather small, we can diagonalize H exactly, which will be very useful for benchmarking in the following. We can reduce this effort even further by diagonalizing the blocks separately. Moreover, if we're only interested in comparing ground-state energies, then for an attractive pairing force ($g > 0$), we can assume that the ground state will lie in the six-dimensional $M_S = 0, N_P = 2$ block of the matrix, and we will only need to diagonalize the matrix

$$H = \begin{bmatrix} 2\delta - g & -g/2 & -g/2 & -g/2 & -g/2 & 0 \\ -g/2 & 4\delta - g & -g/2 & -g/2 & 0 & -g/2 \\ -g/2 & -g/2 & 6\delta - g & 0 & -g/2 & -g/2 \\ -g/2 & -g/2 & 0 & 6\delta - g & -g/2 & -g/2 \\ -g/2 & 0 & -g/2 & -g/2 & 8\delta - g & -g/2 \\ 0 & -g/2 & -g/2 & -g/2 & -g/2 & 10\delta - g \end{bmatrix}. \tag{8.2}$$

Note that for weak pairing $g \ll 1$, the matrix is heavily dominated by the diagonal, and the diagonal entries are the eigenvalues of the one-body part of H. Thus, the configuration shown in Fig. 8.1 will be the dominant component of the exact ground state.

Now let us consider performing an IMSRG(2) calculation for the chosen model. Our first task is to choose a reference state. As argued in previous chapters, it is beneficial

to use a reference that is a good approximation to the ground state of the system, so the aforementioned basis configuration will be a suitable choice for $|\Phi\rangle$. Previously, we have argued for the use of Hartree-Fock optimized Slater determinants as references. In the present case, it turns out that the HF determinant is identical to $|\Phi\rangle$, and only the single-particle energies get modified:

$$\begin{aligned}\epsilon_{p\sigma} &= \delta(p-1) + \sum_{i\sigma'} \langle p\sigma i\sigma' | \, v \, | p\sigma i\sigma' \rangle = \delta(p-1) + n_{p\sigma} \langle p\sigma p-\sigma | \, v \, | p\sigma p-\sigma \rangle \\ &= \delta(p-1) - \frac{g}{2} n_{p\sigma} \,, \end{aligned} \tag{8.3}$$

where we have used the properties of the pairing interaction, as well as $n_{p\sigma} = 1$ for hole and 0 for particle states. This is not a surprising result: The optimal determinant produced by the HF procedure is decoupled from $1p-1h$ excitations by construction, but as mentioned above, the interaction term can only excite fermions pairwise. Thus, the $M_S = 0, N_P = 0$ block of the Hamiltonian matrix is spanned by $|\Phi\rangle$ as well as its $2p-2h$ and $4p-4h$ excitations.

In Fig. 8.3, we show the IMSRG(2) flow for the pairing model with 4 particles in 8 levels, using $\delta = 1.0$ and a pairing strength $g = 0.5$. The curves illustrate how correlations that can be captured by second- and third-order MBPT are absorbed into the flowing Hamiltonian, since the MBPT corrections to $E(s)$ are practically zero for $s \gg 1$. The final final ground-state energy $E(\infty) = 1.4133$ is slightly lower than the exact ground-state energy value of 1.4168, indicated by the dashed line, which we obtained by exact diagonalization of the Hamiltonian. This differences is due to the truncation of the IMSRG to two-body operators.

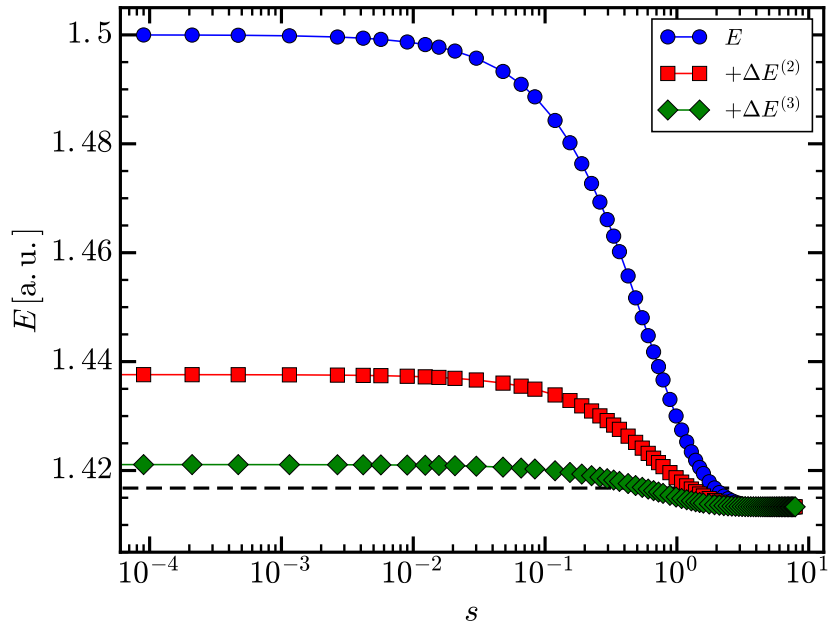

Figure 8.3: IMSRG(2) ground-state energy $E(s)$ (i.e., the zero-body part of $H(s)$) for 4 particles in 8 levels described by a pairing Hamiltonian with $\delta = 1.0$ and pairing strength $g = 0.5$. The White generator (3.21) was used for the calculation. The figure also displays the impact of the perturbative second ($\Delta E^{(2)}$) and third-order energy corrections ($\Delta E^{(3)}$) as a function of the flow parameter (s). The dashed line in the plot corresponds to the exact ground-state energy value. Adapted from [41].

8.1.2 The Pairing plus Pair-Breaking Model

As explained in the previous section, the pairing model exhibits symmetries that can be leveraged to simplify calculations, but which ultimately restrict the types of configurations that can mix with the ground-state. While spin and angular momentum are usually conserved by realistic nuclear interactions, the number of pairs is not, although pairing does play an important role in nuclei. To enhance the complexity of our model, we can add a pair-breaking interaction of the form

$$H = H_{\text{pair}} + \frac{1}{2} b \left(\sum_{pp'q}^{p \neq p'} a^\dagger_{p+} a^\dagger_{p'+} a_{q-} a_{q+} + \text{H.c.} \right) \tag{8.4}$$

where $H.c.$ indicates the Hermitian conjugate of the previous term in the parenthesis — this term would create a pair out of two fermions with opposite spins and different energy quantum numbers.

Referring to the Hamiltonian matrix as shown in Fig. 8.2, the pair-breaking interaction will populate the blocks adjacent to the diagonal, which couple the blocks with N_P to blocks with $N_P \pm 1$.

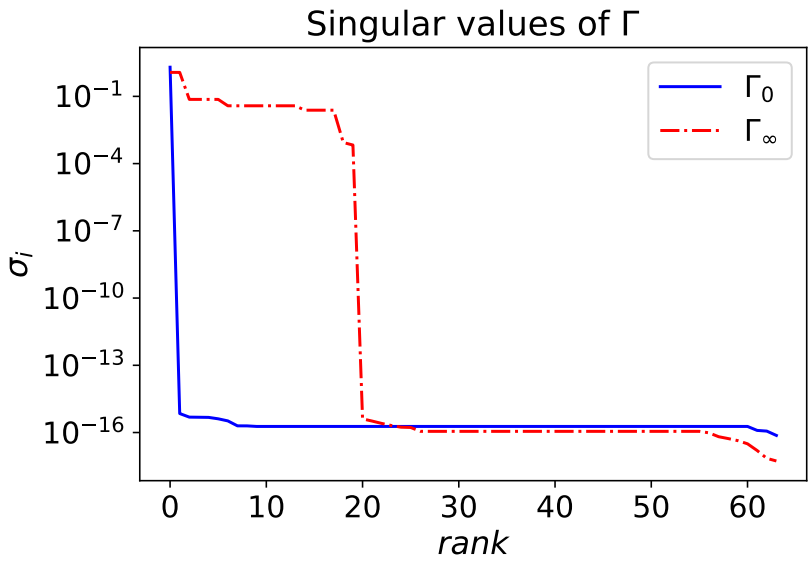

Figure 8.4: Singular Values Spectrum of initial Γ_0 and final Γ_∞. The solid curve represents the singular values spectrum of the initial Γ_0 matrix, indicating a rank of 1 and the presence of a single dominant feature. The dashed red curve corresponds to the singular value spectrum of evolved Γ_∞, revealing a higher rank of 20, suggesting a richer set of physical features compared to the initial Γ_0 matrix.

8.2 SVD-IMSRG(2) for the Pure Pairing Model

Let us now consider the SVD-IMSRG(2) for the pure pairing model. Since the one-body operator's dimension, N, is significantly smaller than that of the two-body operator, N^2, our main focus is on decomposing constructing a low-rank approximation of the two-body

part of the flowing Hamiltonian, Γ, that retains critical information and characteristics while allowing us to substantially reduce the computational cost of the IMSRG evolution.

We start by examining the singular values of the initial Gamma (Γ_0) and final Gamma (Γ_∞) coefficient matrices, which are shown in Fig. 8.4 for our example with $N = 8$ levels (i.e., Γ can be represented by a 64×64 matrix). Notably, Γ_0 exhibits a rank of one, indicating that it contains only one dominant feature — this is as expected, because the pairing interaction (8.1) is characterized by the single constant g. However, when considering the singular values of Γ_∞, we see that it has a rank of approximately 20, although most of the singular values are quite small compared to the dominant ones. Thus, the evolution induces contributions to Γ that effectively increase the rank, analogous to what we found in the momentum-space SVD-SRG applications discussed in Chapter 5, although the objects we are considering here are somewhat different.

Clearly, it would be a bad idea to use the one dominant singular vector of Γ_0 as a projector for the SVD-IMSRG flow equation, and it is impossible to anticipate which of the other remaining singular vectors that are associated with vanishing singular values may become important during the evolution. Naturally, we also want to avoid using the singular vectors of Γ_∞ as projectors, because this would force us to perform the evolution first, and defeat the purpose of the SVD-IMSRG.

However, we do have quantities available at $s = 0$ that may indicate how the system is going to evolve, namely the generator η and the derivative $\frac{d\Gamma}{ds}\Big|_{s=0}$ matrix. It turns out that the singular vectors of $d\Gamma$ are capable of capturing all the essential features of the Γ_∞, as illustrated in Figure 8.5b. In panel (a), we show Γ_∞ in the singular vector basis of Γ_0. While the resulting matrix is sparse and structured, non-zero matrix elements appear in its far off-diagonal sectors. In contrast, panel (b) shows Γ_∞ in the basis of singular vectors of

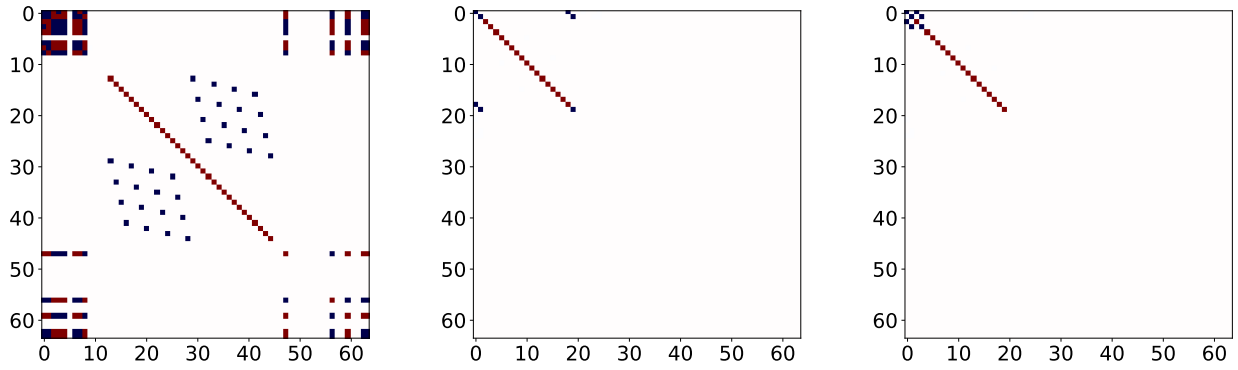

(a) (b) (c)

Figure 8.5: These graphs showcase the transformation of Γ matrices into singular spaces derived from various sources. *Panel (a):* Representation of Γ_∞ in the singular space of Γ_0. *Panel (b):* Representation of Γ_∞ in the singular space of $d\Gamma$. *Panel (c):* Representation of Γ_∞ in the singular space of $d\Gamma$ with basis permuted.

(a) (b)

Figure 8.6: These graphs shows the transformation of η matrices into singular spaces from $d\Gamma$. *Panel (a):* Representation of η in the singular space of $d\Gamma$. *Panel (b)* Representation of η in the permuted singular space of $d\Gamma$

$d\Gamma$, and we find that the matrix elements are confined to a 20x20 block in the upper left corner that suggests that the evolution can be captured in a space of dimension 20 instead of 64. Moreover, there are only two matrix elements located at the off-diagonal corners of the matrix in this proposed effective space. The objective in the following is to relocate the singular vectors associated with these points to the foremost upper left corner, creating a distinct elongated tail. This rearrangement facilitates a more convenient truncation process, as illustrated in Figure 8.5c. While some may perceive this step as unnecessary, we emphasize its significance. Neglecting the basis permutation could lead to challenges in truncation, particularly when employing only a few singular vectors. This becomes evident when viewing the matrix representation in the singular space as a covariance matrix. Consequently, the singular vectors linked to these off-diagonal points exhibit correlation, Disregarding points during truncations may result in a divergent evolution, rather than convergence. Therefore, the careful consideration of basis permutation becomes crucial to ensure the stability and accuracy of the evolution process, especially in scenarios where the matrix representation involves correlated elements.

Next, we consider the representation of η in the singular space of $d\Gamma$. In the basis selection process, we project the matrix η at the initial point ($s = 0$) onto the singular space of $d\Gamma$, as depicted in Figure 8.6a. Strikingly, we observe a resemblance between the representation of η and that of Γ_∞ in Figure 8.5b. To optimize the basis arrangement, our objective is to reorganize the basis such that the representation of η aligns with the 4 by 4 block in the upper left corner, leading to a representation of Γ_∞ resembling that shown in Figure 8.5c.

By achieving this configuration, we can effectively compute the pairing model using only 4 components, which results in a stable and rapid calculation. particularly in scenarios where the particle-hole term is not considered. Furthermore, the potential for including

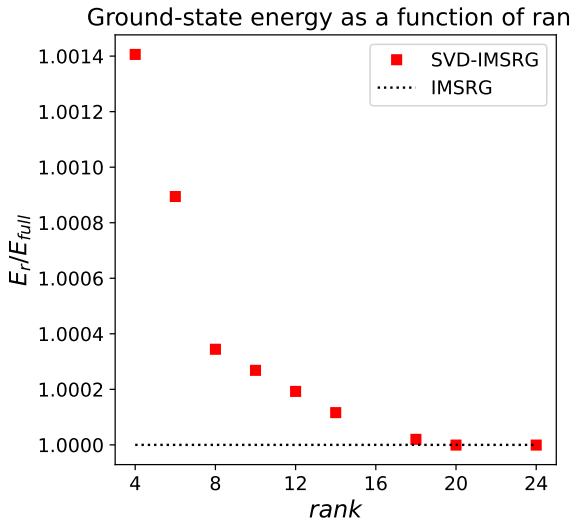

(a) Model with 4 particles and 8 single-particle states

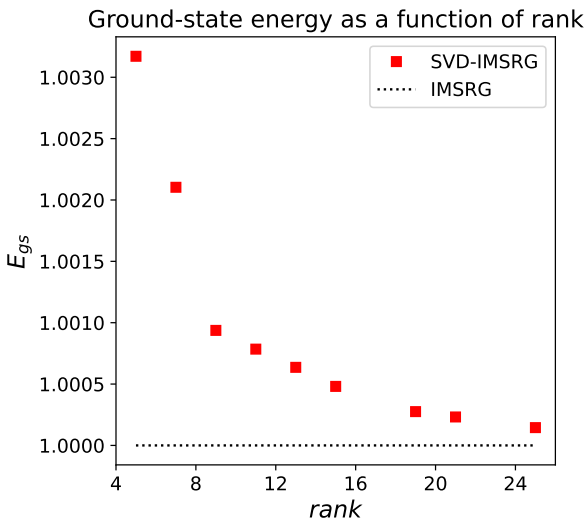

(b) Model with 4 particles and 20 single-particle states

Figure 8.7: These figures showcases the ground-state energy ratio, as a function of included rank in the SVD-IMSRG calculation. The x-axis denotes the rank considered in the SVD-IMSRG, while the y-aixs represents the ratio of rank-reduced ground-state enregy to the full-rank ground-state energy. The red points in both subfigures (a) and (b) depict the results obtained from SVD-IMSRG computations. For comparison, the dashed line represents the ground-state energy ratio calculated from full-rank IMSRG. Subfigure (a): Model with 4 particles and 8 single-particle states. Subfigure (b): Model with 4 particles and 20 single-particle states.

more components exists. Since the remaining block is diagonal, we can strategically omit calculations for the entire 16 by 16 block, and instead focus solely on the diagonal elements of 16, substantially expediting the computation process.

Next, we consider the ground-state energy of our model system in the SVD-IMSRG(2) as a function of the rank, i.e., the number of singular vectors of $d\Gamma$ that are used to project the flow equations, after performing the basis rearrangement and selection (cf. Fig. 8.5).

Initially, we compute the ground-state energy of the system using only 4 components and subsequently increment the number of components in steps of two or four, up to 24 components. Intriguingly, even with just 4 components, the SVD-IMSRG(2) calculation produces highly accurate results. yielding an error of approximately 0.1%. As we include

more components, the error diminishes exponentially. Remarkably, when we include 20 components (corresponding to the rank of the system), we effectively capture all the necessary information, resulting in convergence to the ground-state energy obtained from the general IMSRG(2) approach. Further inclusion of components does not impact the results since no additional physics is involved, as shown in Figure 8.7a.

Additionally, we apply the pairing model to a scenario with 4 particles distributed among 20 single-particle states, resulting in a 400-dimensional Γ matrix. In this case, the rank of Γ_∞ is 69. While we do not consider all these components in the calculation, as depicted in Figure 8.7b, we observe that even with just 4 components (similar to the 4-particle, 8-state model), the results remain highly accurate, with an error of around 0.3% compared to the general IMSRG(2) results. As we progressively include more components, the accuracy improves exponentially, aligning with our previous findings.

These calculations demonstrate the efficacy and efficiency of the SVD-IMSRG(2) method in accurately computing the ground-state energy of pairing models with varying dimensions. The results showcase the potential for obtaining precise outcomes with reduced computational costs, making the approach particularly suitable for larger systems.

8.3 SVD-IMSRG(2) for a Pairing plus Pair-Breaking Model

Presently, we enhance the model by introducing a particle-hole term to the Hamiltonian. Let's analyze the singular values of the Γ_0 and Γ_∞ once more. Remarkably, the Γ_0 exhibits a rank of 2, signifying the presence of only two dominant features: a pairing interaction and a pair-breaking interaction, respectively. In contrast, upon considering the Γ_∞, we observe a

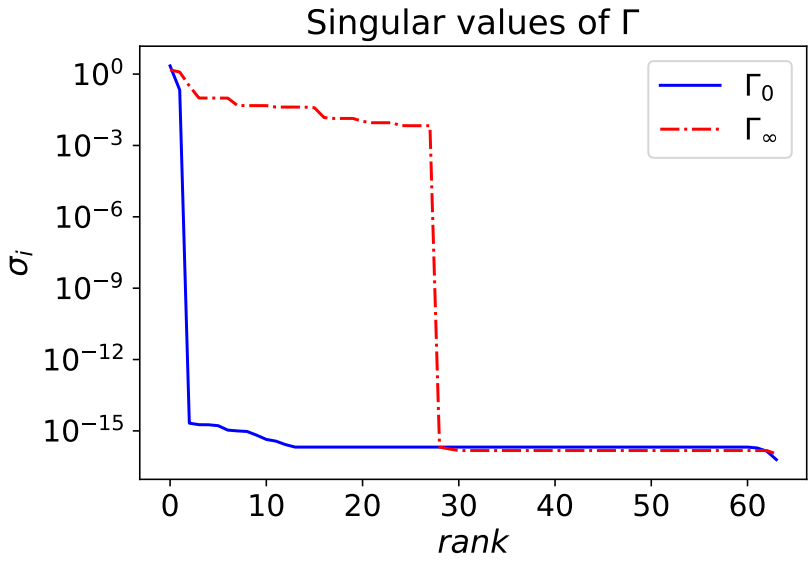

Figure 8.8: Singular Values Spectrum of Γ_0 and Γ_∞. The solid curve represents the singular values spectrum of the Γ_0, indicating a rank of 2, signifying the presence of two dominant features. The dashed red curve corresponds to the singular values spectrum of the Γ_∞, revealing a higher rank of 28, suggesting a richer set of physical features compared to the Γ_0.

higher rank of 28, as depected in Figure 8.8. This finding once again emphasizes the lower-rank singular space of Γ_0 is inadequate in effectively capturing the physical features present in the Γ_∞, as shown in Figure 8.9a. As discussed in the previous section, our objective is to perform truncation in the upper left corner of the singular space to retain the most relevant and critical features.

Figure 8.9b illustrates the representation of the Γ_∞ in the singular space derived from $d\Gamma$, which forms a single 28 by 28 block. However, when we implement the $d\Gamma$ space with basis selection, as discussed in previous section, the representation of the Γ_∞ matrix in the singular space, as shown in Figure 8.9d, reveals two decoupled blocks. In comparison, the singular space representation of the Γ_0 matrix derived from $d\Gamma$ with basis selection consists of a single 10 by 10 block. This observation indicates that the IMSRG calculation drives an additional block of size 18 by 18, suggesting the emergence of distinct physical phenomena or

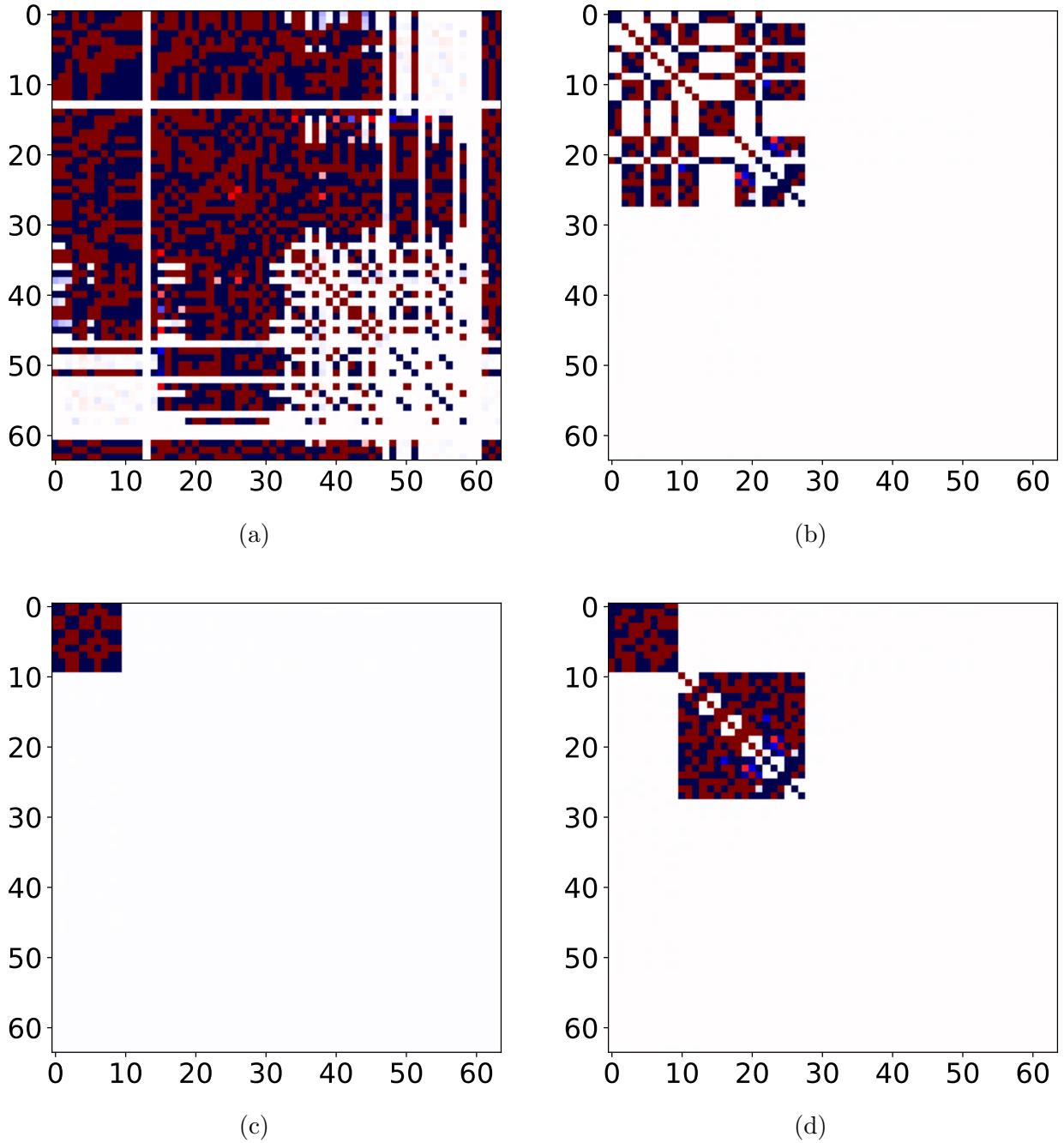

Figure 8.9: The graphs illustrate the SVD of four distinct Γ matrices, each represented in a unified manner. The subgraphs depict the transformation of these Γ into their respective singular spaces, derived from different sources. Subgraph (a): Γ_∞ singular space representation from Γ_0. Subgraph (b): Γ_∞ singular space representation from $d\Gamma$. Subgraph (c): Γ_0 singular space representation from $d\Gamma$ with basis permutation. Subgraph (d): Γ_∞ singular space representation from $d\Gamma$ with basis permutation.

modes in the system. The basis selection plays a crucial role in capturing these features, as evident from the partitioned structure observed in Figure 8.9d. This analysis highlights the significance of basis manipulation and its impact on revealing different facets of the system's behavior within the IMSRG framework.

In the $d\Gamma$ space, the representation of Γ_∞ exhibits two decoupled blocks. This suggests the possibility of independently and simultaneously evolving these two blocks intead of evolving the entire block, as shown in Figure 8.9b. However, even evolving two smaller blocks simultaneously remains computationally demanding. Therefore, our primary interest lies in udnerstanding the contribution form the second block. If this contribution is found to be relatively small, we can effectively disregard the derived block and proceed with the implementation of SVD-IMSRG(2) solely using the primary block. By doing so, we significantly reduce computational complexity and enhance efficiency in our calculations.

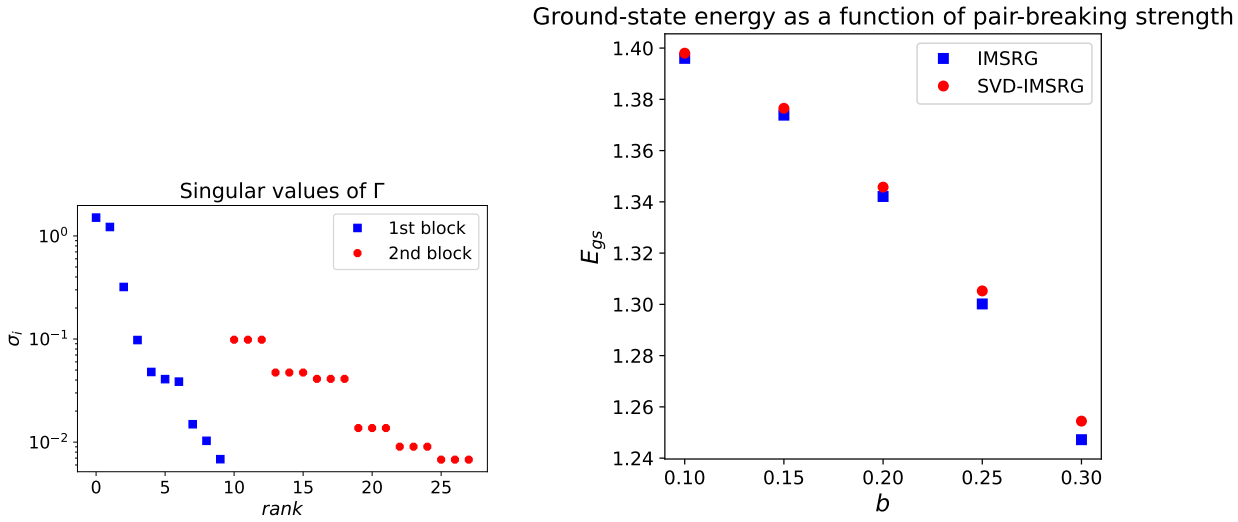

(a) (b)

Figure 8.10: The left panel illustrates the cumulative sum of singular values for the primary block, which constitutes 83% of the total. These results were obtained for $b = 0.1$. The right panel showcases the SVD-IMSRG calculation using the primary block only, represented in red and is compared to the result from the general IMSRG method shown in blue.

To pursue this objective, we commence our investigation by examining the singular spectrum of each block, as depicted in Figure 8.10a. The cumulative sum of singular values for the first block contributes significantly, accounting for approximately 83.58% of the total singular values encompassing the entire block. On the other hand, the second block's cumulative sum accounts for a relatively smaller portion, approximately 16.42% of the total singular values. It is important to note that the magnitude of singular values corresponds to the amount of information contained within.

While the significance of the second block's contribution cannot be disregarded entirely, its relatively smaller cumulative sum suggests a potentially lesser impact on the calculation of ground-state energy. Anticipating an approximate accuracy of 85% in the results obtained from SVD-IMSRG with the primary block is reasonable. Nonetheless, it is vital to acknowledge that not all singular components play an equal role in the energy calculation.

We then conducted a comprehensive investigation using SVD-IMSRG, focusing on the primary block to assess the significance of the second block. In this analysis, we deliberately excluded the evolution of the second block, as shown in Figure 8.10b. Our study involved varying the strength of the pair-breaking term. We plotted the results obtained from SVD-IMSRG in red and results from the general IMSRG in blue. The distintictive gaps between these two sets of result indicate the contribution arising from the second block. Specifically, for a pair-breaking strength of $b = 0.1$, the observed error between IMSRG and SVD-IMSRG amounted to approximately 0.15%. As we increased the pair-breaking strength to $b = 0.3$, the discrepancy remained within 1%, which is approximately 0.6%. When applying SVD-IMSRG to the system, the pair-breaking part can exhibit stronger correlations, which may not be adequately captured by the low-rank approximation. As the pair-breaking strength, denoted by parameter "b", increases, the impact of this term, or the second block, becomes

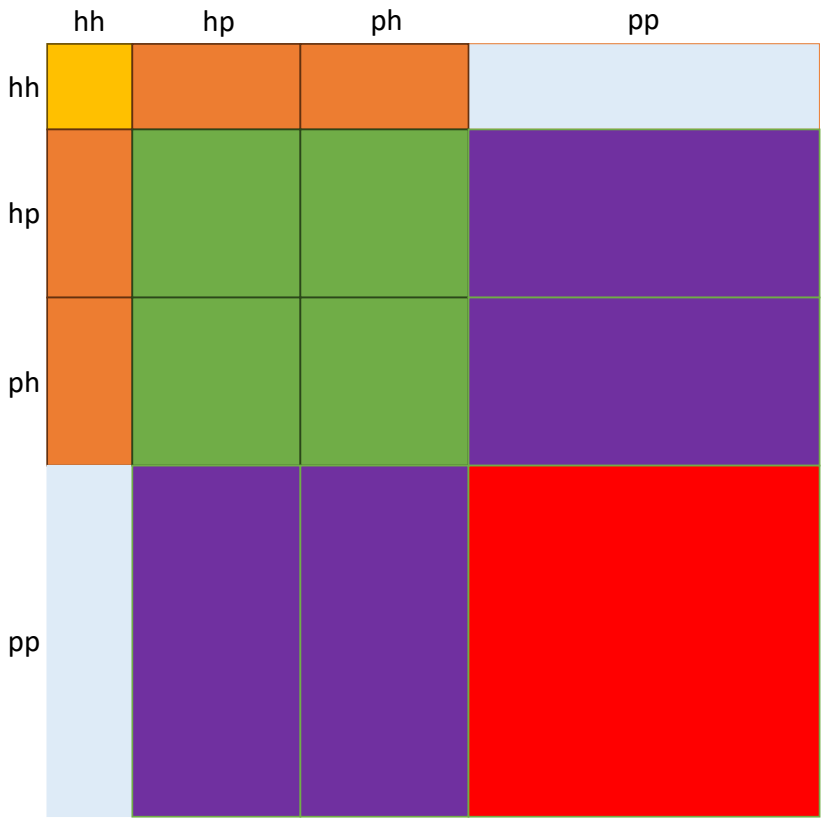

Figure 8.11: The Γ Matrix Mosaic. Divided into 16 captivating pieces, 6 essential blocks are painted in vivid colors encapsulate the heart of essential information. Every hue signifies distinct physics, while symmetrical copies unveil the dance of hermitian and anti-symmetrization, where shared colors embrace with a twist of sign change.

more pronounced, leading to challenges in the approximation. Truncationor or omission of these terms can result in increased error and reduced accuracy in the model.

In summary, the examination of the singular spectrum reveals the contrasting contributions of the two blocks. While the second block's cumulative sum indicates its importance, its role in calculating ground-state energy may not be on par with that of the first block. A deeper analysis of the specific singular components and their respective significance in the energy calculation is warranted to draw conclusive insights.

Chapter 9

SVD-IMSRG for Infinite Matter

9.1 Preliminaries

In this section, we briefly recapitulate the construction of single-particle basis and the representation of two-nucleon interactions in infinite matter calculations, following Ref. [63].

9.1.1 Single-Particle Basis for Infinite Matter

The description of infinite nuclear matter relies on plane-wave functions that are confined to a box with volume Ω and side length L, which quantizes the spectrum. (Eventually, one needs to take the limit $L \to \infty$ in computed expectation values.) The wave function is given by

$$\Psi_{\mathbf{k}\sigma}(\mathbf{r}) = \frac{1}{\sqrt{2\Omega}} \exp(i\mathbf{k}\mathbf{r})\xi_\sigma \tag{9.1}$$

where $\mathbf{k}$ denotes the wave number, and ξ_σ are basic spinors for nucleons with either spin up or spin down:

$$\xi_{\sigma=+1/2} = \begin{pmatrix} 1 \\ 0 \end{pmatrix} \qquad \xi_{\sigma=-1/2} = \begin{pmatrix} 0 \\ 1 \end{pmatrix}. \tag{9.2}$$

We can think of an infinitely extended system in terms of periodic copies of our "elementary" box, which implies the use of periodic boundary conditions on the single-particle wave functions. These conditions impose constraints on the allowed wave numbers, which can be

represented as

$$k_{n_i} = \frac{2\pi n_i}{L} \qquad i = x, y, z \qquad n_i = 0, \pm 1, \pm 2, \cdots \tag{9.3}$$

The kinetic energy operator can then be expressed as

$$T = \sum_{\mathbf{p}\sigma_p} \frac{\hbar^2 k_p^2}{2m} a^\dagger_{\mathbf{p}\sigma_p} a_{\mathbf{p}\sigma_p} \tag{9.4}$$

where $a^\dagger_{\mathbf{p}\sigma_p}$ and $a^\dagger_{\mathbf{p}\sigma_p} a_{\mathbf{p}\sigma_p}$ are the creation and annihilation operators, respectively, associated with the momentum state represented by the wave number $\mathbf{p}$. When applying periodic boundary conditions, the discretization of the single-particle momenta lead to the following expression for the single-particle energy:

$$\varepsilon_{n_x,n_y,n_z} = \frac{\hbar^2}{2m}\left(k_{n_x}^2 + k_{n_y}^2 + k_{n_z}^2\right) = \frac{\hbar^2}{2m}\left(\frac{2\pi}{L}\right)^2 \left(n_x^2 + n_y^2 + n_z^2\right) . \tag{9.5}$$

To avoid singling out specific spatial directions, we impose truncations on the single-particle basis by restricting the single-particle energy $\varepsilon_{n_x,n_y,n_z} \leq \varepsilon_{\max}$ (or, equivalently, the total single-particle momenta or quantum numbers n_i). It is clear from Eq. (9.5) that for each ε allowed by the truncation, we may have several energetically degenerate realizations through different combinations of the quantum numbers n_x, n_y, n_z. Thus, the single-particle basis will have a structure analogous to a shell model.

In our calculations, we ensure a "closed-shell" structure for both occupied and unoccupied single-particle states by carefully including all single-particle states with energies below our predetermined cutoff. Consider, for example, the case

$$\left(n_x^2 + n_y^2 + n_z^2\right) \leq 3 . \tag{9.6}$$

$n_x^2 + n_y^2 + n_z^2$	n_x	n_y	n_z	$N_{\uparrow\downarrow}$
0	0	0	0	2
1	-1	0	0	
1	1	0	0	
1	0	-1	0	
1	0	1	0	
1	0	0	-1	
1	0	0	1	14
2	-1	-1	0	
2	-1	1	0	
2	1	-1	0	
2	1	1	0	
2	-1	0	-1	
2	-1	0	1	
2	1	0	-1	

$n_x^2 + n_y^2 + n_z^2$	n_x	n_y	n_z	$N_{\uparrow\downarrow}$
2	1	0	1	
2	0	-1	-1	
2	0	-1	1	
2	0	1	-1	
2	0	1	1	38
3	-1	-1	-1	
3	-1	-1	1	
3	-1	1	-1	
3	-1	1	1	
3	1	-1	-1	
3	1	-1	1	
3	1	1	-1	
3	1	1	1	54

Table 9.1: Total number of particles $N_{\uparrow\downarrow}$ for various $n_x^2 + n_y^2 + n_z^2$ values for one spin-1/2 fermion species, accounting for a spin degeneracy of 2 for each energy state.

The resulting list of energy levels is presented in Table ??, considering one species of identical fermions and accounting for both spin-up and spin-down solutions.

If we were to consider $n_x^2 + n_y^2 + n_z^2 = 4$, we obtain 6 additional energy levels (with one $n_i = \pm 2$ and the others vanishing) and 12 additional states due to spin degeneracy, resulting in a new magic number of 66. Proceeding in this manner, one obtains the magic numbers of 2, 14, 38, 54, 66, 114, ... For the study of infinite nuclear matter with both protons and neutrons, the magic numbers become 4, 28, 76, 108, 132, 228, and so on.

Once the number of particles in the simulation is determined, and a specific density ρ is chosen, the Fermi momentum k_F of the system is determined by the equation

$$\rho = g\frac{k_F^3}{6\pi^2} \tag{9.7}$$

where g represents the degeneracy. For a system of one type of spin-1/2 particles, the degeneracy is 2, while for nuclear matter with protons and neutrons, it is 4.

Since we are typically interested in the energy of neutron or nuclear matter at a fixed density, we can use ρ and the particle number A that we choose according to our "closed-shell criterion" to define the size of the simulation box via

$$\Omega = L^3 = \frac{A}{\rho}\,. \tag{9.8}$$

9.1.2 Two-Nucleon Interaction

In the study of infinite matter properties, a plane wave basis described above is employed. While a Cartesian basis enables direct matrix element calculations, it has limitations as a discrete and finite approximation. Instead, we employ a partial wave expansion for the nucleon-nucleon interaction, which allows us to compute the Hartree-Fock energy of the ground-state in the thermodynamical limit with a constrained number of partial waves. By expressing the Hartree-Fock energy in a partial wave basis, we conveniently rewrite the two-body force in terms of relative and center-of-mass motion momenta, facilitating a comprehensive comparison between the two approaches.

The direct matrix element is defined in terms of the single-particle three-dimensional momenta $\mathbf{k}_p$, spin σ_p and isospin τ_p, as follows

$$\langle \mathbf{k}_p \sigma_p \tau_p \mathbf{k}_q \sigma_q \tau_q | \, \hat{v} \, | \mathbf{k}_r \sigma_r \tau_r \mathbf{k}_s \sigma_s \tau_s \rangle \tag{9.9}$$

By introducing the relative momentum and the center-of-mass momentum

$$\mathbf{k} = \frac{1}{2}(\mathbf{k}_p - \mathbf{k}_q) \tag{9.10}$$

$$\mathbf{K} = \mathbf{k}_p + \mathbf{k}_q \tag{9.11}$$

we have

$$\begin{aligned}\langle \mathbf{k}_p\sigma_p\tau_p\mathbf{k}_q\sigma_q\tau_q|\hat{v}\,|\mathbf{k}_r\sigma_r\tau_r\mathbf{k}_s\sigma_s\tau_s\rangle &= \langle \mathbf{k}\mathbf{K}\sigma_p\tau_p\sigma_q\tau_q|\,\hat{v}\,|\mathbf{k}'\mathbf{K}'\sigma_r\tau_r\sigma_s\tau_s\rangle \\ &= \delta_{T_zT_z'}\delta(\mathbf{K}-\mathbf{K}')\,\langle \mathbf{k}T_zS_z=(\sigma_a+\sigma_b)|\,\hat{v}\,|\mathbf{k}'T_zS_z'=(\sigma_c+\sigma_d)\rangle \\ &= \delta_{T_zT_z'}\delta(\mathbf{K}-\mathbf{K}')\,\langle T_zS_z|\,\hat{v}(\mathbf{k},\mathbf{k}')\,|T_zS_Z'\rangle\end{aligned} \tag{9.12}$$

where the first equality comes from the conservation of the total momentum and charge. In the second equality, we defined the isospin projections $T_z = \tau_p + \tau_q$ and $T_z' = \tau_r + \tau_s$. Subsequently, these matrix elements can be expressed in terms of the total two-body quantum numbers, specifically for the spin S of two spin-1/2 fermions, as

$$\langle \mathbf{k}T_zS_z|\,\hat{v}(\mathbf{k},\mathbf{k}')\,|\mathbf{k}'T_zS_z'\rangle = \sum_{SS'}\langle\tfrac{1}{2}\sigma_p\tfrac{1}{2}\sigma_q|SS_z\rangle\,\langle\tfrac{1}{2}\sigma_r\tfrac{1}{2}\sigma_s|S'S_z'\rangle\,\langle \mathbf{k}T_zSS_z|\,\hat{v}(\mathbf{k},\mathbf{k}')\,|\mathbf{k}T_zS'S_z'\rangle \tag{9.13}$$

The coefficient $\langle\frac{1}{2}\sigma_p\frac{1}{2}\sigma_q|SS_z\rangle$ are known as Clebsch-Gordan recoupling coefficients. We will assume that our interactions conserve charge, ans we will refer to $T_z = 0$ as the pn (proton-neutron) channel, $T_z = -1$ as the pp (proton-proton) channel, and $T_z = -1$ as the nn (neutron-neutron) channel.

The nucleon-nucleon force is frequently studied and analyzed using a partial wave expansion. A state with linear momentum $\mathbf{k}$ can be expressed in terms of spherical harmonics Y_{lm} as follow

$$|\mathbf{k}\rangle = \sum_{l=0}^{\infty}\sum_{m=-l}^{l}\iota^l Y_{lm}\,\langle\hat{k}|klm_l\rangle \tag{9.14}$$

The potential in momentum space is connected to the nonlocal operator $V(\mathbf{r},\mathbf{r}')$ in terms of $\mathbf{k}$ and $\mathbf{K}$ as

$$\langle \mathbf{k}'\mathbf{K}'|\,\hat{v}\,|\mathbf{k}'\mathbf{K}\rangle = \int d\mathbf{r}d\mathbf{r}'e^{-\iota\mathbf{k}'\mathbf{r}'}V(\mathbf{r}',\mathbf{r})e^{-\iota\mathbf{k}\mathbf{r}}\delta(\mathbf{K},\mathbf{K}') \tag{9.15}$$

We make the assumption that the interaction is spherically symmetric and utilize the partial wave expansion of the plane waves in terms of spherical harmonics. As a result, we can separate the radial part of the wave function from its angular dependence. The wave function of the relative motion can be described in terms of plane waves as

$$e^{-\iota \mathbf{kr}} = \langle \mathbf{r}|\mathbf{k}\rangle = 4\pi \sum_{lm} \iota^l j_l(kr) Y^*_{lm}(\hat{\mathbf{k}}) Y_{lm}(\hat{\mathbf{r}}) \tag{9.16}$$

where j_l is a spherical Bessel function and Y_{lm} the spherical harmonic. The nucleon-nucleon interaction can be conveniently described using a partial wave basis, where the operator exhibits symmetry under rotations, parity, and isospin transformation. This symmetry ensures that the interaction is diagonal with respect to the quantum numbers of total angular momentum (J), spin (S), and isospin (T). Utilizing the plane wave expansion and coupling to final J, S and T states, we obtain the following results

$$\langle \mathbf{k'}| V |\mathbf{k}\rangle = (4\pi^2) \sum_{JM} \sum_{lm} \sum_{l'm'} \iota^{l+l'} Y^*_{lm}(\hat{\mathbf{k}}) Y_{lm}(\hat{\mathbf{k'}}) \mathcal{C}^{l'SJ}_{m'M_S M} \mathcal{C}^{lSJ}_{mM_S M} \langle k'l'STJM| V |klSTJM\rangle \tag{9.17}$$

where

$$\langle k'l'STJM| V |klSTJM\rangle = \int j_{l'}(k'r') \langle l'STJM| V(r',r) |lSTJM\rangle j_l(kr) r'^2 dr' r^2 dr \tag{9.18}$$

The omission of the center-of-mass motion momentum $(\mathbf{K})$ and the corresponding orbital momentum $(\mathbf{L})$ is justified since the interaction is diagonal with respect to these variables.

This particular task, involving the construction of the Hamiltonian for infinite matter, falls beyond the scope of my work. This task has already been accomplied by Omokuyani and Kang, as documented in their research, In their study, the NNLO (Next-to-Next-to-

Leading Order) interaction is utilized to construct the Hamiltonian for the system under investigation.

9.2 SVD-IMSRG(2) for Infinite Matter

In this section, our focus lies in investigating the low-rank structure of infinite neutron matter. The matrix used for this analysis has been obtained from Omokuyani and Kang, incorporating the NNLO (Next-to-Next-to-Leading Order) interaction. The parameters for the matrix are as follows: A = 38, representing the number of hole-states, and N_{max} = 4, signifying that there are 66 single-particle states, of which 28 are particle-states (66−38 = 28). Consequently, the dimension of the Hamiltonian(Γ) matrix is $4356(66^2)$.

Incorporating the NNLO interaction results in complex-valued matrix elements. As explained in earlier sections, the matrix is created along the diagonal, as shown in Figure 9.1a, with each block corresponding to partial waves with unique total momentum $\mathbf{K}$ and total spin projection S_z. Within each block, the basis states are organized based on $\mathbf{k}_p$+$\mathbf{k}_q$ = $\mathbf{K}$ = $\mathbf{k}_r$+$\mathbf{k}_s$, where each $\mathbf{k}_i$ has three components representing n_x, n_y and n_z, along with certain prefactors. The individual dimensions of each block are visually elucidated, with the largest among them boasting an approximate dimension of 130, see Figure 9.1b. This organization facilitates a structured representation of the states and simplifies the analysis of the system's properties.

The singular values spectrum is meticulously depicted in Figure 9.1c, revealing a notable alignment in rank between Γ_0 and Γ_∞, both possessing an equivalent rank of 2145. This alignment elegantly satisfies the stipulations set forth in Eq. **??**. Evidently, this congruence of rank signifies that Γ_0 and Γ_∞ retain their maximal ranks throughout their evolution.

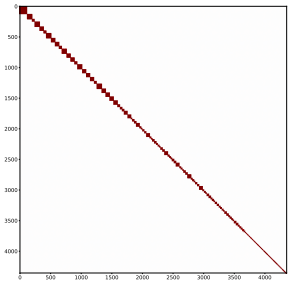

(a) Infinite Matter Matrix Representation

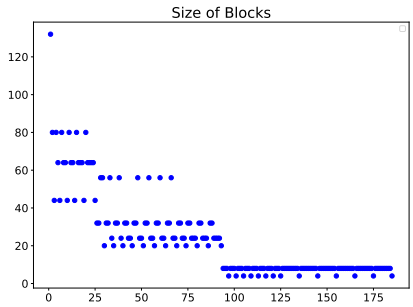

(b) The Dimension of each Block

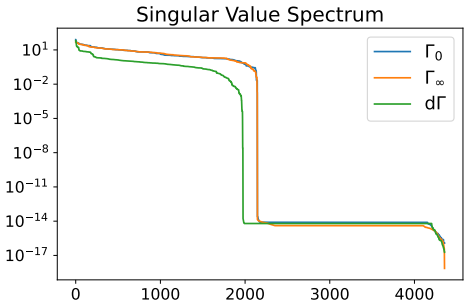

(c) Singular Value Spectrum

Figure 9.1: Visualizing Quantum Insights: (a) Infinite Matter diagonal representation in the chosen basis. (b) Blocks illuminated. Sizes vary, with the largest around 130, showcasing their significance. (c) Singular Values Spectrum of Γ_0, Γ_∞ and $d\Gamma$. Γ_0 and Γ_∞ equal in size, whereas $d\Gamma's$ spectrum takes slight variation.

Remarkably, this congruence implies that the subspace encapsulated by Γ_0 profoundly captures the essential physics embodied by Γ_∞, establishing a profound connection between these two entities. In a fascinating contrast, the rank of $d\Gamma$ emerges slightly diminished in comparison to Γ_0. This observation indicates that the subspace represented by $d\Gamma$ remains a subset within the realm of Gamma, insufficient to encapsulate the entirety of $\Gamma's$ complex physics within its confines. The nuanced interplay between these ranks and subspace affords profound insights into the dynamics of the underlying physics system.

Turning our attention to the low-rank structures of Γ_∞, and Ω_∞ previously discussed in Sec. 3.5, we adopt an approach akin to our treatment in the pairing model, akin to Figure 9.2 and Figure 9.2. Building upon our established methodology, we project the dynamic evolution of Γ_∞ onto the singular basis derived from Γ_0, adhering to the earlier prescribed basis selection.

Analogous to the paradigm observed in the pairing model, discernible patterns emerge, featuring two disentangled blocks within both Γ_∞ and Ω_∞. The ensuing exploration extends to the examination of the respective singular value spectra, adorning Figure 9.2 and Figure

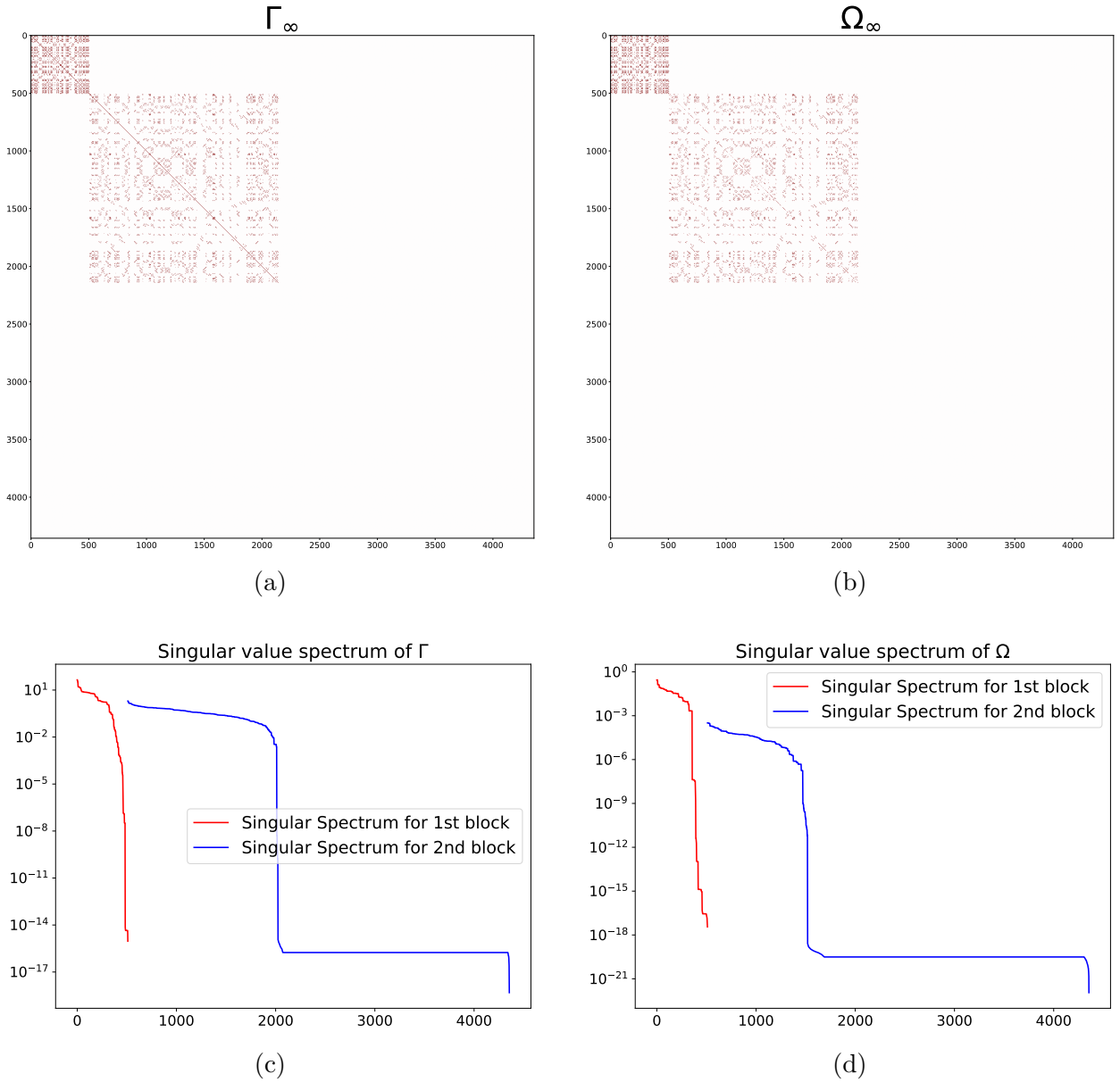

Figure 9.2: A Visual Journey through (a) to (d). Exploring low-rank structures and singular value spectra of Γ_∞ and Ω_∞, showcasing decoupled blocks and cumulative singular value contributions. Unveiling patterns and parallels, forging a pathway to future investigation.

9.2 for Γ_∞ and Ω_∞, respectively. Of significant note, the cumulative sum of singular values exhibited by the first block within Γ_∞ contributes to a remarkable 76% of the aggregate sum of all singular values. In striking contrast, its counterpart within Ω_∞ commands a staggering 99.7% of the cumulative sum. Such nuanced distinctions illuminate the profound disparities that emerge between these two distinct domains.

Further inquiries are kindled by the parallel conducted study involving the pairing model, where we employed the general IMSRG and SVD-IMSRG approaches. The utilization of the first block, boasting a cumulative sum of singular values accounting for 76% of the total, yielded impressively accurate results, hovering around the 99% precision mark.

Notably, this observation mirrors the findings within the infinite matter context, wherein an omission of approximately 25% of the singular values yet garners an admirably high level of accuracy. This intriguing pattern opens the door for comprehensive exploration, warranting future investigations to unearth the underlying mechanisms at play.

Chapter 10

Block Structures and Further Development of SVD-IMSRG

As depicted in Figure 8.11, the Γ matrix is strategically segmented into 16 distinct components, with 6 among them encapsulating the essential physical information. In light of this configuration , the current section embarks upon an in-depth investigation of the evolution equations across each of these meticulously defined blocks. Departing from the conventional approach of propagating the entirety of the matrix, the focus shifts towards the progressive evolution of these more compact blocks. This insightful strategy serves a dual purpose: it unveils the underlying low-rank structural attributes inherent to each individual block while simultaneously delving into the intricate particle-hole interaction contributions embedded within.

The pursuit of this endeavor is driven by an acknowledgement of the intricate and multifaceted nature of the challenge at hand. As a measure of prudent resource allocation, we endeavor to assess the significance of the particle-hole interaction contribution within each block. By quantifying its magnitude and discerning its relevant impact, we discern the feasibility of its exclusion in certain blocks where its contribution is comparatively marginal. This judicious exploration is driven by the aspiration to distill complexity and prioritize salient elements within our investigation.

Moreover, an inherent advantage of our approach lies in the focused handling of smaller, intricately defined blocks. This tactical shift not only grants us deeper insights but also accentuates computational efficiency. The expedited evolution of these confined blocks stands in stark contrast to the computational overhead entailed by the holistic evolution of the entire matrix. This operational expediency resonates well with our pursuit of informed efficiency.

In summary, this section illuminates a nuanced investigative methodology, capitalizing on the segmented structure of the Γ matrix. By unraveling the dynamics of individual blocks, we endeavor to uncover the underlying dynamics and glean valuable insights, thereby harnessing efficiency and depth in our pursuit of elucidating fundamental phenomena.

Moving forward, we address the practical scenario wherein the number of particle states far exceeds that of hole states – typically denoted as $(N_p = 10 \sim 15)N_h$. In the context of Block-IMSREG, due to manipulation of a reduced set of matrix elements, we anticipate an acceleration in evolution despite the time complexity remaining at $\mathcal{O}(N_h^2 N_p^4)$, as discuss in Section 3.2.2, or in Equation 3.14. Notably, our calculations involve the IMSRG and Block-IMSRG methods applied to a pairing model exhibiting defined randomness,

$$\Gamma^R_{ijkl} = R_{ijkl} \exp^{-(f_{ii}+f_{jj}-f_{kk}-f_{ll})^2/\lambda^2} \tag{10.1}$$

where R is random but Hermitized and antisymmetrized, and Γ_R, a Gaussian randomness, is introduced to achieve a maximum rank in the presence of a pair-breaking term in Γ_0, aligning the model more closely with real-world systems. This pragmatic step enhances the veracity of our analysis by better simulating complex system behavior.

Within the set of six fundamental blocks, three predominant bases emerge: hh, hp and pp. As illustrated in Figure 10.1, the entirety of these six blocks undergoes a projection

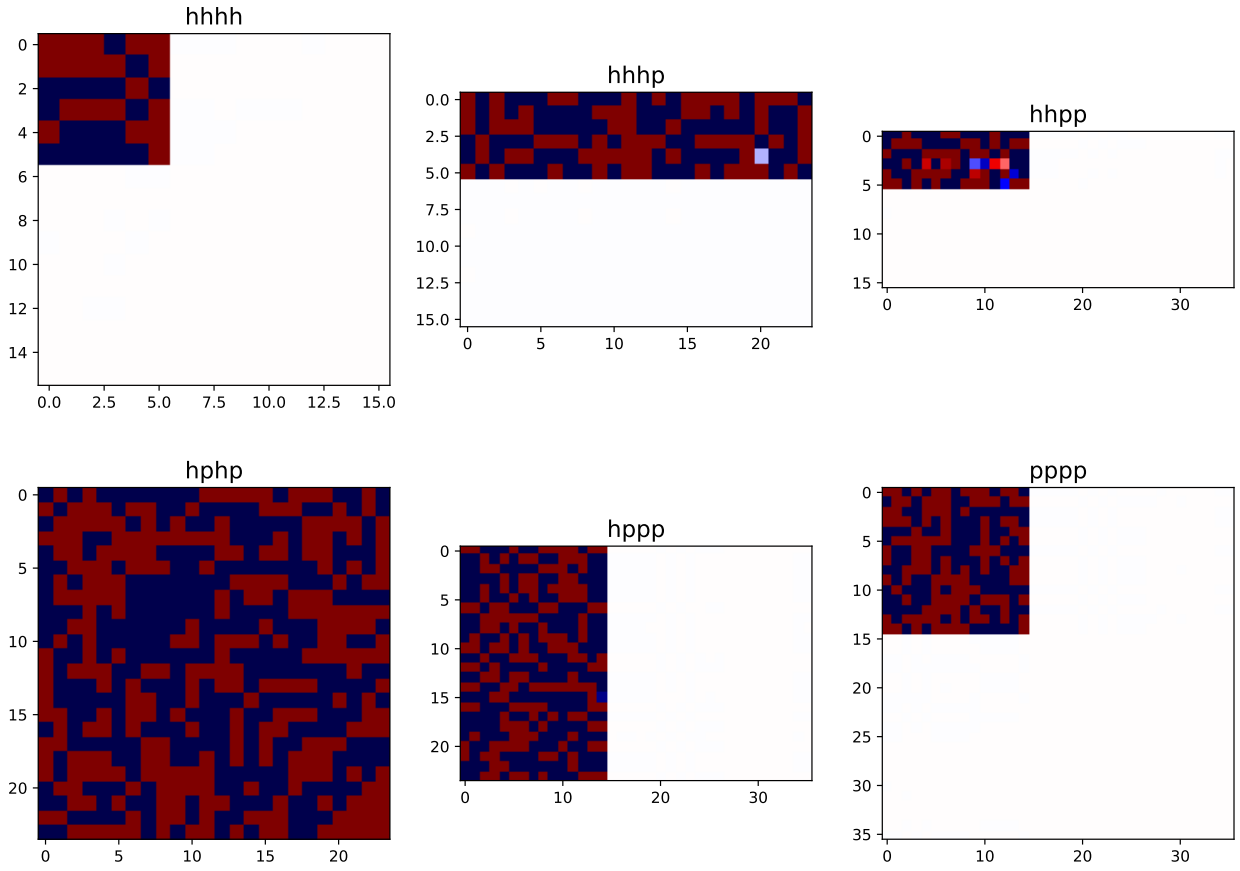

Figure 10.1: Representation of the 6 Essential blocks in corresponding singular bases for the pairing model with 0.5 pairing interaction and 0.1 pair-breaking term. The hole states' size is 4 and single-particle states' size is 10.

onto the *hh*, *hp* and *pp* bases. The selection of bases stems from the decomposition of the hhhh, hphp and pppp blocks. The hhhh and pppp representations, as previously discussed, adhere to a rank determined by Equation (**??**), which asymptotically converges to half the dimension of the respective blocks. Unsurprisingly, the hphp representation achieves full rank. The rank of hhpp mirrors that of hhhh, owing to the substantially smaller size of *hh* in comparison to *pp* within the physical context. This size differential places *hh* at the forefront of rank determination. However, it remains imperative to uphold the rank of *pp* for the sake of preserving its right singular vectors. Regarding hhhp, similarly, although its rank aligns with that of hhhp or hhpp, a nuanced adaptation becomes necessary for the

	1B-2B	ladder term	ladder(reduce-rank)	p-h term
hhhh	$\mathcal{O}(N_h^4 N_p)$	$\mathcal{O}(N_h^4 N_p^2)$	$1/8\mathcal{O}(N_h^4 N_p^2)$	None
hhhp	$\mathcal{O}(N_h^3 N_p^2)$	$\mathcal{O}(N_h^3 N_p^3)$	$1/4\mathcal{O}(N_h^3 N_p^3)$	$\mathcal{O}(N_h^4 N_p^2)$
hhpp	$\mathcal{O}(N_h^2 N_p^3)$	$\mathcal{O}(N_h^2 N_p^4)$	$1/8\mathcal{O}(N_h^2 N_p^4)$	$\mathcal{O}(N_h^3 N_p^3)$
hphp	$\mathcal{O}(N_h^2 N_p^3)$	None	None	$\mathcal{O}(N_h^3 N_p^3)$
hppp	$\mathcal{O}(N_h N_p^4)$	$\mathcal{O}(N_h^3 N_p^3)$	$1/4\mathcal{O}(N_h^3 N_p^3)$	$\mathcal{O}(N_h^2 N_p^4)$
pppp	$\mathcal{O}(N_p^5)$	$\mathcal{O}(N_h^2 N_p^4)$	$1/8\mathcal{O}(N_h^2 N_p^4)$	None

Table 10.1: Time complexity analysis of each term in the evolution of 6 essential blocks. The table presents the computational time complexities associated with individual terms within the evolution of each essential block, offering insights into the intricacies of the computational demands for various components of the studied system. The white generator is used in this case.

right singular vectors, entailing the inversion of all singular bases. Analogously, for hppp, a reversal process is applied to the rank of *hp* in relation to left singular vectors, and a reduced rank of *pp* is enacted for the right singular vectors.

Table 10.1 provides an exposition of the time complexities associated with the two-body evolution (IMSRG) of the six pivotal blocks. As previously demonstrated, the two-body evolution encompasses three distinct terms: the interplay between one-body and two-body components, a ladder term and a particle-hole (p-h) term. Notably, the most substantial time complexity arises during the evolution of hppp within the p-h term and of pppp and hhpp within the ladder term, both exhibiting a complexity of $\mathcal{O}(N_h^2 N_p^4)$, aligning consistently with prior discussions. Moreover, the ladder term consistently exhibits reducibility in its SVD form, or SVD-IMSRG in particular.

Consequently, the preeminant factor driving complexity is the particle-hole term within hppp, warranting further rigorous investigation. Expanding our focus, we endeavor to scrutinize the precise contribution of the p-h term within each distinct block. Subsequent part delve into the comprehensive efforts undertaken to dissect and elucidate these contributions.

Figure 10.2 provides a comparative analysis between the IMSRG and Block-IMSRG ap-

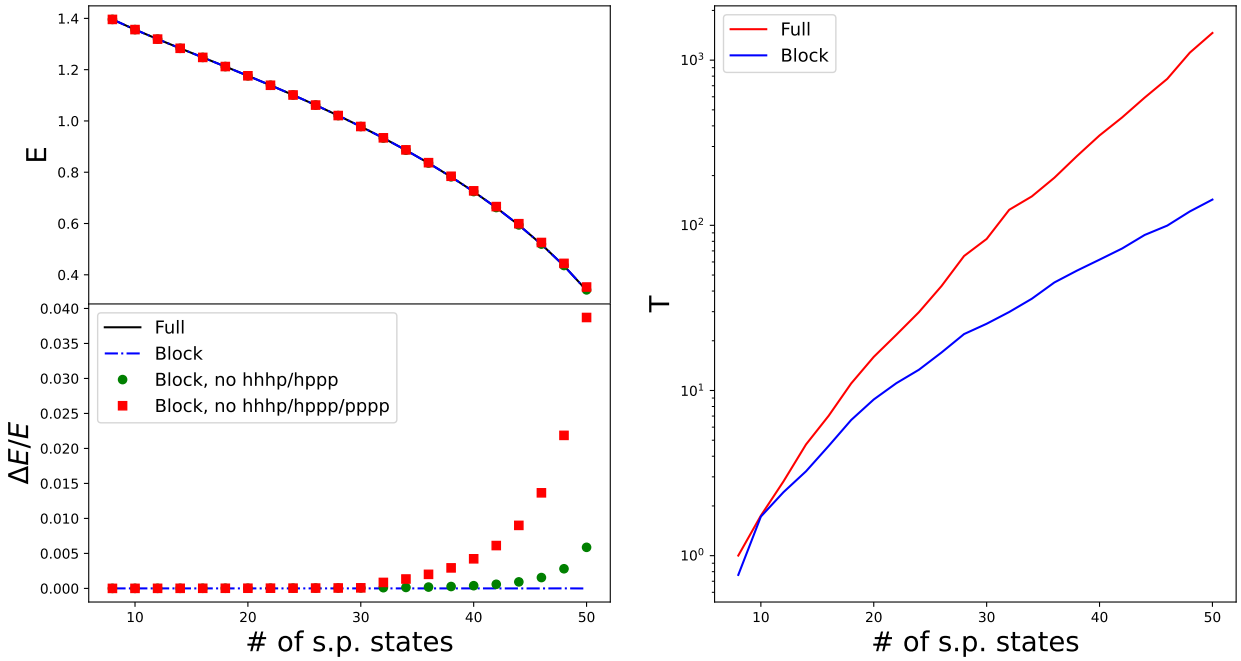

Figure 10.2: Right Panel: The computational time required for IMSRG and Block-IMSRG is depicted across a range of single-particle states. Notably, a distinct acceleration in computational efficiency is observed within the range of 10-15 single-particle states relative to hole states. Left Panel(Top): Ground-state energies obtained through IMSRG and Block-IMSRG are presented, along with an assessment of omitted contributions. In the context of hhhp and hppp blocks, the particle-hole term is omitted, while for pppp, the interplay between one-body and two-body components is disregarded. Left Panel(Bottom): The error ratio, reflecting the discrepancy between the calculated and accepted ground-state energies. As the number of single particle states increases, the impact of omitted contribution becomes progressively pronounced, underscoring the interplay between accuracy and computational efficiency.

proaches. The right panel illustrates the computational time required for IMSRG and Block-IMSRG across varying number of single-particle states, while the number of hole states remains constant at 4. Noteworthy, when the ratio of the number particle states (N_p) to that of hole states (N_h) falls within the range of 10-15, a nearly tenfold acceleration in computational efficiency is observed. Remarkably, this acceleration is achieved without truncation; rather, it arises from the streamlined manipulation of a reduced set of matrix elements.

The left panel presents a juxtaposition of ground-state energies obtained through IMSRG, Block-IMSRG, and a modified Block-IMSRG approach involving selective contribution omis-

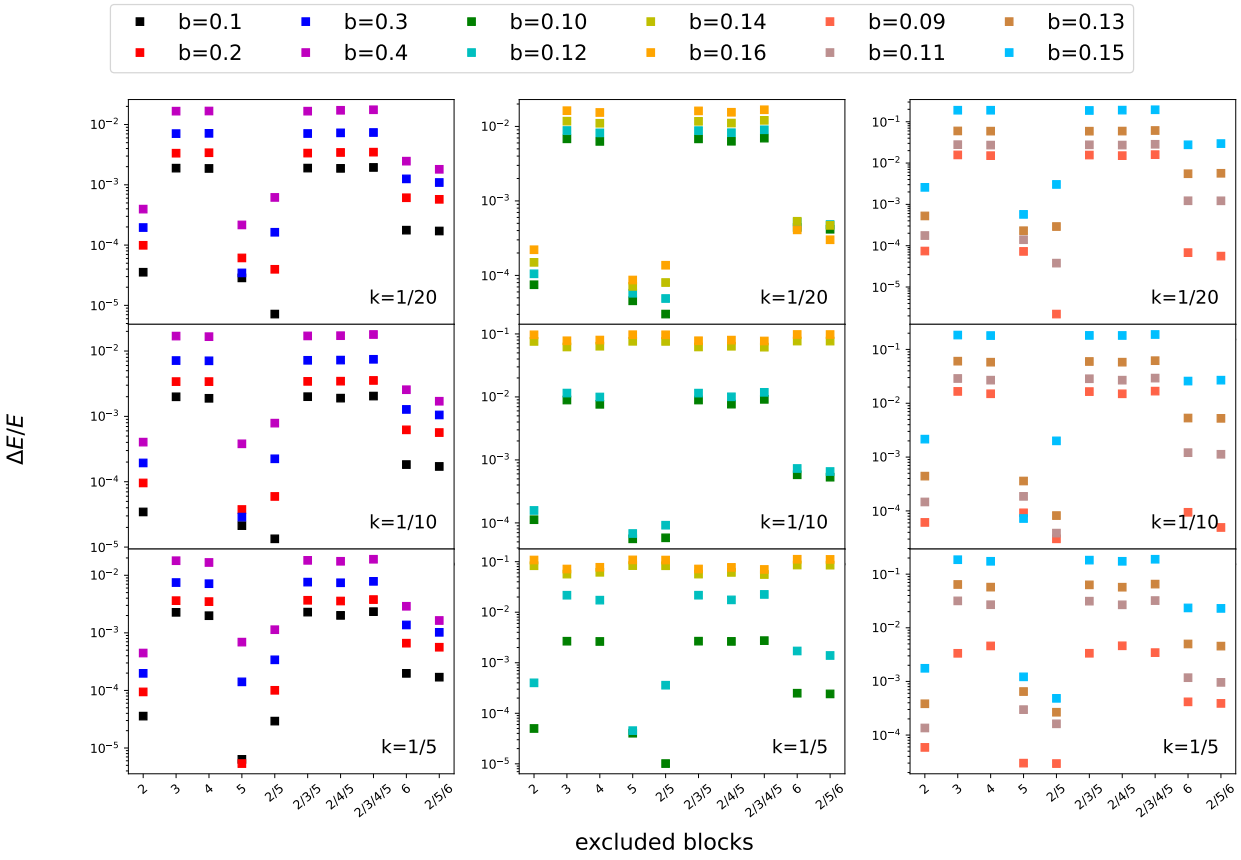

Figure 10.3: .

sion. This omission aims to significantly reduce complexity while maintaining a high level of accuracy. At the top panel the left graph, distinguishing the calculated ground state energies poses a challenge. However, the bottom panel introduces an error ratio that elucidates a arguably trend: as the number of single-particle states, or the number of particle states, increases, the influence of the omitted contributions becomes increasingly pronounced. The phenomenon warrants a more extensive exploration, which will be expounded upon in the following.

At present, our focus is dedicated to an intricate investigation into the distinctive contributions of particle-hole term within each block. In Figure 10.3, we present a comprehensive analysis of the error ratios observed in Block-IMSRG calculation, with the selective omission

of the particle-hole term in specific blocks. This exploration is conducted under varying conditions of randomness, characterized by distinct scalings (1/20, 1/10 and 1/5) as indicated in the graph.

The left, middle and right panels of the figure depict calculations performed on a pairing model with 8, 16 and 30 single-particle states, respectively, while remaining a constant hole state count of 4. Within each sub-panel, diverse pairing-breaking terms (denoted as 'b') are taken into account. Additionally, the axis is represented numerically (1, 2, 3, 4, 5, 6) corresponding to the blocks with labels (hhhh, hhhp, hhpp, hphp, hppp, pppp).

From the analysis of the graph, intriguing observations emerge. As the strength of randomness (k), or pair-breaking strength (b), intensifies, the influence of the particle-hole term becomes more pronounced, reflecting a heightened significance. Furthermore, with an escalation in the number of single-particle states, the contribution of particle-hole term experience a proportional augmentation. Particularly noteworthy is the realization that the particle-hole terms within hhhp and hppp, characterized by scalings of $\mathcal{O}(N_h^4 N_p^2)$ and $\mathcal{O}(N_h^2 N_p^4)$ respectively, can be safely truncated without compromising accuracy. Of potential significance is the consideration of omitting the 1B-2B term in pppp. Although marginally larger than those in hhhp and hppp, the contribution of this term is notably smaller compared to the others, as evidenced in Figure 10.4.

This approach warrants an extensive exploration within the domain of real nuclear systems, such as infinite nuclear matter. In scenarios where the ratio of the number of single-particle states to the number hole states exhibits a larger magnitude, roughly between 10 to 15, the sensitivity of particle-hole term contributions within each block to interaction strength becomes more pronounced. With regard to computational time complexity, the most substantial complexities manifest in hhpp and pppp blocks within the ladder term.

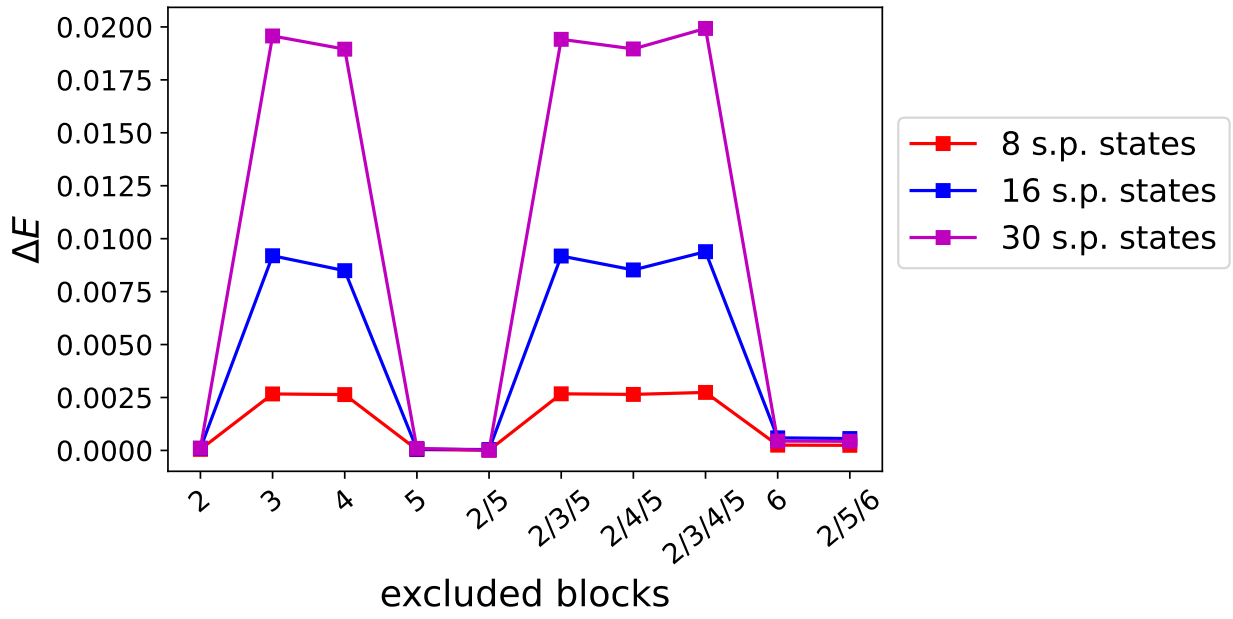

Figure 10.4: .

However, employing singular value decomposition allows for an asymptotic complexity reduction by a factor of 1/8. This reduction stems from the observation that the ranks of *hh* and *pp* are half of their respective dimensions, as per Eq. **??**. Another notable instance of high complexity arises in the particle-hole term of hppp, which can be safely truncated. The viability of omitting the 1B-2B term in pppp, scaled at $\mathcal{O}(N_p^5)$, presents a subject for consideration, even it is small enough.

Collectively, these advancements culminate in a noteworthy reduction of the original IMSRG time complexity by a factor of 1/8. While certain blocks may not exert dominant influences, their contribution remains vital in expediting calculations. A lingering task involves delving into the calculation of η through the rank-reduced representation of Γ. The present methodology necessitates the repetitive reconstruction of blocks and subsequent η derivation in each step, a process characterized by its time-intensive and intricate nature. Addressing this challenge constitutes a pivotal avenue for future investigation.

Conclusions and Outlook

Chapter 11

Conclusion and outlook

In conclusion, this dissertaion presents a comprehensive exploration of factorization techniques applied to nuclear interactions and many-body methods, with a primary objective of enhancing the computational efficiency and reducing memory demands in contemporary nuclear many-body calculations. The research journey begins with the utilization of Singular Value Decomposition (SVD) to construct precise low-rank models for nucleon-nucleon interactions, followed by the development of an innovative Similarity Renormalization Group (SRG) variant to evolve these interactions in the SVD-factorized form.

Extending this investigation to encompass three-nucleon interactions, we employ randomized SVD algorithms to address the challenges posed by significantly larger basis dimensions. While evidence of low-rank structures in three-nucleon interactions emerges, we identify impediments to sustained rank reduction, primarily attributed to SRG-induced interactions.

Furthermore, we delve into the application of SVD for factorization and rank reduction within the framework of the In-Medium SRG (IMSRG). This leads to the development of rank-reduced IMSRG flow equations, offering promising results despite persisting computational hurdles linked to the treatment of particle-hole terms. As an initial step towards resolving this issue, we conduct a comprehensive breakdown of the scaling and significance of all contributions within the ISMRG flow, exemplified through applications in a schematic model and infinite neutron matter, utilizing realistic interactions from chiral Effective Field

Theory.

As we set our sights on future research endeavors, the utilization of these advanced algorithms and methodological enhancements holds the potential to extend their applicability to the realm of infinite matter within the SVD-IMSRG framework, specifically focusing on the primary block. This extension would enable us to conduct a thorough comparative analysis with conventional IMSRG outcomes. This comparative assessment serves the crucial purpose of evaluating the pertinence of truncating the second block, as previously established in the context of the pairing model.

Furthermore, our research trajectory offers a unique opportunity to delve into novel decomposition and contraction techniques. These innovative methods have the potential to streamline and expedite the computation of particle-hole contributions within the IMSRG formalism. Such investigations hold promise for enhancing the overall efficiency and efficacy of the IMSRG approach.

In summary, this dissertation advances the understanding and utilization of factorization techniques to enhance the efficiency of nuclear many-body calculations, offering valuable insights into low-rank structures in nuclear interactions and paving the way of more computationally tractable methods in the field of nuclear physics. The research herein lays a solid foundation for further investigations into the optimization of computational resources in nuclear physics simulations, with potential implications for broader applications in the study of nuclear systems.

Bibliography

[1] E Anderson et al. "Block diagonalization using similarity renormalization group flow equations". In: *Physical Review C* 77.3 (2008), p. 037001.

[2] ER Anderson et al. "Operator evolution via the similarity renormalization group: The deuteron". In: *Physical Review C* 82.5 (2010), p. 054001.

[3] W. E. Arnoldi. "The principle of minimized iterations in the solution of the matrix eigenvalue problem". In: *Quarterly of Applied Mathematics* 9.1 (1951), pp. 17–29.

[4] C. Barbieri and A. Carbone. "Self-Consistent Green's Function Approaches". In: *An Advanced Course in Computational Nuclear Physics*. Ed. by M. Hjorth-Jensen, M. Lombardo, and U. van Kolck. Lecture Notes in Physics 936. Springer, 2017. Chap. 11.

[5] Bruce R. Barrett, Petr Navrátil, and James P. Vary. "Ab initio no core shell model". In: *Prog. Part. Nucl. Phys.* 69.0 (2013), pp. 131 –181.

[6] Sven Binder et al. "Ab initio path to heavy nuclei". In: *Physics Letters B* 736 (2014), pp. 119–123.

[7] Sven Binder et al. "Extension of coupled-cluster theory with a noniterative treatment of connected triply excited clusters to three-body Hamiltonians". In: *Physical Review C* 88.5 (2013), p. 054319.

[8] Sergio Blanes et al. "The Magnus expansion and some of its applications". In: *Physics reports* 470.5-6 (2009), pp. 151–238.

[9] SK Bogner, Richard J Furnstahl, and RJ Perry. "Similarity renormalization group for nucleon-nucleon interactions". In: *Physical Review C* 75.6 (2007), p. 061001.

[10] SK Bogner, RJ Furnstahl, and Achim Schwenk. "From low-momentum interactions to nuclear structure". In: *Progress in Particle and Nuclear Physics* 65.1 (2010), pp. 94–147.

[11] SK Bogner, Thomas Tzu Szu Kuo, and A Schwenk. "Model-independent low momentum nucleon interaction from phase shift equivalence". In: *Physics Reports* 386.1 (2003), pp. 1–27.

[12] SK Bogner et al. "Convergence of the Born series with low-momentum interactions". In: *Nuclear Physics A* 773.3-4 (2006), pp. 203–220.

[13] SK Bogner et al. "Nonperturbative shell-model interactions from the in-medium similarity renormalization group". In: *Physical Review Letters* 113.14 (2014), p. 142501.

[14] Peter N Brown and Alan C Hindmarsh. "Reduced storage matrix methods in stiff ODE systems". In: *Applied Mathematics and Computation* 31 (1989), pp. 40–91.

[15] Gerhard Buchalla, Oscar Catà, and Claudius Krause. "On the power counting in effective field theories". In: *Physics Letters B* 731 (2014), pp. 80–86.

[16] Angelo Calci. "Evolved chiral Hamiltonians at the three-body level and beyond". In: (2014).

[17] James Chadwick. "The existence of a neutron". In: *Proceedings of the Royal Society of London. Series A, Containing Papers of a Mathematical and Physical Character* 136.830 (1932), pp. 692–708.

[18] Moody T Chu. "Scaled Toda-like flows". In: *Linear algebra and its applications* 215 (1995), pp. 261–273.

[19] S. A. Coon et al. "Convergence properties of ab initio calculations of light nuclei in a harmonic oscillator basis". In: *Phys. Rev. C* 86 (5 Nov. 2012), p. 054002.

[20] Carl Eckart and Gale Young. "The approximation of one matrix by another of lower rank". In: *Psychometrika* 1.3 (1936), pp. 211–218.

[21] A Ekström et al. "What is ab initio in nuclear theory?" In: *Frontiers in Physics* 11 (2023), p. 125.

[22] DR Entem and R Machleidt. "Accurate charge-dependent nucleon-nucleon potential at fourth order of chiral perturbation theory". In: *Physical Review C* 68.4 (2003), p. 041001.

[23] Evgeny Epelbaum, Hermann Krebs, and Patrick Reinert. "High-precision nuclear forces from chiral EFT: state-of-the-art, challenges, and outlook". In: *Frontiers in Physics* 8 (2020), p. 98.

[24] EB Fel'dman. "On the convergence of the Magnus expansion for spin systems in periodic magnetic fields". In: *Physics Letters A* 104.9 (1984), pp. 479–481.

[25] Alexander L. Fetter and John D. Walecka. *Quantum Theory of Many-Particle Systems*. Dover Publications, June 2003. ISBN: 0486428273.

[26] Paolo Finelli, Matteo Vorabbi, and Carlotta Giusti. "Microscopic Optical Potentials: recent achievements and future perspectives". In: *Journal of Physics: Conference Series*. Vol. 2453. 1. IOP Publishing. 2023, p. 012026.

[27] RJ Furnstahl. "The renormalization group in nuclear physics". In: *Nuclear Physics B-Proceedings Supplements* 228 (2012), pp. 139–175.

[28] RJ Furnstahl et al. "Infrared extrapolations for atomic nuclei". In: *Journal of Physics G: Nuclear and Particle Physics* 42.3 (2015), p. 034032.

[29] Eskendr Gebrerufael, Angelo Calci, and Robert Roth. "Open-shell nuclei and excited states from multireference normal-ordered Hamiltonians". In: *Physical Review C* 93.3 (2016), p. 031301.

[30] G. Hagen et al. "Coupled-cluster computations of atomic nuclei". In: *Rept. Prog. Phys.* 77.9 (2014), p. 096302.

[31] G Hagen et al. "M. W loch, and P. Piecuch". In: *Phys. Rev. C* 76.3 (2007).

[32] Nathan Halko, Per-Gunnar Martinsson, and Joel A Tropp. "Finding structure with randomness: Stochastic algorithms for constructing approximate matrix decompositions". In: (2009).

[33] K. Hebeler et al. "Improved nuclear matter calculations from chiral low-momentum interactions". In: *Phys. Rev. C* 83 (3 Mar. 2011), p. 031301.

[34] Kai Hebeler. "Momentum-space evolution of chiral three-nucleon forces". In: *Physical Review C* 85.2 (2012), p. 021002.

[35] Kai Hebeler. "Three-nucleon forces: Implementation and applications to atomic nuclei and dense matter". In: *Physics Reports* 890 (2021), pp. 1–116.

[36] Werner Heisenberg. "On the structure of atomic nuclei". In: *Z. Phys* 77.1 (1932).

[37] H Hergert. "In-medium similarity renormalization group for closed and open-shell nuclei". In: *Physica Scripta* 92.2 (2016), p. 023002.

[38] H Hergert and R Roth. "Treatment of the intrinsic Hamiltonian in particle-number nonconserving theories". In: *Physics Letters B* 682.1 (2009), pp. 27–32.

[39] H Hergert et al. "The in-medium similarity renormalization group: A novel ab initio method for nuclei". In: *Physics reports* 621 (2016), pp. 165–222.

[40] Heiko Hergert. "A guided tour of ab initio nuclear many-body theory". In: *Frontiers in Physics* 8 (2020), p. 379.

[41] Heiko Hergert et al. "In-medium similarity renormalization group approach to the nuclear many-body problem". In: *An Advanced Course in Computational Nuclear Physics*. Springer, 2017, pp. 477–570.

[42] Alan C Hindmarsh. "ODEPACK, a systemized collection of ODE solvers". In: *Scientific computing* (1983).

[43] Alan C Hindmarsh et al. "SUNDIALS: Suite of nonlinear and differential/algebraic equation solvers". In: *ACM Transactions on Mathematical Software (TOMS)* 31.3 (2005), pp. 363–396.

[44] Osamu Hino, Tomoko Kinoshita, and Rodney J. Bartlett. "Singular value decomposition applied to the compression of T3 amplitude for the coupled cluster method". In: *J. Chem. Phys.* 121.3 (Jan. 2004), pp. 1206–1213.

[45] Edward G. Hohenstein et al. "Rank-reduced coupled-cluster. III. Tensor hypercontraction of the doubles amplitudes". In: *J. Chem. Phys.* 156.5 (Feb. 2022), p. 054102.

[46] Edward G. Hohenstein et al. "Rank reduced coupled cluster theory. II. Equation-of-motion coupled-cluster singles and doubles". In: *J. Chem. Phys.* 151.16 (Apr. 2019), p. 164121.

[47] Jason D Holt et al. "Counter terms for low momentum nucleon–nucleon interactions". In: *Nuclear Physics A* 733.1-2 (2004), pp. 153–165.

[48] Calvin W Johnson. "Unmixing symmetries". In: *Physical Review Letters* 124.17 (2020), p. 172502.

[49] ED Jurgenson, Petr Navratil, and RJ Furnstahl. "Evolving nuclear many-body forces with the similarity renormalization group". In: *Physical Review C* 83.3 (2011), p. 034301.

[50] Eric Donald Jurgenson. "Applications of the similarity renormalization group to the nuclear interaction". In: *arXiv preprint arXiv:0912.2937* (2009).

[51] G.P. Kamuntavičius et al. "The general harmonic-oscillator brackets: compact expression, symmetries, sums and Fortran code". In: *Nuclear Physics A* 695.1 (2001), pp. 191–201.

[52] Stefan Kehrein. *The flow equation approach to many-particle systems*. Vol. 217. Springer, 2007.

[53] Tomoko Kinoshita, Osamu Hino, and Rodney J. Bartlett. "Singular value decomposition approach for the approximate coupled-cluster method". In: *J. Chem. Phys.* 119.15 (Oct. 2003), pp. 7756–7762.

[54] S. König et al. "Ultraviolet extrapolations in finite oscillator bases". In: *Phys. Rev. C* 90 (6 Dec. 2014), p. 064007.

[55] Werner Kutzelnigg. "Quantum chemistry in Fock space. I. The universal wave and energy operators". In: *The Journal of Chemical Physics* 77.6 (1982), pp. 3081–3097.

[56] Werner Kutzelnigg. "Quantum chemistry in Fock space. III. Particle-hole formalism". In: *The Journal of chemical physics* 80.2 (1984), pp. 822–830.

[57] Werner Kutzelnigg and Sigurd Koch. "Quantum chemistry in Fock space. II. Effective Hamiltonians in Fock space". In: *The Journal of chemical physics* 79.9 (1983), pp. 4315–4335.

[58] C. Lanczos. "An iteration method for the solution of the eigenvalue problem of linear differential and integral operators". In: *J. Res. Nat'l Bur. Std.* 45 (1950), p. 255.

[59] G Peter Lepage. "What is renormalization?" In: *arXiv preprint hep-ph/0506330* (2005).

[60] GP Lepage. "How to renormalize the Schrodinger equation". In: *Nuclear Physics (ed. by CA Bertulani et al.)* (1997), p. 135.

[61] Michał Lesiuk. "Near-Exact CCSDT Energetics from Rank-Reduced Formalism Supplemented by Non-iterative Corrections". In: *J. Chem. Theory Comput.* 17.12 (Dec. 2021), pp. 7632–7647.

[62] Michał Lesiuk. "Quintic-scaling rank-reduced coupled cluster theory with single and double excitations". In: *J. Chem. Phys.* 156.6 (Oct. 2022), p. 064103.

[63] Justin G Lietz et al. "Computational nuclear physics and post hartree-fock methods". In: *An Advanced Course in Computational Nuclear Physics: Bridging the Scales from Quarks to Neutron Stars* (2017), pp. 293–399.

[64] R Machleidt. "High-precision, charge-dependent Bonn nucleon-nucleon potential". In: *Physical Review C* 63.2 (2001), p. 024001.

[65] R Machleidt. "The theory of nuclear forces: Is the never-ending story coming to an end?" In: *arXiv preprint nucl-th/0701077* (2007).

[66] Re Machleidt. "The meson theory of nuclear forces and nuclear structure". In: *Advances in nuclear physics*. Springer, 1989, pp. 189–376.

[67] Ruprecht Machleidt and David Rodrignez Entem. “Chiral effective field theory and nuclear forces”. In: *Physics Reports* 503.1 (2011), pp. 1–75.

[68] Wilhelm Magnus. “On the exponential solution of differential equations for a linear operator”. In: *Communications on pure and applied mathematics* 7.4 (1954), pp. 649–673.

[69] S. N. More et al. “Universal properties of infrared oscillator basis extrapolations”. In: *Phys. Rev. C* 87 (4 Apr. 2013), p. 044326.

[70] TD Morris, NM Parzuchowski, and SK Bogner. “Magnus expansion and in-medium similarity renormalization group”. In: *Physical Review C* 92.3 (2015), p. 034331.

[71] P Navrátil, Gintautas Prancišskus Kamuntavičius, and Bruce R Barrett. “Few-nucleon systems in a translationally invariant harmonic oscillator basis”. In: *Physical Review C* 61.4 (2000), p. 044001.

[72] Petr Navratil. “Local three-nucleon interaction from chiral effective field theory”. In: *Few-Body Systems* 41.3-4 (2007), pp. 117–140.

[73] Petr Navrátil et al. “Unified ab initio approaches to nuclear structure and reactions”. In: *Phys. Scripta* 91.5 (2016), p. 053002.

[74] A Nogga et al. “Spectra and binding energy predictions of chiral interactions for Li 7”. In: *Physical Review C* 73.6 (2006), p. 064002.

[75] Andreas Nogga, Scott K. Bogner, and Achim Schwenk. “Low-momentum interaction in few-nucleon systems”. In: *Phys. Rev. C* 70 (6 Dec. 2004), p. 061002.

[76] D. Odell, T. Papenbrock, and L. Platter. “Infrared extrapolations of quadrupole moments and transitions”. In: *Phys. Rev. C* 93 (4 Apr. 2016), p. 044331.

[77] Robert M. Parrish et al. “Rank reduced coupled cluster theory. I. Ground state energies and wavefunctions”. In: *J. Chem. Phys.* 150.16 (Apr. 2019), p. 164118.

[78] N. M. Parzuchowski et al. “Ab initio electromagnetic observables with the in-medium similarity renormalization group”. In: *Phys. Rev. C* 96 (3 Sept. 2017), p. 034324.

[79] Maria Piarulli and Ingo Tews. “Local nucleon-nucleon and three-nucleon interactions within chiral effective field theory”. In: *Frontiers in Physics* 7 (2020), p. 245.

[80] William H Press et al. *Numerical recipes 3rd edition: The art of scientific computing*. Cambridge university press, 2007.

[81] P. Ring and P. Schuck. *The nuclear many-body problem*. New York: Springer-Verlag, 1980.

[82] David Rodriguez Entem, Ruprecht Machleidt, and Yevgen Nosyk. "Nucleon-nucleon scattering up to N5LO in chiral effective field theory". In: *Frontiers in Physics* 8 (2020), p. 57.

[83] Robert Roth and Petr Navrátil. "Ab Initio Study of Ca 40 with an Importance-Truncated No-Core Shell Model". In: *Physical review letters* 99.9 (2007), p. 092501.

[84] Robert Roth et al. "Evolved chiral N N+ 3 N Hamiltonians for ab initio nuclear structure calculations". In: *Physical Review C* 90.2 (2014), p. 024325.

[85] Robert Roth et al. "Medium-mass nuclei with normal-ordered chiral N N+ 3 N interactions". In: *Physical Review Letters* 109.5 (2012), p. 052501.

[86] Robert Roth et al. "Similarity-Transformed Chiral N N+ 3 N Interactions for the Ab Initio Description of C 12 and O 16". In: *Physical Review Letters* 107.7 (2011), p. 072501.

[87] Micah D Schuster et al. "Operator evolution for ab initio theory of light nuclei". In: *Physical Review C* 90.1 (2014), p. 011301.

[88] Isaiah Shavitt and Rodney J Bartlett. *Many-body methods in chemistry and physics: MBPT and coupled-cluster theory*. Cambridge university press, 2009.

[89] Vittorio Somà. "Self-Consistent Green's Function Theory for Atomic Nuclei". In: *Frontiers in Physics* 8 (2020), p. 340.

[90] H. P. Stapp, T. J. Ypsilantis, and N. Metropolis. "Phase-Shift Analysis of 310-Mev Proton-Proton Scattering Experiments". In: *Phys. Rev.* 105 (1 Jan. 1957), pp. 302–310.

[91] SR Stroberg et al. "Ab initio limits of atomic nuclei". In: *Physical Review Letters* 126.2 (2021), p. 022501.

[92] SR Stroberg et al. "Ground and excited states of doubly open-shell nuclei from ab initio valence-space Hamiltonians". In: *Physical Review C* 93.5 (2016), p. 051301.

[93] SR Stroberg et al. "Nucleus-dependent valence-space approach to nuclear structure". In: *Physical Review Letters* 118.3 (2017), p. 032502.

[94] Alexander Tichai et al. "Tensor-decomposition techniques for ab initio nuclear structure calculations: From chiral nuclear potentials to ground-state energies". In: *Physical Review C* 99.3 (2019), p. 034320.

[95] AJ Tropiano, SK Bogner, and RJ Furnstahl. "Operator evolution from the similarity renormalization group and the Magnus expansion". In: *Physical Review C* 102.3 (2020), p. 034005.

[96] CM Vincent and SC Phatak. "Accurate momentum-space method for scattering by nuclear and Coulomb potentials". In: *Physical Review C* 10.1 (1974), p. 391.

[97] Sergey Voronin and Per-Gunnar Martinsson. "RSVDPACK: An implementation of randomized algorithms for computing the singular value, interpolative, and CUR decompositions of matrices on multi-core and GPU architectures". In: *arXiv preprint arXiv:1502.05366* (2015).

[98] Meng Wang et al. "The AME 2020 atomic mass evaluation (II). Tables, graphs and references". In: *Chinese Physics C* 45.3 (2021), p. 030003.

[99] F. Wegner. "Flow equations for Hamiltonians". In: *Ann. Phys. (Leipzig)* 3 (1994), p. 77.

[100] Franz J Wegner. "Flow equations for Hamiltonians". In: *Physics Reports* 348.1-2 (2001), pp. 77–89.

[101] Steven Weinberg. "Effective chiral Lagrangians for nucleon-pion interactions and nuclear forces". In: *Nuclear Physics B* 363.1 (1991), pp. 3–18.

[102] Steven Weinberg. "Phenomenological lagrangians". In: *Physica a* 96.1-2 (1979), pp. 327–340.

[103] Steven Weinberg. "What is quantum field theory, and what did we think it is?" In: *arXiv preprint hep-th/9702027* (1997).

[104] K. A. Wendt. "Similarity renormalization group evolution of three-nucleon forces in a hyperspherical momentum representation". In: *Phys. Rev. C* 87 (6 June 2013), p. 061001.

[105] K. A. Wendt et al. "Infrared length scale and extrapolations for the no-core shell model". In: *Phys. Rev. C* 91 (6 June 2015), p. 061301.

[106] Steven R. White. "Numerical canonical transformation approach to quantum many-body problems". In: *J. Chem. Phys.* 117.16 (2002), pp. 7472–7482.

[107] G. C. Wick. "The Evaluation of the Collision Matrix". In: *Phys. Rev.* 80 (2 Oct. 1950), pp. 268–272.

[108] Kenneth G Wilson. "Problems in physics with many scales of length". In: *Scientific American* 241.2 (1979), pp. 158–179.

[109] Robert B Wiringa, VGJ Stoks, and R Schiavilla. "Accurate nucleon-nucleon potential with charge-independence breaking". In: *Physical Review C* 51.1 (1995), p. 38.

[110] J. M. Yao et al. "Ab Initio Treatment of Collective Correlations and the Neutrinoless Double Beta Decay of ^{48}Ca". In: *Phys. Rev. Lett.* 124 (23 June 2020), p. 232501.

[111] Hideki Yukawa and Shoichi Sakata. "On the Theory of the β-Disintegration and the Allied Phenomenon". In: *Proceedings of the Physico-Mathematical Society of Japan. 3rd Series* 17 (1935), pp. 467–479.

[112] B Zhu, R Wirth, and H Hergert. "Singular value decomposition and similarity renormalization group evolution of nuclear interactions". In: *Physical Review C* 104.4 (2021), p. 044002.